MODELING METHODOLOGY OF CONVERTERS FOR HVDC SYSTEMS AND LFAC SYSTEMS: INTEGRATION AND TRANSMISSION OF RENEWABLE ENERGY

A Dissertation
Presented to
The Academic Faculty

by

Yongnam Cho

In Partial Fulfillment
of the Requirements for the Degree
Doctor of Philosophy in the
School of Electrical and Computer Engineering

Georgia Institute of Technology
August 2013

Copyright © 2013 by Yongnam Cho

MODELING METHODOLOGY OF CONVERTERS FOR HVDC SYSTEMS AND LFAC SYSTEMS: INTEGRATION AND TRANSMISSION OF RENEWABLE ENERGY

Approved by:

Dr. A. P. Sakis Meliopoulos, Advisor
School of Electrical and Computer Engineering
Georgia Institute of Technology

Dr. Anthony Joseph Yezzi
School of Electrical and Computer Engineering
Georgia Institute of Technology

Dr. Ronald G. Harley, Committee Chair
School of Electrical and Computer Engineering
Georgia Institute of Technology

Dr. David G. Taylor
School of Electrical and Computer Engineering
Georgia Institute of Technology

Dr. Shijie Deng
School of Industrial and Systems Engineering
Georgia Institute of Technology

Date Approved: [May 24, 2013]

To my father, Hongkyu Cho:

Even though you are not with us, I am sure that you are eagerly looking forward to my graduation. Father, the work is now complete in your dedication.

To my beloved mother, Waoulhee Yoon, to my sisters, Eunhee Cho and Eunjin Cho

ACKNOWLEDGEMENTS

Your word is a lamp to guide my feet and a light for my path.

PSALM: 119: 105

When I look back on my Ph. D. period at Georgia Institute of Technology, the journey is filled with a life full of hardship and struggle. However, the quote above leads me to reach the end of the doctoral degree. First of all, I would like to thank my God for seeing me through these seven years. I would also like to thank the people who have supported and encouraged me during this period.

I remember the first encounter I had with my Ph. D. advisor, Professor A. P. Sakis Meliopoulos. He was (and still is) a very kind and approachable person. Even though I couldn't speak English well, he always carefully listened to my word and helped me to improve my verbal English. During my Ph.D., He has fully supported and encouraged me academically and personally. Specifically, I remember that he consoled and supported me when my father passed away, this is something I could never forget. Also, I have come to see what a great educator and advisor Professor Meliopoulos is. If I am ever opportune to advice students, I would really want to emulate my advisor. I am truly grateful to him for his immense support both academically and personally.

Furthermore, I would like to thank Professor Ronald G. Harley, Professor Shijie Deng, Professor Anthony Joseph Yezzi, and Professor David G. Taylor, who as my Ph. D. committee members, have helped me get to where I am today. These committee members of my Ph.D. dissertation were the key to the success of this work. Their comments and guidance were instrumental in making a lot of improvement to my initial work. They

provided the directions for my dissertation and the knowledge in the classes they taught me.

I would like to express my appreciation to Dr. George J. Cokkinides for his noble support and help in my research. He was always ready to help amidst his busy schedule. I consider him a specialist in power system engineering, and have learned a lot under his supervision.

In addition, I would like to show my appreciation to my friends and colleagues which were and are in the Power Systems Control and Automation Laboratory including the ones that have graduated already. First, when I joined the laboratory, Dr. Georgios K. Stefopoulos, Dr. Salman Mohagheghi, and Dr. Q. Binh Dam welcomed me and delightfully shared their knowledge and wisdom with me. Also, I had the pleasure to exchange opinions with Dr. Vangelis Farantatos, Kyle Howells, Dr. Curtis Roe, Renke Huang**,** Dr. Ye Tao, Sandhya Madan**,** Stephanie M. Gossman, Anupama Keeli, and Xuebei Yu.

Moreover, I would like to express my appreciation for the support my Korean friends in power group gave me. Yonghee Lee, Jongkook Park, Namhum Cho, Dr. Sangtek Han and Insu Kim were very supportive during my difficulties. I would like to specifically thank Sungyun Choi who was a companion that studied together with me during the whole period of my journey at Georgia Institute of Technology. Also, I would also like to thank visiting scholars that came to our lab later, Dr. Beung-Jin Kim, Dr. Sungsam Kim, Dr. SooHyoung Lee, and Dr. Sungyul Kim.

Finally, I am grateful to the new members in the Power Systems Control and Automation Laboratory for their help. They include: Dongbo Zhao, Evangelos Polymeneas, Rui Fan, Zhenyu Tan, Liangyi Sun, and Thamer Alquthami. Specially, I would like to thank Aniemi Umana who has helped me to practice and improve my conversational English.

TABLE OF CONTENTS

Page

LIST OF TABLES

Page

LIST OF FIGURES

Page

SUMMARY

The major achievements of this work are based on two categories: (A) introduction of an advanced simulation technique in both time domain and frequency domain, and (B) realistic and reliable models for converters applicable to analysis of alternative transmission systems.

The proposed modeling-methodology using a combination of model quadratization and quadratic integration has been demonstrated as a more robust, stable, and accurate method for power system analysis than previous numerical-methods. In particular, the quadratic-integration method is free of artificial numerical-oscillations exhibited by trapezoidal integration (which is the most widely used method for power-transient analysis) during simulations of power systems with nonlinearities and switching subsystems. Artificial numerical oscillations can be the direct reason for switching malfunction and switching failure, even though the system to be analyzed is in a stable condition. However, by the application of the quadratic-integration method, fictitious oscillations can be easily eliminated without any additional control algorithm (such as numerical stabilizers, damping adjustment methods, and wave digital filters); and accurate simulations can be assured of power systems.

Also, model quadratization allows nonlinear equations to be solved without any approximation methods, such as the linearization of nonlinear equations. In this method, high-order, nonlinear equations are transformed into linear and quadratic equations, in which the highest order is not bigger than two. After model quadratization, Newton's method is applied to iteratively solve the quadratized models. It is worth noting that the quadratized models are inherently best matched to Newton's method. Therefore, the

combination of model quadratization and quadratic integration is suitable for simulations of network systems with nonlinear components and switching subsystems.

Realistic and reliable models by the combination method of model quadratization and quadratic-integration method can be used for advanced designs and optimization studies for alternative transmission systems; they can also be used to perform a comprehensive evaluation of the technical performance and economics of alternative transmission systems. For example, the converters can be used for comprehensive methodology for determining the optimal topology, kV-levels, etc. of alternative transmission systems for wind farms, for given distances of wind farms from major power grid substations. In this case, a comprehensive evaluation may help make more-informed decisions for the type of transmission (HVAC, HVDC, and LFAC) for wind farms.

CHAPTER 1

INTRODUCTION AND OBJECTIVE OF THE RESEARCH

1.1 Problem Statement

The increasing interest and gradual necessity of using renewable resources, such as wind, hydro and solar energy, have brought about strong demands for economic and technical innovation and development. In particular, both the interconnection and transmission of renewable resources into synchronous grid systems have become promising topics to power engineers. Generally, switching systems, such as HVDC-transmission systems and boost-type converters, have been used for the robust and reliable transmission and interconnection of renewable energy into central grid systems, since switching systems can easily permit excellent controllability of electrical signals: changing voltage and frequency levels, and power factors. Converter systems recently seem to be key factors in the integration of renewable resources.

Furthermore, since the demands for using long-distant sources and linking different-frequency systems have been increasing, transmission systems using HVDC-transmission systems and LFAC-transmission systems are becoming two of the promising technologies to meet the need for reliable and cost-effective transmission of electrical power from renewable resources. In particular, the rapid increase of wind power in remote and offshore locations has accelerated the necessity of more advanced, reliable and cost-effective applications of alternative transmission systems. A simulation technique in high fidelity can be one of many useful tools for advanced design and

optimization of alternative transmission systems with switching subsystems (containing AC-to-DC / DC-to-AC converters, cycloconverters, boost-type converters, etc.).

Numerical integration methods have been extensively studied and applied to transient analyses of power systems. The most predominant method among transient simulation methods is the trapezoidal-integration method, since this method has demonstrated the following properties: simplicity in application, adequate precision, and absolute stability [1], [2]. However, trapezoidal integration is problematic when applied to network systems with nonlinearities and switching subsystems (such as HVDC-transmission systems and LFAC-transmission systems). Fictitious oscillations can be generated, when the state of the network model suddenly changes. In addition, fictitious oscillations can be shown at certain combinations of integration time-steps and natural frequencies of systems to be analyzed. These fictitious oscillations are an artifact of the trapezoidal-integration method. Therefore, the system model with switching subsystems and nonlinearities cannot be properly analyzed by the pure application of trapezoidal integration. Additional algorithmic controls are needed with trapezoidal integration when it is used in systems with power electronics (switching systems) and nonlinearities.

To suppress the numerical oscillations derived from trapezoidal integration, several additional-algorithms have been proposed, such as the numerical stabilizer method [3], (b) critical damping adjustment (CDA) [4], [5], and (c) the wave digital filter (WDF) [1], [6]. Numerical stabilizers slightly change both the structure and the state equations of the network model, and cannot flawlessly eliminate fictitious oscillations in some cases. The CDA method requires variable time-steps. These variable time-steps require the companion matrices of all the devices to be recomputed for critical conditions.

The sampling rate during critical conditions is twice that during standard conditions. The WDF method can generate some abnormal distortions, and these distortions may be problematic in some cases, thus leading to less accurate results.

Therefore, trapezoidal integration is not a proper method for mixed power systems with nonlinearities and switching systems, even though this method has been successfully used for each component, which should be a nonlinear component and a switching system, with additional algorithms. Mixed-power systems have barely been modeled by the application of trapezoidal integration, and more reliable and stable methods are required for power systems to integrate renewable resources.

1.2 Objectives of the Research

The objectives of this research are (a) to introduce a high-fidelity simulation-method for alternative transmission systems (HVDC and LFAC) using converters; (b) to develop a realistic and accurate model of converters (such as phase-controlled converters and PWM converters); and (c) to study the capability of alternate transmission topologies using the proposed modeling method and developed converters. Consequently, the combination method of model quadratization and quadratic integration will be applied to several converter models in this work.

The proposed method is motivated with two concepts: (a) nonlinear model equations are converted into a set of linear and quadratic equations with the introduction of new additional variables (model quadratization) and (b) the resulting equations are integrated, assuming a quadratic variation within the integration time-step (quadratic integration). The quadratic-integration method has demonstrated advanced properties to

eliminate the artificial numerical oscillations exhibited by the application of trapezoidal integration and to enhance simulation accuracy. Since the quadratic-integration method has a natural characteristic to eliminate fictitious oscillation, additional algorithmic controls to suppress numerical oscillation are not needed. The quadratic-integration method is highly robust and stable.

Quadratic integration accompanies model quadratization to model power systems with nonlinearities and switching systems. Generally, the mixed-power systems of nonlinearities and switching systems have barely been modeled, since numerical oscillations, which are frequently generated when they are modeled, give difficulty to control switching systems and require a complex modeling process to suppress the numerical oscillations. However, the proposed modeling methodology, a combination method of model quadratization and quadratic integration (QMQI), can be applied to the mixed-power systems with nonlinearities and switching systems without additional algorithms, since the method has a natural characteristic to eliminate artificial oscillations. Modal quadratization is introduced for high-order nonlinearities such as saturable reactors and saturable transformers. Using modal quadratization, high-order nonlinear equations can be converted into a set of linear and quadratic equations. Consequently, quadratized models are denoted as linear, quadratic, and differential equations. Then, quadratic integration is applied to the quadratized models to transform the differential equations into algebraic equations.

The QMQI method permits modeling and analyzing power systems with nonlinearities and switching systems, with great accuracy and simplicity. In this research, the superior properties of the QMQI method to analyze power systems with nonlinearities

and switching systems are presented in comparison to two other methods (the trapezoidal integration method, which is one of the most popularly used methods for power system analysis and the cubic integration method that is an extension of trapezoidal integration and the quadratic-integration method). After demonstrating the superior properties of the QMQI method, this method is applied to converters, such as phase-controlled converters, PWM converters, and push-pull, resonant converters, for reliable and realistic models in both the frequency domain and time domain.

Using reliable and realistic models, alternative transmission systems, such as HVDC-transmission systems and LFAC-transmission systems, are analyzed and studied for cost-effective and technically suitable interconnections between synchronous grid systems and renewable resources. Specifically, in this work, LFAC-transmission systems connecting wind-farm systems are analyzed by performing operational studies, transient-stability studies, power-transient studies, and harmonic studies. In this case, comprehensive evaluations may help make more informed decisions for the type of transmission (HVAC, HVDC, and LFAC) involving for the wind farms.

1.3 Thesis Outline

A brief outline of the remainder of this dissertation is presented in this section:

In Chapter 2, the origin and history of the research topic is described. First, general descriptions of alternative-power-transmission systems, for example, HVDC-transmission systems and LFAC-transmission systems, are presented. Then, a transient-simulation method for alternative transmission systems with switching subsystems is presented. In addition, the results of a literature survey are presented.

A new type of modeling methodology using a combination of model quadratization and quadratic integration, which is denoted as the QMQI method in brevity, is presented in Chapter 3. In this chapter, quadratic integration is compared to other methods to demonstrate the superior properties of the QMQI method in analyses of power systems with nonlinearities and switching subsystems. Also, the QMQI method is applied to a push-pull, resonant converter to show how to model converters by the application of the QMQI method.

Chapter 4 provides converter models in a (quasi-) steady state using an averaging modeling concept. In this chapter, averaging methods of a three-phase, six-pulse converter, a three-phase, six-pulse cycloconverter, and a three-phase, PWM converter are presented. The averaged converter models in a steady-state are suitable for the quantitative analysis of power systems, and the averaged converter models in a quasi-steady state are used to analyze the dynamic behavior of power systems at a specific frequency.

Chapter 5 provides a brief explanation of time-domain models of a three-phase, six-pulse converter, a three-phase, six-pulse cycloconverter, and a three-phase, PWM converter. Since the time-domain models are realistic models using physical components, the equivalent circuits and controllers of converters are modeled in a realistic manner. Consequently, the QMQI method is applied to the equivalent circuits and controllers for the converter models, leading to realistic and accurate converters.

In Chapter 6, demonstrative examples of LFAC-transmission systems are presented and studied. The LFAC-transmission systems are a new type of transmission

system integrating wind-farm systems to main grid systems, using an operating frequency of 20-Hz. Using the converter models developed in Chapter 4 and Chapter 5, operational studies, voltage stability studies, power transient studies, and harmonic studies are performed in this chapter.

Finally, chapter 7 provides a concise description of completed and remaining work.

CHAPTER 2

ORIGIN AND HISTORY AND LITERATURE REVIEW

In this chapter, the origin and history of both the alterative-transmission systems and numerical integration methods are presented. The main focus of this work is to propose a new modeling approach (which is named QMQI) to model power systems with nonlinearities and switching systems, and to realistically model converters (containing PWM converters, phase-control converters, and a push-pull resonant converter) for alternative transmission systems. So, the origins and history with a substantial literature survey of alternative transmission systems using converter systems and the modeling methodologies to solve these systems are presented in this chapter. Subsequent sections present origins and history according to the following subtitles:

- HVDC-transmission systems;
- LFAC-transmission systems; and
- Numerical integration methods.

2.1 HVDC-Transmission Systems

2.1.1 Overview

As a very well-known historical fact, the first commercial electrical power transmission was developed with direct current (DC) by Thomas Alva Edison in 1882. However, the difficulty in transmitting DC-power to remote utilities, which is due to low voltage, restrained its wide utilization. With the development of electrical machines (generating alternating power) and transformers (increasing or decreasing voltage levels),

alternating-current (AC) electrical systems have become worldwide dominant applications to transmit electrical energy [7]-[10]. Therefore, AC-systems have governed in terms of generation, transmission, and distribution of electrical power for over 125 years and continuing to do so.

Since power electronics (semiconductor devices) with improved rated voltage (in the case of a thyristor, the rated voltage is up to 10-kV) have become available as applications in high-power systems, HVDC-transmission systems have increasingly become a practical and commercially viable solution for economical alternative transmission systems to transmit bulk electrical power [7]. Since the first commercial HVDC-transmission system was built on the island of Gotland, Sweden in 1954, HVDC systems have spread out around the world. The highest total rated power (the greatest capacity) of HVDC transmission reached 6300-MW (the Itaipu HVDC-transmission system in Brazil [8]).

2.1.2 Usual Configurations of HVDC Systems

HVDC-transmission systems consist of two converter stations of a sending end (rectifier) and a receiving end (inverter). The rectifier transforms AC- to DC power, and the inverter transforms DC- to AC power. Each converter station is comprised of several subsystems: electrical valves, converter transformers, AC-harmonic filters, DC-harmonic filters, controllers, etc. [9]. Figure 2.1 shows the typical configurations of HVDC-transmission systems.

HVDC-transmission systems can be classified into monopolar, bipolar, and back-to-back link. The monopolar system is the cheapest and simplest configuration, since it needs only one conductor line and uses the earth as the return conductor. Also, a metallic return can be used in case the ground return is not allowed. The bipolar configuration has two conductor lines with different polarities (positive and negative), and can be seen as a

combination of two monopolar systems. Thanks to the combination of two monopolar systems, one monopolar system can be used with a ground return in case a fault condition is generated in one pole. In the back-to-back link, the two converters (rectifier and inverter) are located next to each other, and they are directly connected [10].

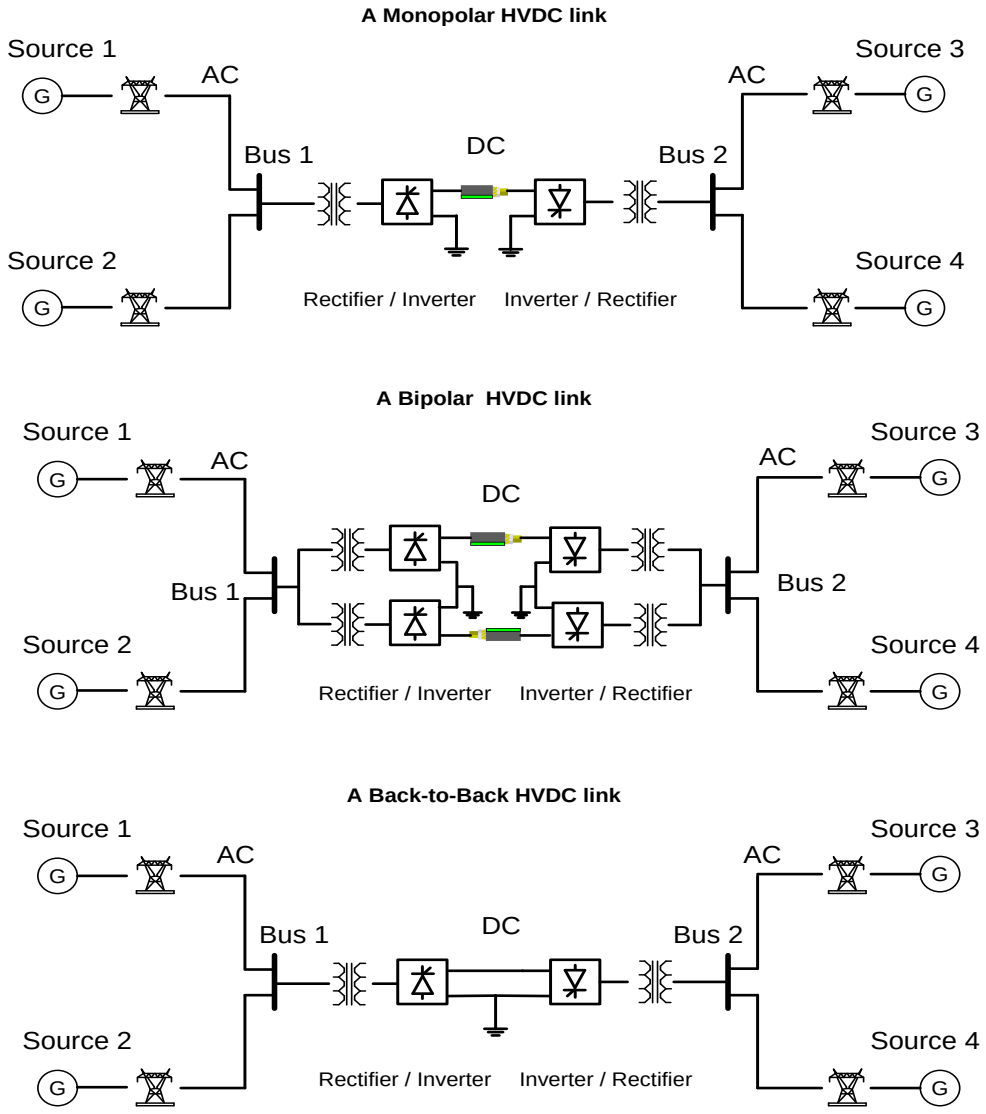

Figure 2.1: Example configurations of HVDC links: (a) monopolar HVDC link, (b) bipolar HVDC link, and (c) back-to-back HVDC link.

2.1.3 Application of HVDC Systems

The introduction of HVDC-transmission systems is justified for economical transmission from remote areas and the interconnection of asynchronous systems. High-voltage, alternating-current (HVAC) systems can exhibit some disadvantages in certain cases: (a) HVAC-transmission systems can suffer from higher electrical losses derived from the skin effect. (b) Electric-power transmission via a long cable is impractical, since high capacitance is derived from charging currents. (c) Asynchronous systems (different frequency systems) cannot be easily connected to each system. However, HVDC-transmission systems can solve these disadvantages with more economical applications [10]. Therefore, HVDC-transmission systems can be more attractive in the following cases, when compared with HVAC-transmission systems.

- Electric-power transmission from remote areas;
- Interconnection of asynchronous systems; and
- Electric-power transmission via long cable.

2.1.3.1 Application of HVDC Systems

Most of the renewable resources, such as hydro power, wind power, and solar power, are located in remote areas from power grids. As a well known fact, hydropower resources are concentrated around great rivers, such as the Amazon River and the Congo River; wind power can be located in offshore fields; and solar power resources can be easily gathered in deserts. For these renewable sources from remote areas, HVDC-transmission systems are more reasonable than HVAC-transmission systems in terms of economical aspects. The inductance and electrical losses along transmission lines can be generated by the operating frequency in AC-transmission. However, DC-transmission

systems are not affected by such inductance and electrical losses, but are dependent only on conductor dc-resistance.

In addition, HVDC-transmission systems only need one or two conductor(s): In the case of ground return, only one conductor is needed, and two conductors are needed for the metallic return in the monopolar and bipolar configurations. When compared with HVAC-transmission systems, HVDC-transmission systems can transmit the same electrical energy with fewer conductors [10], [11]. Therefore, bulk-power transmissions are possible by HVDC-transmission systems with lower losses and fewer conductors from remote areas, compared to HVAC-transmission systems.

2.1.3.2 Interconnection of Asynchronous Systems

The incipient utilizations of HVDC-transmission systems were intended to interconnect either regional or national grid systems with different frequencies or asynchronous networks. In particular, the increased population of wind turbines has accelerated the necessity of robust and stable interconnections between wind farms and power grids. Furthermore, HVDC-transmission systems have created an international exchange of surplus electrical energy among nations with different frequencies. In this case, back-to-back converters can be used without long DC-lines.

Interconnections between remote wind turbines and power grid can be offered effectively by HVDC-transmission systems, since these HVDC-transmission systems can be used as a collector system, reactive power compensator, and outlet from remote wind turbines. In this case, converters with an on/off capability can be used to transmit electrical power, and to compensate for reactive power.

These interconnections can work as a firewall between connected systems [9]-[11]. In the case of either system failure or fault in one of systems, HVDC-transmission

systems can prevent the propagation of disturbances from a faulted system, and can separate properly working systems from the contaminated system. The Northeast blackout in 2003 was an example of such an operation as a firewall against cascading outages [11], [12].

2.1.3.3 Electric-Power Transmission via Long Cable

HVDC-transmission systems can be one of the viable solutions for long underground or submarine cables. HVAC-transmission via long cable suffers from reactive components (capacitance); and therefore, cable lines have to be compensated with reactors (inductors). Even though the capacitance can be immediately compensated with inductance, the installation cost of inductors is not practical in long-distance transmission via cables. In the case of submarine cables, inductive compensation is impractical or is not economically feasible. The break-even distance between HVDC-transmission and HVAC-transmission does not exceed 50-km in economical aspects. However, the operation of HVDC cable transmission is not affected by the capacitance, and HVDC-transmission systems are feasible for lengths of hundreds of kilometers to transmit electrical power. Therefore, HVDC-transmission systems are more cost effective and are more technically feasible for long-distance cables.

2.2 LFAC-transmission Systems

2.2.1 Overview

Low-frequency, alternating-current (LFAC) transmission systems are more advanced and cost-effective technology than HVDC-transmission systems for short and intermediate distances (50-150km) [13]. The basic concept of LFAC transmission is to use frequency (16.666/20Hz) lower than nominal frequency (50/60Hz) by introducing a phase-controlled thyristor-cycloconverter. LFAC-transmission systems are very similar to HVDC-transmission systems, except that they use a cycloconverter instead of a DC-to-AC converter. This usage makes the economics of their transmission systems more effective. For example, the rating voltage of the electrical switches in their converters can be reduced, and high-voltage transmission is available, since existing transformers can be used in low-frequency transmission. Furthermore, existing technologies, such as transmission-line design and protection systems used in 60-Hz networks, can also be used for LFAC-transmission systems [14], [35].

2.2.2 Proposed Configuration of LFAC-Transmission Systems

LFAC-transmission systems are based on converters, such as AC-to-DC or DC-to-AC converters and AC-to-AC converters. Figure 2.2 shows examples of LFAC-transmission systems.

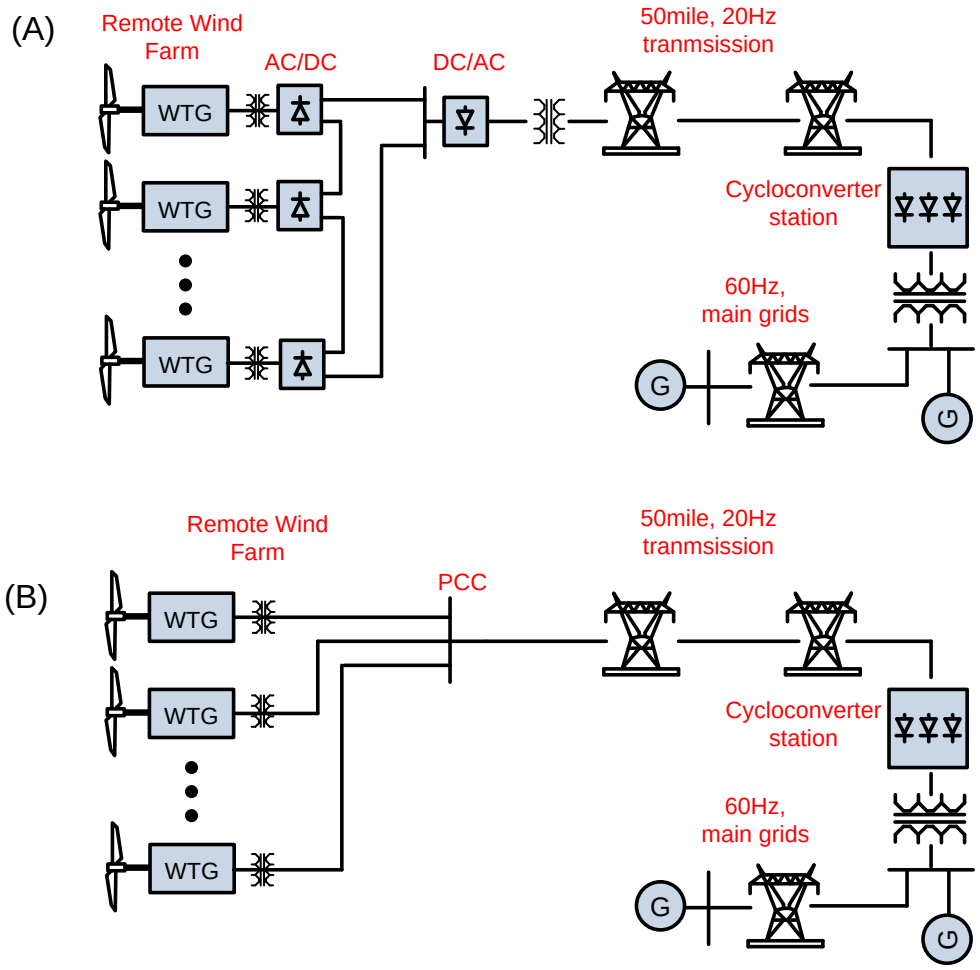

Figure 2.2: Example configurations of a LFAC-transmission system for remote wind farm: (A) DC collection and a LFAC-transmission system, and (B) LFAC collection and transmission.

In the transmission system of example (A), wind turbines are connected to each AC-to-DC converter, and electrical power from wind turbines can be collected as DC power. A DC-to-AC converter offers an interconnection between DC systems and an LFAC-transmission system, and a cycloconverter offers an interconnection between the LFAC-transmission system and a 60-Hz power grid. The example configuration (B) shows an LFAC-transmission system with doubly-fed induction machines (DFIM). Electrical power can be accumulated and transmitted using LFAC power. The LFAC-transmission

system is connected to the power grid via a phase-controlled cycloconverter in example (B).

2.2.3 Application and Benefit of LFAC-Transmission Systems

Typically, the geographic sites for wind-power plants are in remote locations and offshore locations (tens of miles from shore), so as to capture strong wind capacity. In these cases, the transmission of wind energy to main grids (central loads) is a major issue for economically suitable connections and stable, robust integration of wind farms [15]. Presently, HVAC- and HVDC-transmission systems have been researched, and well established for wind farms.

However, for the transmission from offshore wind farms of short and intermediate distance (50km-150km), HVDC-transmission systems are not economically effective, since the initial investment costs for HVDC-transmission systems are more expensive than those of onshore wind farms. The converter substation to collect and transform the electrical energy (AC into DC) is needed nearby the wind farms on the sea. That is, the installation cost is increased, and HVDC-transmission systems for offshore wind farms are not effective, compared with HVAC for short and intermediate distances [13].

LFAC-transmission systems can be applied for offshore wind farms. As in the case of Figure 2.2 (B), the converter substation is only needed in on-shore to offer the interconnection between the wind farm and the main grid via a phase-controlled cycloconverter; and thus, the initial investment can be reduced. Furthermore, LFAC transmission can increase the transmission capability, since the impedance is theoretically one-third that of a 60-Hz system.

2.3 Numerical Integration Methods

2.3.1 Overview

Numerical-integration methods are intended to solve problems of continuous mathematics, according to the process of creating, analyzing, and implementing proper algorithms. Normally, these problems, in which the variables change continuously, are directly derived from physical components in the natural world. However, the mathematical problems cannot usually be analyzed and solved exactly in explicit calculations and the necessity of approximate methods to solve these problems has been emphasized for several generations [16].

In power engineering, the mathematical model derived by physical components (circuit elements or power devices) is essential for analyzing dynamic power systems. However, these physical components cannot exactly be modeled by intuitive methods, since the physical components are normally addressed by either differential or algebraic equations. In such case, differential equations can be recomputed into algebraic equations and solved in simple computation processes by the application of numerical methods [1], [3], [17].

Many numerical integration methods have been introduced and studied for power system analysis for over a century. The backward-Euler method is one of the most popularly used methods, and is the simplest method among linear-multistep methods for power-system analysis. However, the backward-Euler method is not proper for a precise analysis of power systems, since the method is first-order accurate for solving ordinary differential-equations (ODE). Another method among well-known linear-multistep

methods is trapezoidal integration. The trapezoidal-integration method has become the dominant one among numerical methods in power-system simulation with the properties of low distortion and absolute stability (A-stable) [1].

However, trapezoidal integration is problematic when applied to network systems with nonlinearities and switching subsystems: (a) fictitious oscillations can be generated when used as a differentiator; and (b) precision problems still exist in analyses by the application of trapezoidal integration (which is second-order accurate) [1], [3], [17].

2.3.2 Trapezoidal-Integration Method

One of the most popularly used methods among numerical-integration methods for power-system analysis is trapezoidal integration. The trapezoidal-integration method has demonstrated valid accuracy and reliability in the time-domain analysis of power systems consisting of linear components. Specifically, since trapezoidal integration is simple and fast, the method is popularly used in analyses of mass power systems.

The trapezoidal-integration method belongs to the following classes of methods:

- Implicit numerical-methods; and
- Collocation methods.

The trapezoidal integration rule is an implicit method. In the case of the explicit methods, the algebraic equations of the system to be analyzed can only be represented as the relationship of the state variables at previous times. Otherwise, in the case of the implicit methods, the algebraic companion equations after the application of one among the numerical methods can be denoted as a combination of state variables at different time instances (present and previous times). The Euler method is one of the explicit

methods, and this method can be denoted as follow: $x_{n+1} = x_n + hf(t_n, x_n)$, where x_{n+1} is the unknown value at time t_{n+1}, and x_n is the known value at time t_n. The unknown state can be represented only by the previous state; therefore, the equation can be solved explicitly. However, the trapezoidal-integration method is an implicit method, and its application can yield system equations with combinations of both unknown and known values. The equations have to be modified as a compact matrix form, and can be solved by forward and backward substitution [18]. Therefore, the implicit methods take more time to compute the system equations compared with the explicit methods, since the implicit methods need more computations during each time-step. However, the implicit numerical integration methods use more information to compute unknown values, so that the methods are more robust, accurate, and stable for analyzing power transient systems. That is, the implicit numerical methods present better performance to analyze complex, stiff power systems. Since trapezoidal integration is also in the family of implicit methods, it is a robust and absolute stable method (A-stable) [1]. Assuming that the model equations of a system are stable, the results by application of trapezoidal integration are also stable.

Trapezoidal integration is one of the family of collocation methods. In more detail, the trapezoidal-integration method is a member of the Lobatto IIIA among implicit Runge-Kutta methods. The Lobatto IIIA methods are known as collocation methods and the functions (polynomial equations) for the numerical-integration methods in the methods are sampled at both end-points of the integration time-step as well as the inner collocation-point(s). The dominant error of the Lobatto IIIA is defined as order *2s-2*, where *s* is a stage value and is matched to the number of collocation points. The

trapezoidal is sampled at two collocation points of both ends of the integration time-steps. That is, the trapezoidal-integration method is a second-order accurate method. Also, the implicit Runge-Kutta methods are known as A-stable methods [19].

Therefore, the trapezoidal-integration method has become the most dominantly used method for power transient simulations with the following properties: stability, simplicity, and proper precision. For example, trapezoidal integration is implemented in the EMTP, Spice, and Virtual Test Bed [1], [3].

2.3.3 Artificial Numerical Oscillation

Trapezoidal integration is based on two assumptions: (a) systems can be linearly modeled; and (b) the state variables of the systems vary linearly within each time-step [18]. In the two conditions, the trapezoidal-integration method has demonstrated numerically stable characteristics and proper precision to analyses power systems. However, most power systems integrating renewable resources include nonlinear components and switching systems, such as saturable core transformers and converters. Trapezoidal integration generates numerical oscillations, while the method is applied to nonlinearities and switching systems. Numerical oscillations are not natural phenomena from systems to be analyzed, but are artifacts derived from the application of the trapezoidal-integration method. Particularly speaking, in the case of analyzing power systems with nonlinearities and switching subsystems, the state variables of network models suddenly change and numerical oscillations are frequently generated. Also, it is known that numerical oscillations can be shown at certain combinations of integration time-steps and natural frequencies of a system to be analyzed [17]. These phenomena

have been frequently found during the state changes of electrical switches in switching systems. When the valves of switching systems change the state from on-state to off-state, the combination of the integration time-step and the natural frequency of the switching systems could lead numerical solutions to oscillation zones (Note that the reason for the phenomena is mathematically analyzed in the next section). In this case, the switching systems can generate numerical oscillations, which can be a direct reason for switching misfiring and failure. Figure 2.3 shows the true solutions and the oscillatory solutions, derived from the trapezoidal-integration methods, of a three-phase, six-pulse converter: (a) the true value of line-to-line voltage (A-B); and (b) the results by the application of the trapezoidal integration of line-to-line voltage (A-B). The results show that the trapezoidal-integration method suffers from certain fictitious oscillations as reported in previous publications [1], [3], [17].

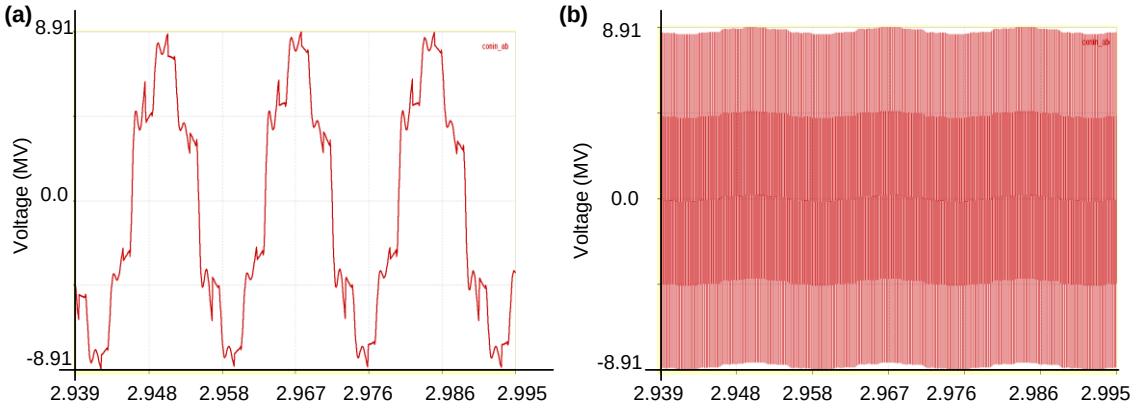

Figure 2.3: Numerical oscillations: (a) the true value of line-to-line voltage; and (b) the results by the application of the trapezoidal integration of line-to-line voltage of a six-pulse converter.

2.3.4 Elimination of Numerical Oscillations

In an analysis of power systems with nonlinearities and switching subsystems using trapezoidal integration, numerical oscillations have decreased the simulation efficiency and precision. An additional algorithm to eliminate or suppress the problems is needed. Thus, several approaches have been proposed for suppressing numerical oscillations. The most well-known methods can be presented as follows:

- External damping (stabilizer method);
- Critical damping adjustment (CDA); and
- Wave digital filter (WDF).

The external damping method adds fictitious resistance (stabilizer) to systems with an artificial, numerical, and oscillatory solution. Fictitious resistance can be added in parallel with the inductances and in series with the capacitance [20], [21], [22]. However, numerical stabilizers slightly change both the structure and the state equations of the network model and cannot flawlessly eliminate fictitious oscillation. The major disadvantage of adding fictitious damping using stabilizers is that the rest of the normal network system response is distorted by the phase errors introduced by the damping [20].

The most widely used method is critical damping adjustment (CDA). This method uses a combination of both trapezoidal integration and the backward-Euler method. The backward-Euler method is free of numerical oscillations, and therefore, is used during critical conditions when the switching systems change the state. However, the method requires variable time-steps, leading to different sampling rates. The sampling rate in critical conditions is twice that during standard conditions, and the variable time-steps

require the companion matrices of all devices to be recomputed for critical conditions. Furthermore, the backward-Euler method is first-order accurate so that the combination of both the trapezoidal integration and backward-Euler method lowers the degree of precision [1], [17], [20].

The WDF method is also a well-known implementation used to suppress numerical oscillations. This method uses two parameters, referred to as incident and reflected voltage wave quantities and port resistance. With these quantities, the WDF method establishes the series and parallel adaptors originating from the physical components, and the power networks can be modeled by connecting the series and parallel adaptors [2], [4]. However, the WDF is an auxiliary algorithm added to analog systems to suppress fictitious oscillation, and the method can generate some distortions unrelated to the true values [2].

Therefore, the trapezoidal-integration method is not suitable for power systems with nonlinearities and switching systems, even though additional algorithms can eliminate or suppress numerical oscillations. The additional algorithms require a complex modeling process as well as decreased simulation accuracy. Better simulation methods are needed for power systems interconnecting renewable resources and grid systems.

CHAPTER 3

A NEW MODELING APPROACH: THE QMQI METHOD

A new modeling approach is introduced for modeling and analysis of the mixed power-systems with nonlinearities and switching subsystems, such as the HVDC-transmission systems and the LFAC-transmission systems. The modeling method uses a combination of model quadratization (quadratized models) and quadratic integration and the combination method is denoted as the QMQI method for brevity. This QMQI method is suitable for power systems of switching subsystems with highly nonlinear components such as saturable core reactors and transformers, since the method is free of numerical oscillations, and nonlinear equations are treated without simplification or approximation of nonlinear equations.

In this chapter, the superior properties of the quadratic-integration method are presented in comparison to other numerical methods of trapezoidal integration and cubic integration, which are in the family of collocation methods among implicit Runge-Kutta (RK) methods. For this purpose, several simple switching systems are modeled and simulated by the application of three numerical-integration methods. Also, the modeling methodology using QMQI is carefully explained with the modeling process of a push-pull resonant converter. Subsequent sections present the performance properties and the modeling process using the QMQI method, according to the following subtitles:

- Basic concept of the quadratic integration;
- Performance properties in comparison to other methods; and

- Detailed modeling process using QMQI.

3.1 Basic Concept of Quadratic Integration

The quadratic-integration method is a special case in a class of methods known as collocation methods [1] and is sampled at three collocation points, as shown in Figure 3.1.

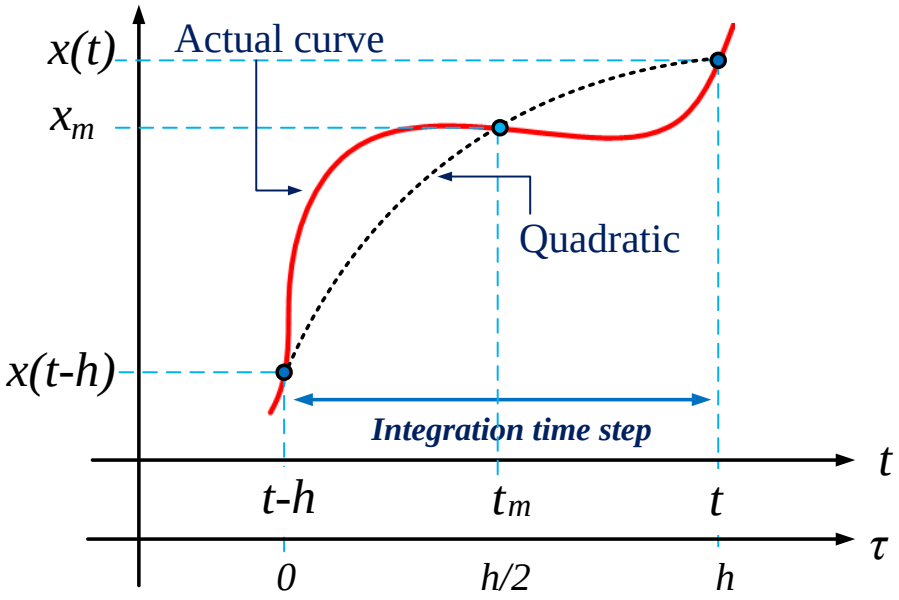

Figure 3.1: Graphical illustration of quadratic integration.

Quadratic integration is based on two concepts: (a) The time-domain functions vary quadratically within the integration time-step; and (b) the model of the system is linear or quadratic. With these assumptions, the general form of the time-domain functions can be written within the integration time-step as follows:

$$x(\tau) = a + b \cdot \tau + c \cdot \tau^2 \qquad (3.1.1)$$

The three parameters of a, b, and c in Equation (3.1) can be expressed as the sampled values of $x(t\text{-}h)$, x_m, and $x(t)$ at the three collocation-points. The results are as follows:

$$a = x(t-h)\,, \tag{3.1.2}$$

$$b = \frac{1}{h}\left(-3x(t-h) + 4x_m - x(t)\right), \text{ and} \tag{3.1.3}$$

$$c = \frac{2}{h^2}\left(x(t-h) - 2x_m + x(t)\right), \tag{3.1.4}$$

where x_m is the value x at the mid-point (t_m).

Then, the integration of the quadratic function is straightforward. The procedure will be illustrated with a first-order, dynamical system:

$$\frac{dx(t)}{dt} = Ax(t) \tag{3.1.5}$$

The equation above is integrated from *t-h* to *t* and from *t-h* to *t-h/2*, yielding:

$$x(t) - x(t-h) = A \cdot \int_{t-h}^{t} x(\tau)d\tau \text{ , and} \tag{3.1.6}$$

$$x_m - x(t-h) = A \cdot \int_{t-h}^{t-h/2} x(\tau)d\tau\,. \tag{3.1.7}$$

Upon evaluation and rearrangement of the integrals, the following matrix equation is obtained (algebraic-companion form), which can be applied repetitively to provide the solution to the differential equation:

$$\begin{bmatrix} \frac{h}{24}A & I - \frac{h}{3}A \\ I - \frac{h}{6}A & -\frac{2h}{3}A \end{bmatrix} \cdot \begin{bmatrix} x(t) \\ x_m \end{bmatrix} = \begin{bmatrix} \left(I + \frac{5h}{24}A\right) \\ \left(I + \frac{h}{6}A\right) \end{bmatrix} \cdot x(t-h) \tag{3.1.8}$$

The algebraic form of Equation (3.1.8) can be used as a solution method of ordinary-differential equations (ODE). In this case, quadratic integration has demonstrated the following advantages: (a) the natural elimination of artificial numerical oscillations; and (b) better performance in stability and accuracy than those of trapezoidal integration. These performance properties are presented in the next subsection.

3.2 Properties of Quadratic Integration

In this section, the superior properties of the quadratic integration (QI) method are demonstrated in comparison to other collocation methods of trapezoidal and cubic integration (TI and CI). Quadratic and cubic integration are extensions of trapezoidal integration, which can be viewed as a collocation method. In more detail, the three numerical integration methods are the members of *Lobatto IIIA* among implicit Runge-Kutta methods. The *Lobatto IIIA* methods are known as collocation methods and the functions (polynomial equations) for numerical integration methods are sampled at both end-points of the integration time-step as well as the inner collocation point(s). The three numerical integration methods of TI, QI, and CI are a two-, three-, and four-collocation method, respectively, as shown in Figure 3.2. Also, other forms of collocation methods can be induced while the collocation points are increased.

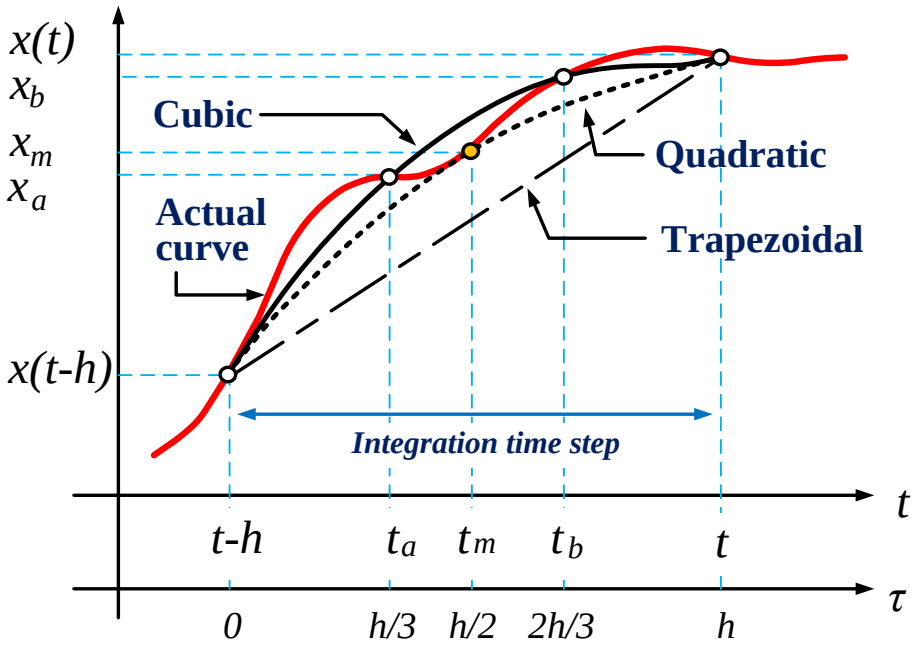

Figure 3.2: Graphical illustration of the trapezoidal, quadratic, and cubic-integration method

Since the numerical integration methods are sampled at collocation points, high-order methods offer more accurate simulation results in the time-domain analysis. However, the computation burden and calculation complexity are substantially increased according to the number of collocation points. For example, a first-order dynamical system is presented in Equation (3.2.1), and the algebraic companion form (ACF) of the dynamical system derived from the three numerical-integration methods (TI, QI, and CI) are induced, as shown in Equations (3.2.2) to (3.2.4), respectively.

$$\frac{dx(t)}{dt} = Ax(t) \tag{3.2.1}$$

The ACF by the application of TI is at each time-step:

$$-\frac{h}{2}A \cdot x(t) = -\frac{h}{2}A \cdot x(t-h) \tag{3.2.2}$$

The ACF by the application of QI is at each time-step:

$$\begin{bmatrix} -\frac{h}{6}A & -\frac{2h}{3}A \\ \frac{h}{24}A & -\frac{h}{3}A \end{bmatrix} \cdot \begin{bmatrix} x(t) \\ x_m \end{bmatrix} = \begin{bmatrix} \frac{h}{6}A \\ \frac{5h}{24}A \end{bmatrix} \cdot x(t-h) \tag{3.2.3}$$

The ACF by the application of the CI is at each time-step:

$$\begin{bmatrix} -\frac{h}{8}A & -\frac{3h}{8}A & -\frac{3h}{8}A \\ -\frac{h}{72}A & -\frac{19h}{72}A & \frac{5h}{72}A \\ 0 & -\frac{4h}{9}A & -\frac{h}{9}A \end{bmatrix} \begin{bmatrix} x(t) \\ x_a \\ x_b \end{bmatrix} = \begin{bmatrix} \frac{h}{8}A \\ \frac{h}{8}A \\ \frac{h}{9}A \end{bmatrix} x(t-h) \tag{3.2.4}$$

where : x_m, x_a, and x_b are the state variables at t_m, t_a, and t_b, respectively. Note: assuming that the number of state equations is n, the matrix of A is an n-*by*-n matrix, and the total number of state variables from TI, QI, and CI is n, $2n$, and $3n$, respectively.

3.2.1 Comparison of the Three Numerical Integration Methods

The QI is compared to TI, which has been popularly used in time-domain analyses of power systems, and CI, which is an extension version of TI and QI. Though the comparison, why the quadratic-integration method is introduced, and why other higher-order collocation methods are not considered as a solution method to analysis power systems with nonlinearities and switching subsystems are presented. Also, the superior properties of QI are presented. For this purpose, the three numerical integration methods are compared in four properties of accuracy, computational speed, stability, and numerical oscillations, using simple example systems with electronics.

3.2.1.1 Comparison in Accuracy and Computational Speed

The accuracy and computational speed of QI are compared to those of TI and CI, since the simulation reliability and applicability to massive power systems depend on the two properties. The accuracy and computational speed of the three numerical integration methods are compared by using an example system, as shown in Figure 3.3.

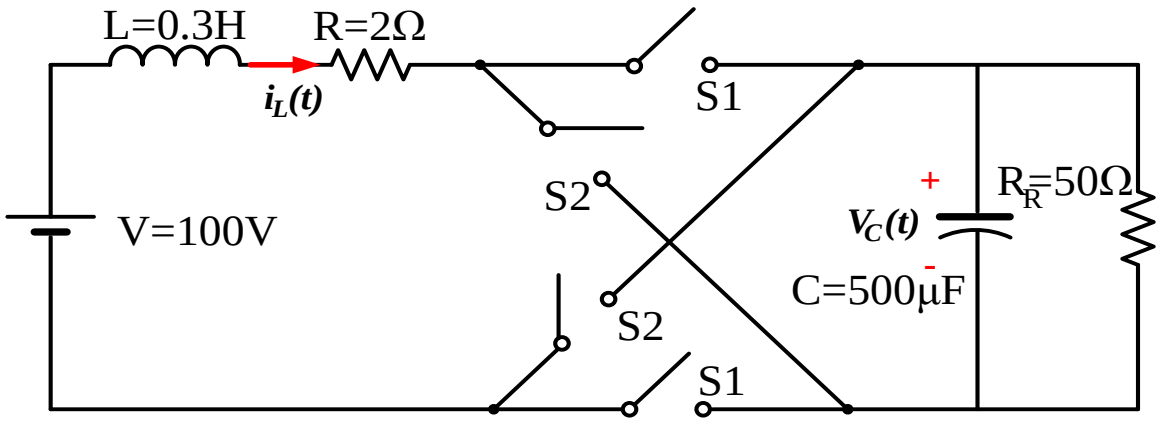

Figure 3.3: A simple switching system with ideal electronics.

The simple switching system consists of ideal electronics and the passive components of two resistors, an inductor, and a capacitor. The ideal electronics are operated in the sequence of switching given the following: Switches *S1* are closed at $t=0.0T+kT$ and opened at $t=0.5T+kT$, and switches *S2* are reversely operated. The switching period T is 0.02 seconds, and $k=\{0,1,2,\ldots\}$.

The simulation results from numerical methods are compared to those of the analytical solution. The analytical solution is calculated by the application of the Laplace transform and the inverse Laplace transform. Figure 3.4 shows the inductor current and the capacitor voltage from the analytical solution.

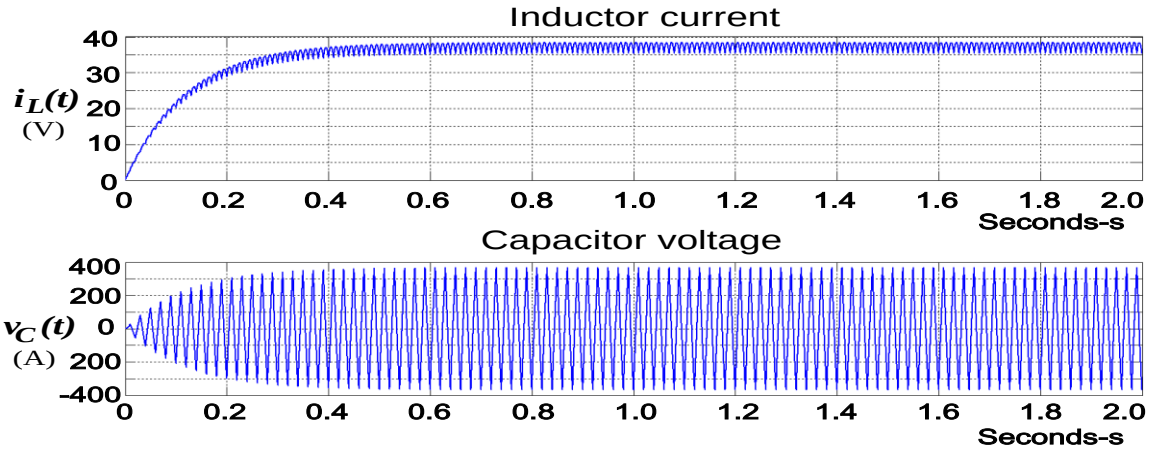

Figure 3.4: Inductor current and capacitor voltage from the analytical solution.

The results by application of the three numerical integration methods are so similar in form, like the waveforms of Figure 3.4, that the difference from the analytical solutions cannot be recognized without a detailed analysis. So as to show the error clearly, the absolute errors of inductor currents are presented between the numerical solutions from the numerical-integration methods and the analytical solutions from the Laplace

transform. The absolute error is denoted in mathematical form as follows:

$$Error=abs(\ i_{LT}(t)-i_N(t)\ ), \qquad (3.2.5)$$

where i_{LT} and i_N are the inductor current from the analytical solution and the three-numerical integration methods, respectively. Figure 3.5 shows the absolute errors of the inductor currents.

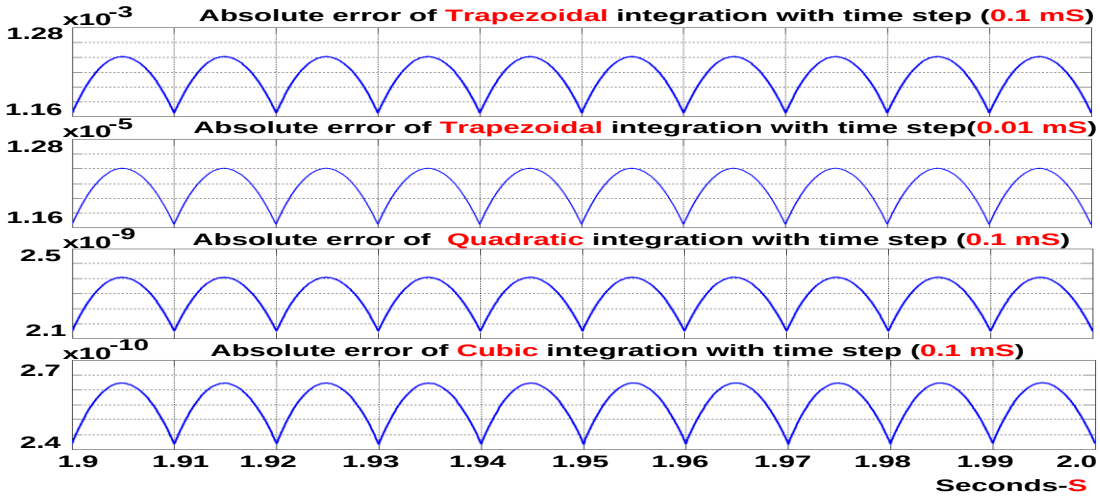

Figure 3.5: Absolute error of the inductor current according to applied methods.

As Shown in Figure 3.5, QI and CI substantially improve simulation accuracy compared to the TI method, while the simulation is performed with the same time-step of 0.1 micro-seconds. Next is the comparison of the maximum error during the entire simulation-time of 2.0 seconds, as shown in Table 3.1.

Table 3.1: Maximum Value of the Absolute Error during Simulation Time.

Time-step (seconds)	Maximum errors during simulation period		
	Trapezoidal	Quadratic	Cubic
0.001	$1.243\ x10^{-1}$	$2.299x10^{-5}$	$2.554x10^{-6}$
0.0001	$1.241x10^{-3}$	$2.305x10^{-9}$	$2.640x10^{-10}$
0.00001	$1.241x10^{-5}$	$1.365x10^{-10}$	$6.172x10^{-11}$

The results of Table 3.1 can be analyzed theoretically. The three collection-methods are special cases of the *Lobatto IIIA*, the family of the implicit Runge-Kutta methods, since the definition of the *Lobatto IIIA* is exactly matched to the *butcher-tableau* of the three collocation methods [23]. The dominant error of the *Lobatto IIIA* is defined as order *2s-2*, where *s* is a stage value and is matched to the number of collocation points. That is, the TI , QI , and CI methods can be denoted as second-, fourth-, and sixth-order methods respectively, in terms of accuracy. Mathematically, the dominant error of the three collocation-methods is denoted as:

$$E_{Trap} = O(h^2),\ E_{Quad} = O(h^4),\ \text{and}\ E_{Cubic} = O(h^6). \qquad (3.2.6)$$

In Table 3.1, the absolute error from TI is quadratically decreasing according to the rule of Equation (3.2.6), while the time-step is decreasing; also, QI is quartically decreasing until the absolute error is bigger than 10^{-10}. However, the absolute error violates the rule of Equation (3.2.6), when the absolute error is smaller than 10^{-10}. The round-off error in the computer calculation is dominant, compared to the truncation-error of the applied methods. Therefore, the CI method is demonstrated as the most accurate method among the three collocation methods, while TI is the worst accurate method. The QI is also an accurate method, and the difference of the absolute error between QI and CI is trivial (ten times).

Next, the computational effort of the three collocation methods is compared also by using the simple switching system of Figure 3.3. Table 3.2 presents the computational effort of the collocation methods during the simulation time of 1.0 second. In the simulation, the memory for the state variables is not allocated to offer a similar condition in which other processing is dominantly involved, such as a control algorithm and data

processing for references of the control algorithm. For example, QI needs sampling data at mid-points (t_m) as well as present points (t). Assuming that the number of state variables is n, the number of state variables for the TI, QI, and CI methods are n, $2n$, and $3n$, respectively. That is, the computational effort for QI needs more than twice that for TI, while the CI needs more than three times, as shown in Table 3.2.

Table 3.2: Computational Effort-One Second Simulation

Time-step (seconds)	The computational cost (seconds)		
	Trapezoidal	Quadratic	Cubic
0.0001	0.700283	1.674141	2.761643
0.00001	101.269275	238.64339	473.08906

Therefore, the collocation methods are listed in the order of computational speed: TI is the fastest, QI is the second-fastest, and CI is the latest, while the same time-step is used. However, it is worth noting that QI with a time-step of 100 microseconds, as compared to TI with a time-step of 10 microseconds, offers more accurate results (around fourth orders of magnitude, as shown in Table I) with a small fraction of the execution time (about 2% of the execution time of TI, as shown in Table II).

3.2.1.2 Comparison in Numerical Stability and Numerical Oscillations

The next property to be compared is the numerical stability: A-stability and the possibility of numerical oscillations. Most of the Runge-Kutta (RK) methods had historically been explicit RK-methods. The explicit RK-methods generate stability problems since the region of the A-stability is bounded: the explicit RK-methods should present unstable results in some cases, even though the system to be analyzed is stable. Thus, implicit RK methods are considered, since implicit RK methods are A-stable methods [24]. In particular, the modeling of power systems with nonlinearities and switching subsystems requires a large region of A-stability for rapid and dramatic

variations of states. Here, the comparison of the three collocation-methods is presented based on A-stability. For this purpose, a first-order dynamic system is introduced as $\dot{x}(t) = \lambda x(t)$. The digital and true solution of the dynamical system can be represented as $x(t)=e^z \cdot x(t-h)$ within [$t-h$, t], where $z=\lambda h$ *and* λ represents complex numbers. The stability function of RK-methods is represented as follows:

$$e^Z = R(z) + O(h^n) = 1 + zb^T (I - zA)^{-1} \cdot 1 + O(h^n) \quad (3.2.7)$$

Note that Equation (3.2.7) is generally used to analyze the stability of RK methods and is easily found in previous literature [24], [25]. Assuming that the truncation error of $O(h^n)$ is trivial and negligible, the numerical solution can be represented as $x(t)=R(z) \cdot x(t-h)$ and the stability of the three collocation-methods can be investigated with the stability function $R(z)$ from Equation (3.2.8) to Equation (3.2.10).

$$Trapezoidal: R(z) = \frac{2+z}{2-z}, \quad (3.2.8)$$

$$Qudaratic: R(z) = \frac{z^2 + 6z + 12}{z^2 - 6z + 12}, \quad (3.2.9)$$

$$\text{and } Cubic: R(z) = \frac{z^3 + 11z^2 + 54z + 108}{-z^3 + 11z^2 - 54z + 108}. \quad (3.2.10)$$

The region of absolute stability satisfies $|R(z)| \leq 1$ and the numerical methods are *A-stable* if the region of absolute stability includes the entire left-half plane of z-coordination [25]. That is, the numerical solutions from *A-stable* methods are stable with the proper time-step, while the system to be analyzed is stable. Figure 3.6 shows the contours of Equations from (3.2.8) to (3.2.10).

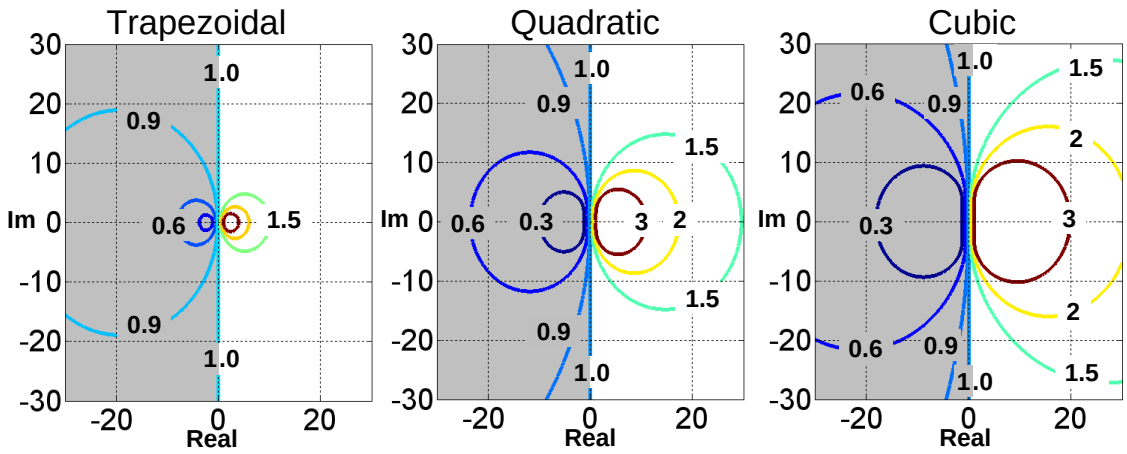

Figure 3.6: Contours of stable functions and zones of A-stability.

As shown in Figure 3.6, the contours of $|R(z)|$, derived from the three collocation methods, have magnitudes that are equal to one or smaller than one in the entire left-half plane. That is, the three collocation methods of the TI, QI, and CI are *A-stable*.

For a time-domain analysis of power systems with nonlinearities and switching systems, the most important property is the possibility of numerical oscillations. These numerical oscillations are not natural phenomena from systems but rather fictitious phenomena derived from numerical integration methods. Numerical oscillations are usually generated, when the state variables of the algebraic equations, derived from numerical integration methods, are suddenly changed. These phenomena have been frequently found in time-domain analyses of switching systems and nonlinearities using TI. Here, the mathematical reason for numerical oscillations and the comparison of the three-collocation methods in the possibility of numerical oscillations are presented. For this purpose, the numerical solution of the first-order dynamic system is also used: $x(t)=R(z)\cdot x(t-h)$. The numerical oscillations are generated while the stability function $R(z)$

is negative. Assuming that $R(z)<0$ in the numerical solution above, the direction of the state variable $x(t)$ is changed at each time-step, and the numerical solution should oscillate, based on true solutions. Figure 3.7 and Table 3.3 represent the zones free of numerical oscillations. Note that the zones (shaded parts) are computed with the equations from (3.2.8) to (3.2.10). As shown in Figure 3.7, quadratic and quartic integration are totally free of numerical oscillations, assuming that $Im(z)$ is zero and z is real numbers. Since power components, such as an inductor, capacitor, resistor, etc., are modeled with algebraic and differential equations (in which the coefficients of the equations are real numbers in the power system analysis), the set of z (λh) represents real numbers. Therefore, it can be concluded that quadratic and quartic integration are totally free of numerical oscillation in time-domain analyses. Note that the zones (free of numerical oscillations) of quartic integration are presented to demonstrate that the collocation methods with odd numbers of collocation points are free of numerical oscillations.

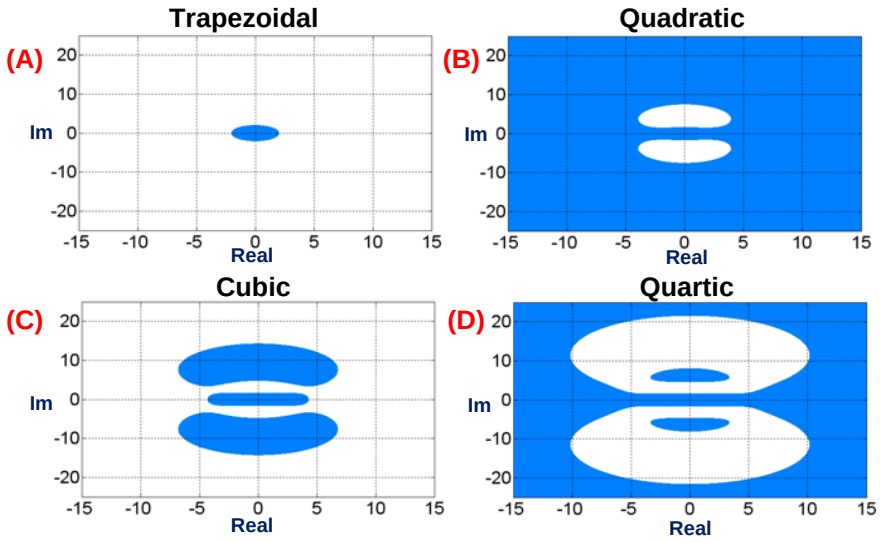

Figure 3.7: Zone(s) free of artificial numerical oscillations of the three methods (shown as shaded regions).

Table 3.3: Zone free of numerical oscillation while Im(z) is zero.

Method	TI	QI	CI
Free zone	$-2 < z \leq 2$	Totally free	$-4.3 < z \leq 4.3$

Here, a simple switching system, a half-wave diode-rectifier, is introduced to graphically verify whether QI is totally free of numerical oscillations. As shown in Figure 3.8, the electronics is a piecewise linear model, in which the diode is represented as $R_{on}=10^{-2}$ during on-state and as $R_{off}=10^{7}$ during off-state.

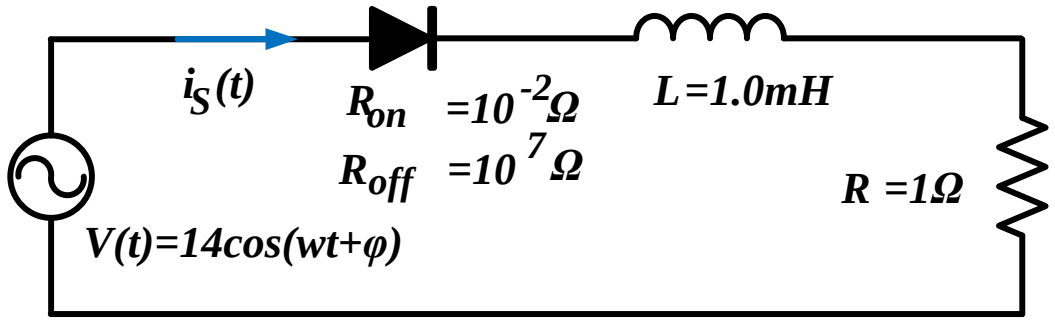

Figure 3.8: An example system of a half-wave diode rectifier.

Using the three numerical integration methods, the diode voltage is analyzed from 0.0 to 0.05 seconds, as shown in Figures 3.9 to 3.11. Note that all simulation conditions are the same, except for the applied methods in this analysis and the integration time-step is 10^{-6}.

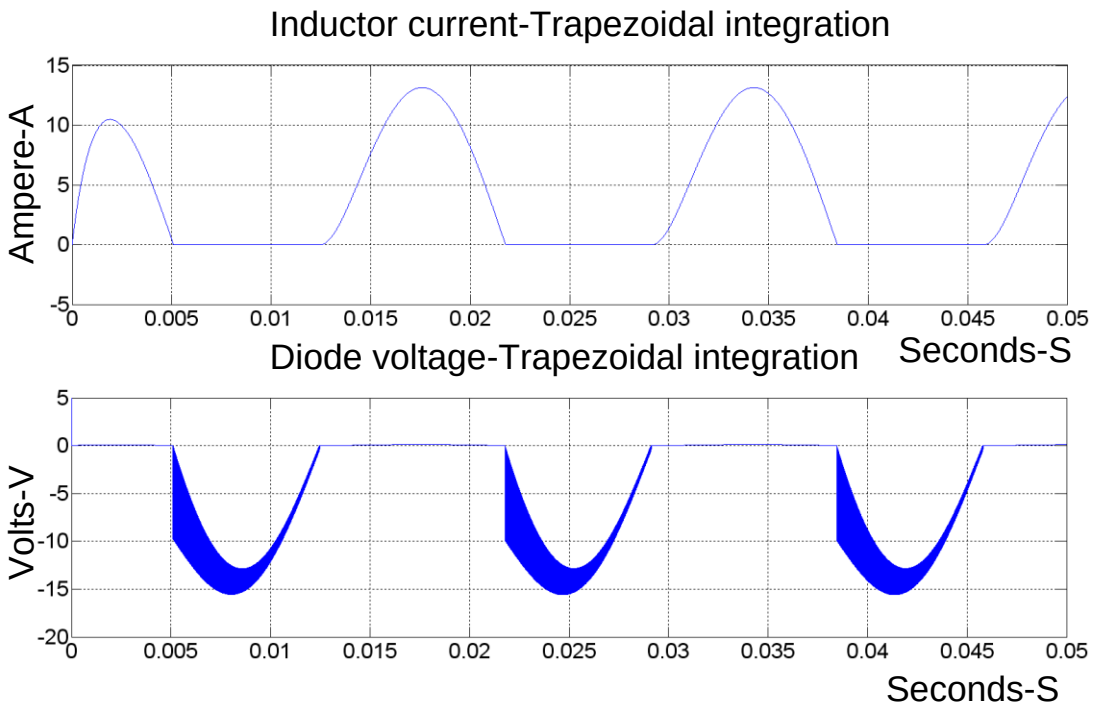

Figure 3.9: Inductor current and diode voltage-Trapezoidal integration.

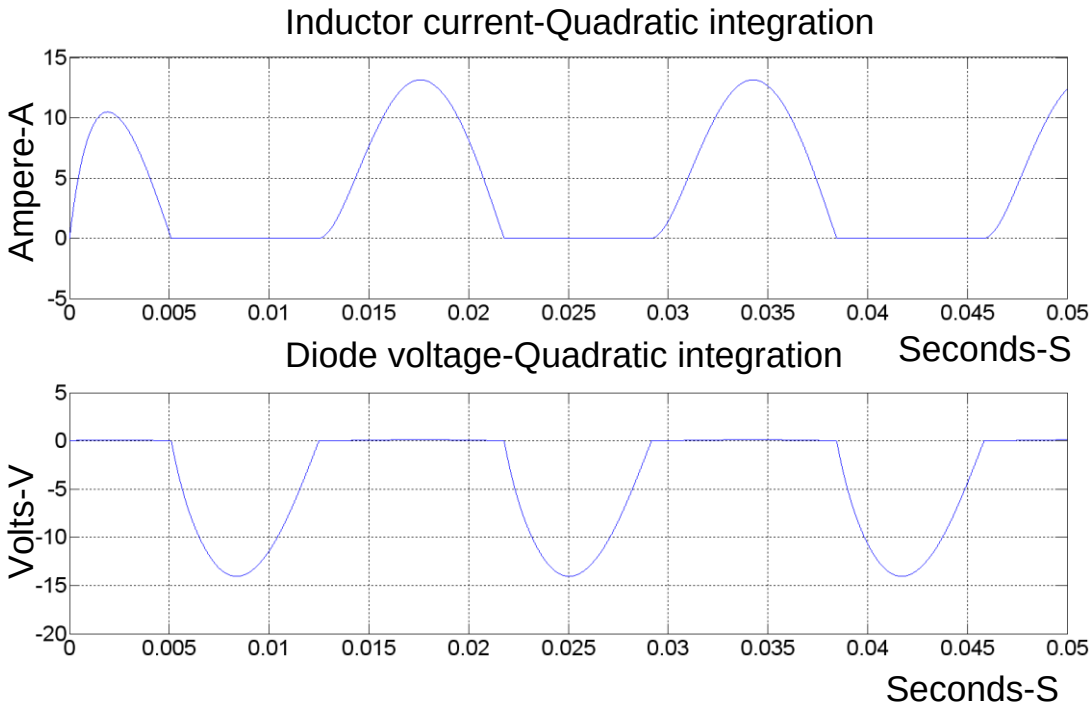

Figure 3.10: Inductor current and diode voltage-Quadratic integration.

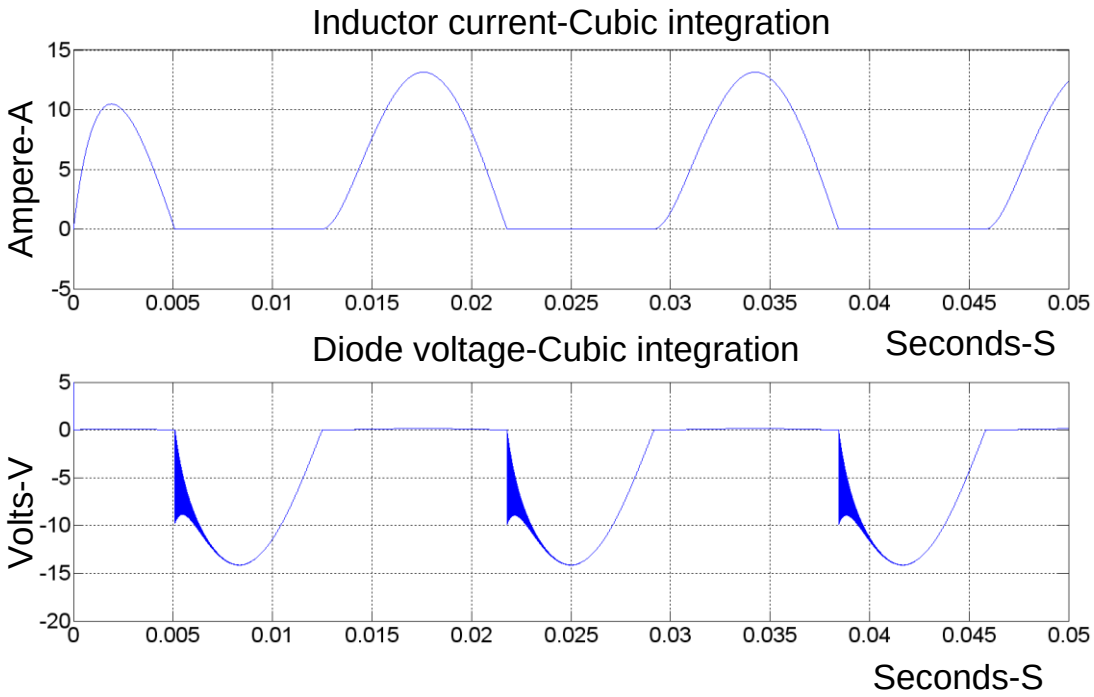

Figure 3.11: Inductor current and diode voltage-Cubic integration.

As mentioned in Table 3.3, TI and CI should generate numerical oscillations, while $|z|$ is bigger than 2 and *4.3*, respectively. Thus, the value of z is calculated when the diode in Figure 3.8 resides in on-state and in off-state: $z \approx -10^{4}$ in off-state and $z \approx -10^{-3}$ in on-state. That is, TI and CI generate fictitious oscillations during off-state, while QI is free of fictitious oscillations as shown in Figure 3.10.

In summary, quadratic integration is not only free of numerical oscillations, which are a main reason of switching malfunction in switching systems, but is also an accurate and stable method, leading to a reliable analysis of power systems with a wide variation of state variables. Other collocation methods with high-order collocation points could also be used for power systems analysis. However, they require a high computational burden and modeling complexity, and even some (even-number collocation methods) of them may generate numerical oscillations with a high possibility in an analysis of power systems with nonlinearities and switching systems. For power systems interconnecting

renewable resources and grid systems, such as HVDC-transmission systems and LFAC-transmission systems, quadratic integration seem to be the best simulation method, with great accuracy and stability.

3.3 Model Quadratization and Quadratic Integration (QMQI)

In this section, the QMQI method is introduced to model both devices and power systems with nonlinear components and switching components. Generally, power systems have been modeled linearly with the application of the trapezoidal-integration method: nonlinearities and switching systems are modeled by a combination of TI and additional methods, such as numerical dampers and critical damping adjustment methods (CDA) after the linearization of nonlinear equations. However, these methods do not only decrease simulation accuracy, but also accompany modeling complexity.

The QMQI allows exact and realistic models of power systems with nonlinear and switching components in simplicity, since QI is totally free of numerical oscillations, and model quadratization permits the possibility to solve nonlinearities in a nonlinear concept. The modeling methodology using QMQI is performed in four steps: (a) a device is written in state-space equations consisting of algebraic, differential, and nonlinear equations; (b) model quadratization is performed on state-space equations to transform nonlinear (high-order) equations into a combination of linear and quadratic equations; (c) the QI method is applied to the quadratized model to induce algebraic equations from the differential equations; and (d) the algebraic equations are computed by Newton's method. Note that in the time-domain simulation the processes are repeated at each time-step. The

modeling process is explained in the following subsections, using a push-pull, resonant converter with a single-phase saturable transformer shown in Figure 3.12 [26].

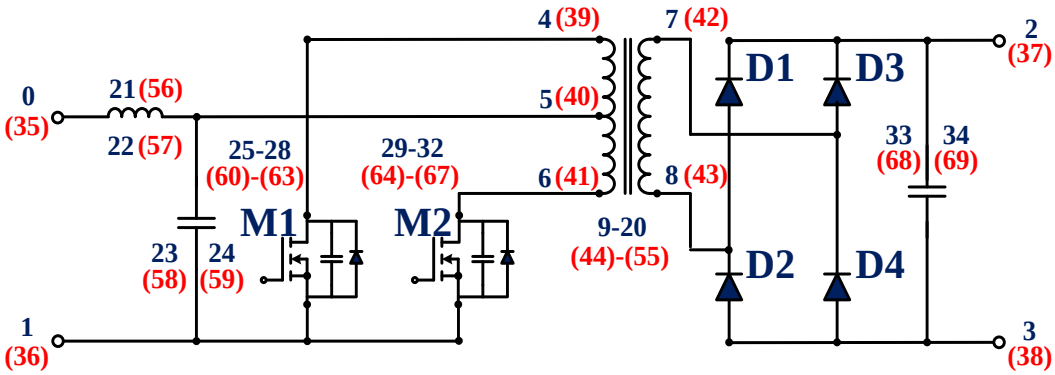

Figure 3.12: An equivalent model of a push-pull resonant converter

3.3.1 State-Space Equations

The push-pull, resonant converter in Figure 3.12 consists of a single phase saturable-transformer, MOSFETs, diodes, inductors, and capacitors. Each component is modeled and merged based on Kirchhoff's law to form an entire model of the push-pull converter. Since the modeling process of each component is the same as each other, the modeling process of a single-phase saturable transformer is only presented. The single-phase saturable transform consists of winding resistance (r_1 and r_2), leakage reactance (L_1 and L_2), core loss (r_C), and magnetizing reactance (L_m), as shown in Figure 3.13.

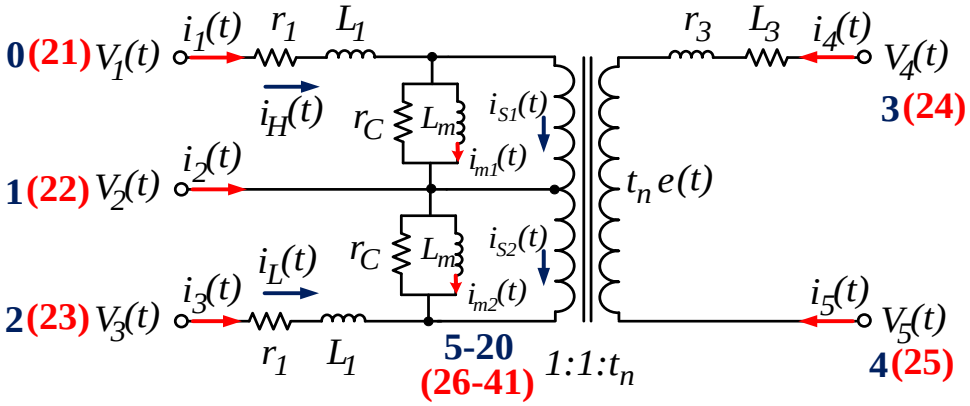

Figure 3.13: An equivalent model of a single-phase saturable transformer

The state-space equations of the transformer shown in Figure 3.13 can be represented as follows:

$$i_1(t) = i_H(t) \tag{3.3.1}$$

$$i_2(t) = -i_H(t) - i_L(t) \tag{3.3.2}$$

$$i_3(t) = i_L(t) \tag{3.3.3}$$

$$i_4(t) = -\frac{1}{t_n} i_{S1}(t) - \frac{1}{t_n} i_{S2}(t) \tag{3.3.4}$$

$$i_5(t) = \frac{1}{t_n} i_{S1}(t) + \frac{1}{t_n} i_{S2}(t) \tag{3.3.5}$$

$$0 = i_S(t) - i_{S1}(t) - i_{S2}(t) \tag{3.3.6}$$

$$0 = -e(t) - r_C i_{m1}(t) + r_C i_H(t) - r_C i_{S1}(t) \tag{3.3.7}$$

$$0 = e(t) + r_C i_{m2}(t) + r_C i_L(t) + r_C i_{S2}(t) \tag{3.3.8}$$

$$0 = -v_1(t) + v_2(t) + e(t) + r_1 i_H(t) + L_1 \frac{d}{dt} i_H(t) \tag{3.3.9}$$

$$0 = -v_2(t) + v_3(t) + e(t) - r_1 i_L(t) - L_1 \frac{d}{dt} i_L(t) \tag{3.3.10}$$

$$0 = -v_4(t) + v_5(t) + t_n e(t) - \frac{r_2}{t_n} i_S(t) - \frac{L_2}{t_n} \frac{d}{dt} i_S(t) \tag{3.3.11}$$

$$0 = e(t) - \frac{d}{dt} \lambda(t) \tag{3.3.12}$$

$$0 = i_{m1}(t) - i_0 \left| \frac{\lambda(t)}{\lambda_0} \right|^n sign(\lambda(t)) \tag{3.3.13}$$

$$0 = i_{m2}(t) - i_0 \left| \frac{\lambda(t)}{\lambda_0} \right|^n sign(\lambda(t)) \tag{3.3.14}$$

where t_n is the transformer ratio, λ_0 is the nominal constant flux, and i_0 is the nominal magnetizing current.

The state-space equations were written in linear, differential, and nonlinear equations of exponent *n*, as shown in Equations (3.3.1) to (3.3.14).

3.3.2 Model Quadratization (Quadratic Model)

The high-order equations, such as Equations (3.3.13) and (3.3.14), are quadratized as linear and quadratic equations, in which the degree is not bigger than two. Generally, the magnetizing current of saturable transformers can be expressed with the magnetic flux of exponent *n* from 9 to 13. Thus, the exponent *n* of Equation (3.3.13), which is representing a relationship between magnetizing current and magnetizing flux linkage, is selected into 9 and the model quadratization is performed on the following equation.

$$0 = i_{m1}(t) - i_0 \left| \frac{\lambda(t)}{\lambda_0} \right|^9 sign(\lambda(t)) \tag{3.3.15}$$

The resulting equations by application of model quadratization are as follows:

$$0 = i_{m1}(t) - \frac{i_0}{\lambda_0} \lambda(t) z_1(t) \tag{3.3.16}$$

$$0 = z_1(t) - z_2^2(t) \tag{3.3.17}$$

$$0 = z_2(t) - z_3^2(t) \tag{3.3.18}$$

$$0 = \lambda_0^2 \cdot z_3(t) - \lambda^2(t) \tag{3.3.19}$$

The magnetizing current, a nonlinear equation of exponent 9, is represented in quadratic forms with additional states from z_1 to z_3.

3.3.3 Application of Quadratic Integration (QI)

Numerical integration methods are introduced to solve the differential equations, since these differential equations cannot be calculated in explicit mathematics. An approximation method is required, and QI is selected with the advantages explained in the previous section to induce algebraic forms from differential equations. For example, quadratic integration is applied to Equation (3.3.12), and the algebraic equations are represented at each time-step as follows:

$$0 = \frac{h}{6}e(t) - \lambda(t) + \frac{2h}{3}e_m + \frac{h}{6}e(t-h) + \lambda(t-h) \tag{3.3.20}$$

$$0 = -\frac{h}{24}e(t) - \lambda_m + \frac{h}{3}e_m + \frac{5h}{24}e(t-h) + \lambda_m(t-h) \tag{3.3.21}$$

All differential equations from (3.3.9) to (3.3.12) in the state-space equations can be denoted as algebraic equations by the application of QI, and the saturable transformer can be represented in a compact form of the algebraic equations as follows:

$$\begin{bmatrix} i(t) \\ 0 \\ i_m \\ 0 \end{bmatrix} = y_{eq}X(t) - b_{eq} + \begin{bmatrix} 0 \\ X(t)^T F_{eq(1\sim i)} X(t) \\ 0 \\ X(t)^T F_{eq(i+1\sim j)} X(t) \end{bmatrix} \tag{3.3.22}$$

Where: $i(t) = \begin{bmatrix} i_1(t) & i_2(t) & i_3(t) & i_4(t) & i_5(t) \end{bmatrix}^T$,

$X(t) = \begin{bmatrix} v(t) & y(t) & z(t) & v_m & y_m & z_m \end{bmatrix}^T$,

$v(t) = \begin{bmatrix} v_1(t) & v_2(t) & v_3(t) & v_4(t) & v_5(t) \end{bmatrix}$,

$y(t) = \begin{bmatrix} e(t) & i_{m1}(t) & i_{m2}(t) & i_H(t) & i_L(t) & i_{S1}(t) & i_{S2}(t) & i_S(t) & \lambda(t) \end{bmatrix}$,

$z(t) = \begin{bmatrix} z_1(t) & z_2(t) & z_3(t) \end{bmatrix}$.

Note that y_{eq} and F_{eq} are *n-by-n* matrices, b_{eq} is an *n*-by-1 vector of historical data at *t-h*, and *j* is the number of nonlinear terms.

All components of passive devices and electronics are written in the same form, which is referred to an algebraic companion form (ACF) as the single-phase saturable transformer, and are merged by a computer algorithm. For this purpose, it is noted that each component is connected to specific nodes of the push-pull resonant converter. The connectivity of each component is defined in terms of the order of the corresponding states. Figure 3.12 shows the node numbers on specific nodes. Since the merging process of all components is the same as one another, the merging process of the single-phase saturable transformer is only presented. Table IV provides the connectivity pointers of the single-phase saturable transformer.

Table 3.4: Connective pointers of the single-phase saturable transformer

Connective pointers of the single-phase transformer	
t	t_m
4, 5, 6, 7, 8, 9, 10, 11, 12, 13, 14, 15, 16, 17, 18, 19, 20	39, 40, 41, 42, 43, 44, 45, 46, 47, 48, 49, 50, 51, 52, 53, 54, 55

The merging of the single-phase saturable transformer into the push-pull, resonant converter is achieved by writing Kirchhoff's current law at each internal node of the push-pull resonant converter, substituting the appropriate equations. This process is achieved with the algorithm below:

DO WHILE ($i <$ *the number of rows*)

$i1 = 1 - \phi$ *transformer pointer*$[i]$

$b_{eq.pp}[i1] = b_{eq}[i]$

DO WHILE ($i <$ *the number of columns*)

$ji = 1 - \phi$ *transformer pointer*$[i]$

$y_{eq,pp}[i1][j1] = y_{eq}[i][j]$

$F_{eq,pp}[i1][j1] = F_{eq}[i][j]$

END DO

END DO

where i = 1,2,…,the number of rows of each matrix,

j = 1,2,…,the number of columns of each matrix.

Note that the 1-ϕ transformer pointer is the order of the connective pointers in Table IV, and $X_{eq.pp}$ denotes the matrix or vector of the push-pull converter. After all components are merged by the computer algorithm, the end result is an algebraic companion form (ACF) of the push-pull resonant converter, given by the following equation:

$$\begin{bmatrix} i(t) \\ 0 \\ i_m \\ 0 \end{bmatrix} = y_{eq,pp} X(t) - b_{eq,pp} + \begin{bmatrix} 0 \\ X(t)^T F_{eq(1\sim i),pp} X(t) \\ 0 \\ X(t)^T F_{eq(i+1\sim j),pp} X(t) \end{bmatrix} \qquad (3.3.23)$$

where $y_{eq,pp}$ and $F_{eq,pp}$ are *70-by-70* matrices and $b_{eq,pp}$ is a *70*-vector, which are automatically built with the computer algorithm above.

3.3.4 Application of Newton's Method

As soon as all components (devices) in a system to be analyzed are modeled, they have to be merged to form an entire system by using a computer algorithm, as in the case

of the push-pull resonant converter, shown in Figure 3.12. Then the system currents can be eliminated and the state variables only remain in the ACF of the system as follows:

$$\begin{bmatrix} 0 \\ 0 \\ 0 \\ 0 \end{bmatrix} = y_{eq} X(t) - b_{eq} + \begin{bmatrix} X(t)^T F_{eq1} X(t) \\ X(t)^T F_{eq2} X(t) \\ \vdots \\ X(t)^T F_{eqn} X(t) \end{bmatrix} \tag{3.3.24}$$

where $X(t)$ and b_{eq} are n-vectors, and y_{eq} and F_{eq} are n-*by*-n matrices, while the total number of state variables is n.

Here, Newton's method is applied for iterative calculation of the quadratized model and the solution is given by the following form:

$$X^{\nu+1}(t) = X^{\nu}(t) - J^{-1} \cdot \left(y_{eq} X^{\nu}(t) - b_{eq} + \begin{bmatrix} X^{\nu}(t)^T F_{eq1} X^{\nu}(t) \\ X^{\nu}(t)^T F_{eq2} X^{\nu}(t) \\ \vdots \\ X^{\nu}(t)^T F_{eqn} X^{\nu}(t) \end{bmatrix} \right) \tag{3.3.25}$$

where: $J = y_{eq} + \begin{bmatrix} x^{\nu}(t)^T \left(F_{eq1} + F_{eq1}^T \right) \\ x^{\nu}(t)^T \left(F_{eq2} + F_{eq2}^T \right) \\ \vdots \\ x^{\nu}(t)^T \left(F_{eq2} + F_{eq2}^T \right) \end{bmatrix}$.

Newton's method has demonstrated that the convergence characteristics of the quadratized equations are outstanding, compared to other methods [27]. For example, the simulations of a DC-DC system (in the next subsection) using the push-pull resonant converter are converged to the total error of 10^{-13} before four iterations at each time-step.

3.4 Demonstrative Example

In this subsection, an example system is presented to demonstrate the superior properties of the QMQI method. The demonstrative example is a DC system using the push-pull DC-DC converter, shown in Figure 3.14. The push-pull DC-DC converter is interconnecting the 24V-ideal source and a passive load (R_L) of 200-ohms. The ratio of the single-phase saturable-transformer is 24V/200V, and the push-pull, resonant converter is operated in an open-loop control algorithm with a modulation index of 0.48. Note that the switching frequency is 65-kH.

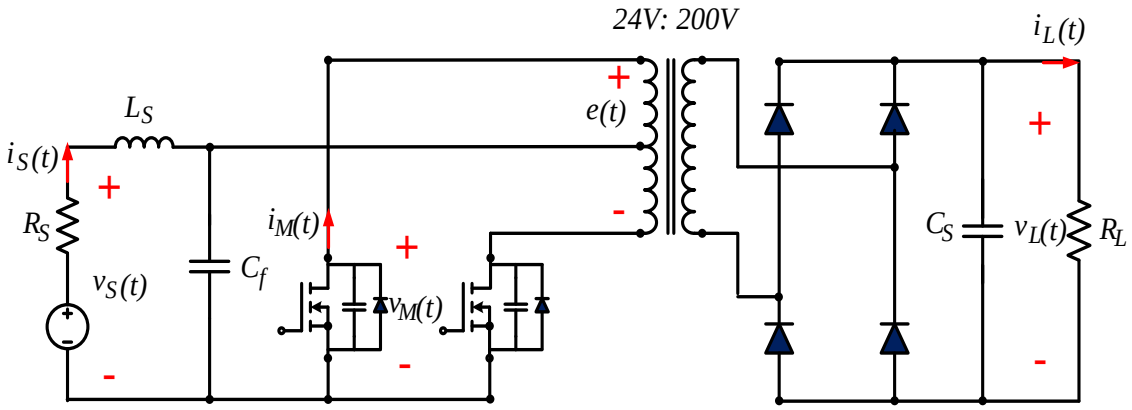

Figure 3.14: A Push-pull resonant converter interconnecting an ideal source and a passive load.

Figure 3.15 represents the (A) source voltage and (B) current; (C) load voltage and (D) current; the (E) induced EMF of the saturable transformer; and the (F) voltage and (G) current of the MOSFET. Figure 3.16 shows the case when the push-pull resonant converter fails in the operation of zero voltage switching (ZVC). Graphs (A) and (B) are the voltage and current of a MOSFET on an operation of ZVS, while graphs (C) and (D) are the voltage and current of a MOSFET at nonzero voltage switching. Note that the

modulation index of 0.47 and faster resonant frequency is used to present graphs (C) and (D).

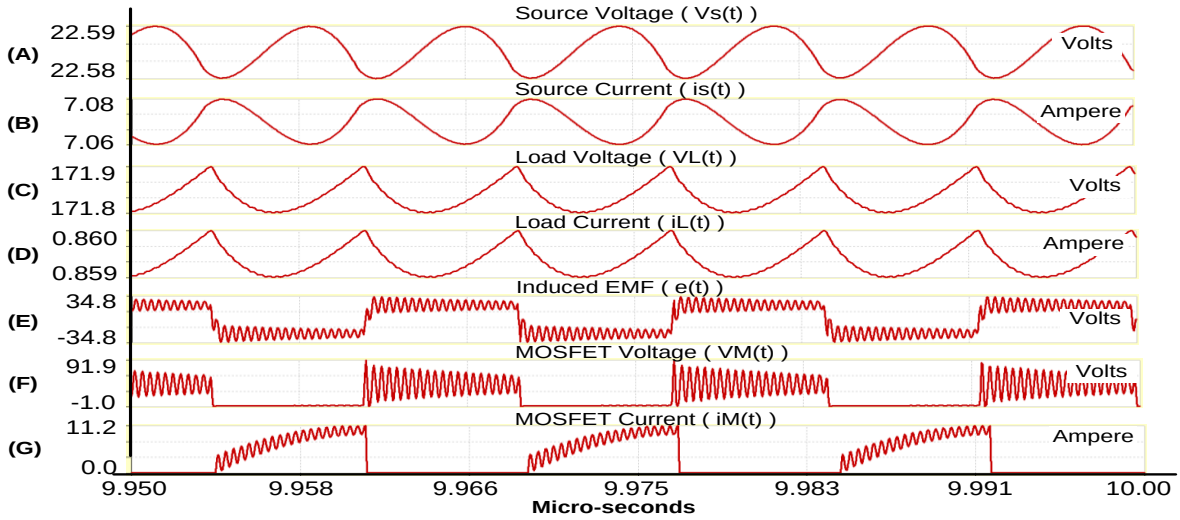

Figure 3.15: Simulation results of the DC system using the push-pull converter.

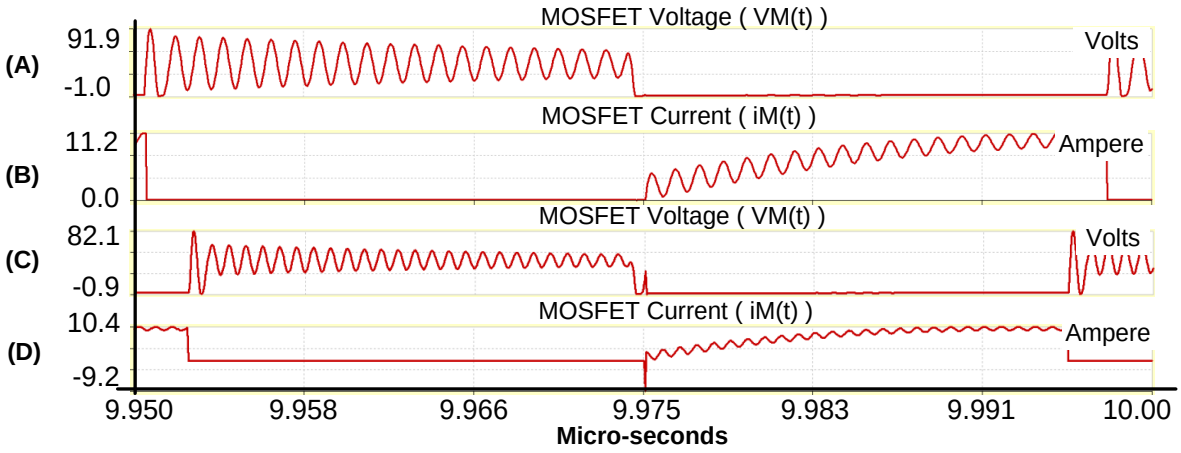

Figure 3.16: Voltage and current of a MOSFET: (A) and (B) in ZVC and (C) and (D) non-ZVC.

3.5 Summary

This section presents a new approach, a combination method of model quadratization and quadratic integration. The quadratic-integration method is not only totally free of numerical oscillations in time-domain analyses, but also increases the simulation accuracy and robustness, compared to popularly used methods in previous power system analyses. Also, modal quadratization allows nonlinearities to be modeled in a nonlinear concept without the approximation of models (such as linearization of nonlinear equations) accompanied with Newton's method. The QMQI method is especially suitable to model and analyses mixed-power systems of nonlinearities and switching subsystems, since the method permits more accurate and reliable analyses than previous modeling methods in simple modeling process. It is important to note that mixed-power systems with power electronics and nonlinearities have barely been modeled due to the difficulty in controlling switching systems. However, the QMQI method is used for these cases with simplicity and great precision.

CHAPTER 4

AVERAGING MODELS OF CONVERTERS

4.1 Introduction

The modeling methodology for power systems with nonlinearities and switching systems was presented in Chapter 3. In this chapter, a method for modeling converters, which is referred to the averaging method, is presented. The averaging method is based on the steady-state analysis and the equivalent relationship between input and output (two-port network analysis). In these averaging concepts, the voltage and current ripples are averaged, and the harmonics at both the AC-side and the DC-side of the converters are ignored. Note that the dynamic behaviors, such as switching operation and transient phenomena, are not in consideration for the averaged converter models. However, this method has the distinct advantage of quantitative analysis, such as power transfer capability, total operational losses, and optimal kV-level studies of networks.

Here, three converters are developed: a phase-controlled, six-pulse converter, a phase-controlled cycloconverter, and a PWM converter.

4.2 Averaging Model of a Six-Pulse Converter

Here, a three-phase, six-pulse converter is modeled in the averaging modeling concept. The averaging method could be used for two modes of a rectifier and an inverter. Since the averaging model of the inverter is almost the same as that of the rectifier, the averaging model of the rectifier is only presented in this subsection. The averaging model of a three-phase, six-pulse rectifier consists of the simplified limiting current

reactors (*-jB*) and simplified internal admittances (*G*). The converter is controlled based on an equidistant control algorithm using firing angle (α) to control the DC-voltage level. Note that the inverter uses extinction angle (γ) to control the firing angle. Figure 4.1 shows the equivalent circuit of the standard six-pulse converter.

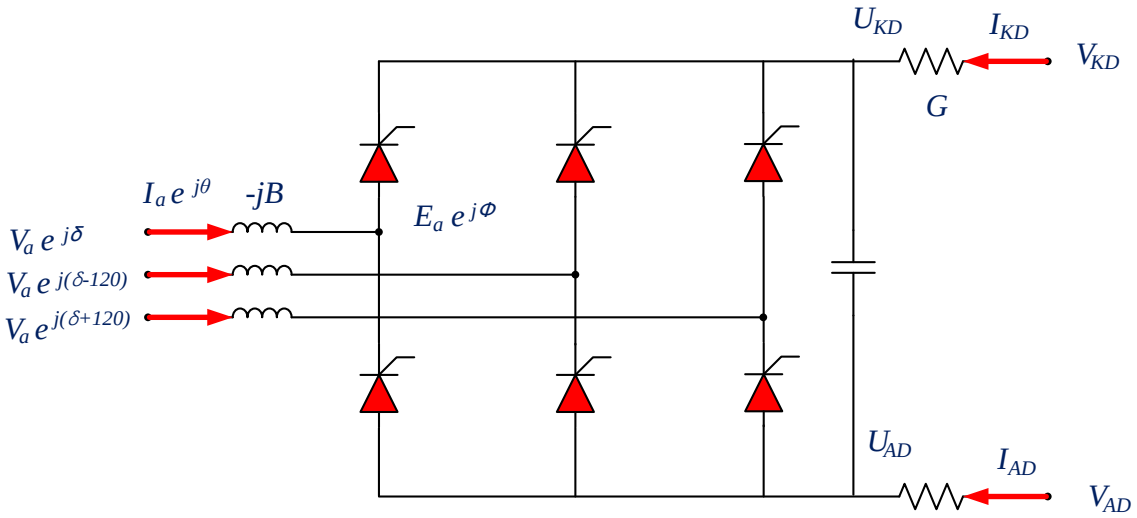

Figure 4.1: An averaging model of a three-phase, six-pulse converter.

For the DC-voltage control-mode, the six-pulse converter equations are denoted as state equations. The model equations are as follows:

$$\tilde{I}_a = -jB(\tilde{V}_a - \tilde{E}_a) \quad (4.2.1)$$

$$\tilde{I}_b = -jB(\tilde{V}_b - \tilde{E}_b) \quad (4.2.2)$$

$$\tilde{I}_c = -jB(\tilde{V}_c - \tilde{E}_c) \quad (4.2.3)$$

$$I_{KD} = G(V_{KD} - U_{KD}) \quad (4.2.4)$$

$$I_{AD} = G(V_{AD} - U_{AD}) \quad (4.2.5)$$

$$0 = I_{KD} + I_{AD} = G(V_{KD} - U_{KD}) + G(V_{AD} - U_{AD}) \quad (4.2.6)$$

$$0 = V_{KD} - V_{AD} - V_{DC.ref} \quad (4.2.7)$$

$$0 = (V_{kd} - V_{Ad}) \cdot I_{Ad} + \frac{2 \cdot I_{Ad}^2}{G} - \mathrm{Re}\left\{V_a I_a^* + V_b I_b^* + V_c I_c^*\right\} \tag{4.2.8}$$

$$0 = 3\left|\tilde{V}_a\right|\left|\tilde{I}_a\right|\sin\varphi - \mathrm{Im}\{\tilde{V}_a \tilde{I}_a^* + \tilde{V}_b \tilde{I}_b^* + \tilde{V}_c \tilde{I}_c^*\} \tag{4.2.9}$$

$$0 = V_{do} - \frac{3\sqrt{6}}{\pi}\left|\tilde{V}_a\right| \tag{4.2.10}$$

$$0 = u_{KD} - u_{AD} - V_{do} \cdot \cos(\varphi) \tag{4.2.11}$$

$$0 = \cos(\varphi) - 0.5\cos(\alpha + \beta) - 0.5\cos(\alpha) \tag{4.2.12}$$

$$0 = \left|\tilde{V}_a\right|\cos(\varphi) - \left|\tilde{V}_a\right|\cos(\alpha) + \frac{1}{\sqrt{6}B} I_{AD} \tag{4.2.13}$$

$$0 \le \varphi \le \pi \tag{4.2.14}$$

$$0 \le \alpha \le \pi \tag{4.2.15}$$

$$0 \le \alpha + \beta \le \pi \tag{4.2.16}$$

$$-1 \le \cos(\varphi) \le 1 \tag{4.2.17}$$

$$-1 \le \cos(\alpha) \le 1 \tag{4.2.18}$$

$$-1 \le \cos(\alpha + \beta) \le 1 \tag{4.2.19}$$

where V_{do} is a no-load DC-voltage, α and β are the firing angle and the commutation angle, respectively, and φ is the control angle, which is related to the firing angle and commutation angle.

Equations (4.2.1) to (4.2.5) are external state-equations and Equations (4.2.6) to (4.2.13) are internal state equations, while Equations (4.2.14) to (4.2.19) are constraints of the control angle, the firing angle, and the commutation angle.

The model equations derived from the six-pulse converter can be represented as phasor representations and quadratized equations, using model quadratization to convert

nonlinear equations into linear and quadratic equations. The averaging model of the six-pulse rectifier can be rewritten as follows:

$$I_{ar} = BV_{ai} - BE_{ai} \tag{4.2.20}$$

$$I_{ai} = -BV_{ar} + BE_{ar} \tag{4.2.21}$$

$$I_{br} = BV_{bi} + \left(\sqrt{3}/2\right)B \cdot E_{ar} + 0.5 \cdot B \cdot E_{ai} \tag{4.2.22}$$

$$I_{bi} = -BV_{br} - 0.5 \cdot B \cdot E_{ar} + \left(\sqrt{3}/2\right)B \cdot E_{ai} \tag{4.2.23}$$

$$I_{cr} = BV_{ci} - \left(\sqrt{3}/2\right)B \cdot E_{ar} + 0.5 \cdot B \cdot E_{ai} \tag{4.2.24}$$

$$I_{ci} = -BV_{cr} - 0.5 \cdot B \cdot E_{ar} - \left(\sqrt{3}/2\right)B \cdot E_{ai} \tag{4.2.25}$$

$$I_{KD.r} = GV_{KD.r} - Gu_{KD.r} \tag{4.2.26}$$

$$I_{KD.i} = 1.0V_{KD.i} \tag{4.2.27}$$

$$I_{AD.r} = GV_{AD.r} - Gu_{AD.r} \tag{4.2.28}$$

$$I_{AD.i} = 1.0V_{AD.i} \tag{4.2.29}$$

$$0 = GV_{KD.r} - Gu_{KD.r} + GV_{AD.r} - Gu_{AD.r} \tag{4.2.30}$$

$$0 = V_{KD.r} - V_{AD.r} - V_{ref} \tag{4.2.31}$$

$$0 = \cos(\varphi) - 0.5\cos(\alpha + \beta) - 0.5\cos(\alpha) \tag{4.2.32}$$

$$0 = V_{do} - \frac{3\sqrt{6}}{\pi} x_8 \tag{4.2.33}$$

$$0 = x_1 - V_{AD.r} + U_{AD.r} \tag{4.2.34}$$

$$0 = x_2 - V_{ai} + E_{ai} \tag{4.2.35}$$

$$0 = x_3 + V_{ar} - E_{ar} \tag{4.2.36}$$

$$0 = x_4 - V_{bi} - \left(\sqrt{3}/2\right)E_{ar} - 0.5E_{ai} \tag{4.2.37}$$

$$0 = x_5 + V_{br} + 0.5E_{ar} - \left(\sqrt{3}/2\right)E_{ai} \tag{4.2.38}$$

$$0 = x_6 - V_{ci} + \left(\sqrt{3}/2\right)E_{ar} - 0.5E_{ai} \tag{4.2.39}$$

$$0 = x_7 + V_{cr} + 0.5E_{ar} + \left(\sqrt{3}/2\right)E_{ai} \tag{4.2.40}$$

$$0 = G \cdot x_1(V_{kd.r} - V_{Ad.r}) + 2G \cdot x_1^2 - B\left(x_2V_{ar} + x_3V_{ai} + x_4V_{br} + x_5V_{bi} + x_6V_{cr} + x_7V_{ci}\right) \tag{4.2.41}$$

$$0 = 3B \cdot x_{10} \cdot x_{11} - B \cdot x_2V_{ai} + B \cdot x_3V_{ar} - B \cdot x_4V_{bi} + B \cdot x_5V_{br} - B \cdot x_6V_{ci} + B \cdot x_7V_{cr} \tag{4.2.42}$$

$$0 = x_8\cos(\varphi) - x_8\cos(\alpha) + \frac{G}{\sqrt{6}B} \cdot x_1 \tag{4.2.43}$$

$$0 = u_{\mathrm{KD.r}} - u_{\mathrm{AD.r}} - V_{do}\cos(\varphi) \tag{4.2.44}$$

$$0 = x_8^2 - V_{ar}^2 - V_{ai}^2 \tag{4.2.45}$$

$$0 = x_9^2 - x_2^2 - x_3^2 \tag{4.2.46}$$

$$0 = x_{10} - x_8 \cdot x_9 \tag{4.2.47}$$

$$0 = -1.0 + \cos(\varphi)^2 + x_{11}^2 \tag{4.2.48}$$

$$0 = -1.0 + \cos(\alpha)^2 + x_{12}^2 \tag{4.2.49}$$

$$0 = -1.0 + \cos(\alpha + \beta)^2 + x_{13}^2 \tag{4.2.50}$$

$$0 = x_{11} - x_{14}^2 \tag{4.2.51}$$

$$0 = x_{12} - x_{15}^2 \tag{4.2.52}$$

$$0 = x_{13} - x_{16}^2 \tag{4.2.53}$$

$$0 = x_8 - x_{17}^2 \tag{4.2.54}$$

$$0 = x_9 - x_{18}^2 \tag{4.2.55}$$

As shown in the quadratized equations above, the high-order equations are converted into linear and quadratic equations, introducing additional state variables. Also, the angle

constraints are represented in quadratic equations. The quadratized model can be denoted in algebraic companion form, in which the components (or devices) are written in the same matrix form so that all devices in a system to be analyzed can be merged. The algebraic companion form of the three-phase, six-pulse converter can be reformulated as follows:

$$\begin{bmatrix} I \\ 0 \end{bmatrix} = y_{eq} \begin{bmatrix} V \\ Y \\ X \end{bmatrix} - b_{eq} + \begin{bmatrix} 0 \\ \cdots \\ 0 \\ X^T F_{eq22} X \\ X^T F_{eq22} X \\ \cdots \\ X^T F_{eq31} X \end{bmatrix} \tag{4.2.56}$$

where: $X = [V \;\; Y \;\; X_1]^T$

$V = [V_{ar} \;\; V_{ai} \;\; V_{br} \;\; V_{bi} \;\; V_{cr} \;\; V_{ci} \;\; V_{KD.r} \;\; V_{KD.i} \;\; V_{AD.r} \;\; V_{AD.i}]$,

$Y = [E_r \;\; E_i \;\; u_{KD.r} \;\; u_{AD.r} \;\; \cos\varphi \;\; \cos(\alpha+\beta) \;\; \cos\alpha \;\; V_{do}]$, and

$X_1 = [x_1 \;\; x_2 \;\; x_3 \;\; x_4 \;\; x_5 \;\; x_6 \;\; x_7 \;\; x_8 \;\; x_9 \;\; x_{10} \;\; x_{11} \;\; x_{12} \;\; x_{13} \;\; x_{14} \;\; x_{15} \;\; x_{16} \;\; x_{17} \;\; x_{18}]$.

$I = [I_{ar} \;\; I_{ai} \;\; I_{br} \;\; I_{bi} \;\; I_{cr} \;\; I_{ci} \;\; I_{KD.r} \;\; I_{KD.i} \;\; I_{AD.r} \;\; I_{AD.i}]^T$

4.3 Averaging Model of a Phase-Controlled Cycloconverter

A three-phase, six-pulse cycloconverter is modeled in the averaging modeling concept. The averaging method consists of three-phase isolation-transformers and the simplified reactors (*-jB*) and admittances (*G*), as shown in Figure 4.2. The converter is modeled under certain assumptions: the converter is working in a circulating current-free mode of operation, the control algorithm of the converter is a cosine-wave-crossing

method, and the transformers are a wye-wye winding connection with the voltage ratio of one.

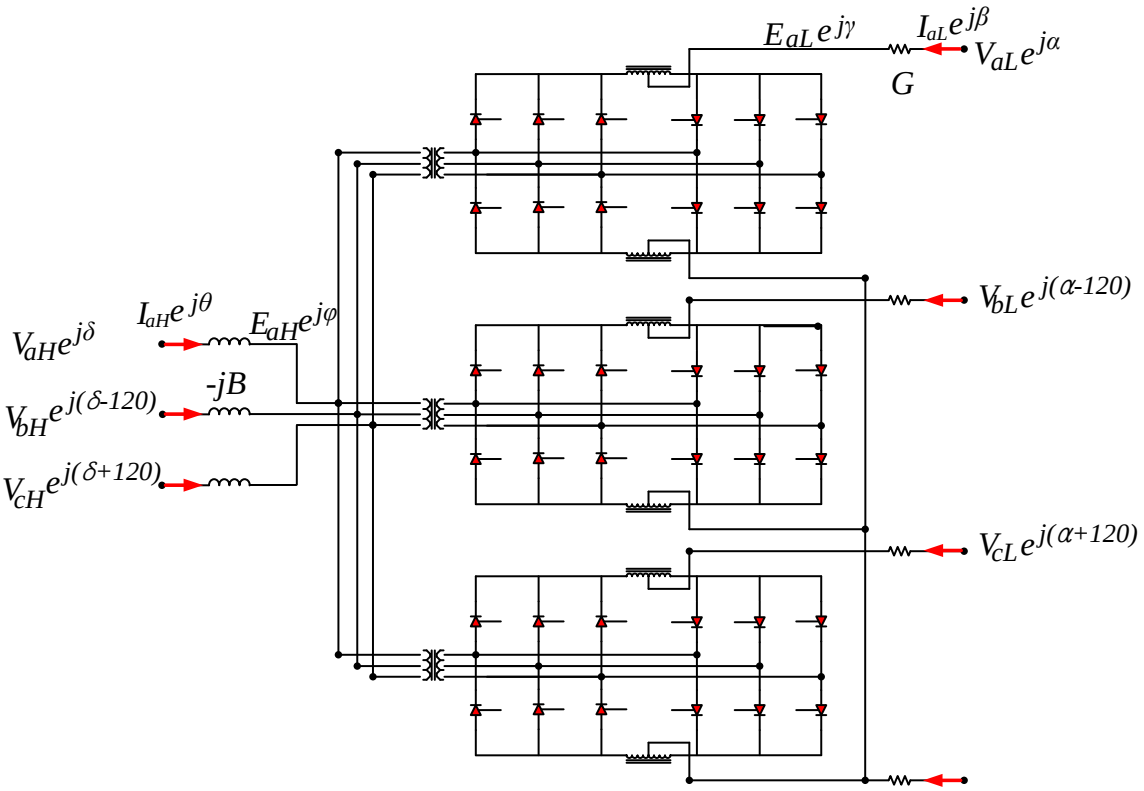

Figure 4.2: An averaging model of a three-phase, six-pulse cycloconverter.

In the cycloconverter model, the averaging input-currents at high frequency cannot be separately controlled and depend on the displacement factor at low frequency and the modulation index which is the magnitude ratio between the input voltages and output voltages. Also, the averaging values have many variations according to the control algorithm and the physical structure itself. Thus, it is difficult to model cycloconverters with fixed parameters and the parameters in the cycloconverter must be selected in specific conditions. For this purpose, the averaging model of the cycloconverter uses pre-calculated values to compute the relationship between the input currents and the output

currents of the cycloconverter [28]. The fundamental components of the input currents consist of an in-phase current (I_p) and a lagging quadrature current (I_q) as follows:

$$I_1 = I_p + jI_q = \sqrt{I_p^2 + I_q^2}\cos\phi_i \tag{4.3.1}$$

where $cos\phi_i$ is the power factor of the input current.

$$I_p = q \cdot s \frac{r\sqrt{3}}{2\pi} I_o \cos\phi_o \tag{4.3.2}$$

$$I_q = q \cdot s \frac{2\sqrt{3}}{\pi^2} I_o \sum_{n=0}^{n=\infty} \frac{-a_{1_{2n}} \cos 2n\phi_o}{(2n-1)(2n+1)} \tag{4.3.3}$$

Where: q is the number of output phase ($q=3$);

s is the number of 3-pulse groups connected in series with one another ($s=2$);

I_o is the RMS current of each output phase ; and

$\cos\phi_o$ is the power factor of the LF(low frequency)-AC side.

Here, the modulation index (r) is calculated and then the coefficients (a_{10}, a_{12}, a_{14}, etc.) of the fundamental components are selected to find the relationship between the input-currents and output-currents as follows.

First, the modulation index can be computed using the rated voltage of the cycloconverter and the reference output-voltage as follows:

$$r = \frac{V_{ref}}{V_{rate}\cos 30^o} \tag{4.3.4}$$

where: V_{ref} is the reference output voltage (Line-to-Line) and V_{rate} is the rating voltage at the input side of the cycloconverter. Note that the modulation index is from 0.1 to 1.

The next is to select the coefficients of the fundamental component in Table 4.1. The coefficients in Table 4.1 are calculated mathematically in [28].

Table 4.1: The coefficients of the fundamental component for input currents

Modulation Index (r)	Coefficients of fundament component								
	$a1_0$	$a1_2$	$a1_4$	$a1_6$	$a1_8$	$a1_{10}$	$a1_{12}$	$a1_{14}$	$a1_{16}$
1.0	0.637	0.424	-0.085	0.036	-0.020	0.013	-0.009	0.007	-0.005
0.9	0.746	0.277	-0.027	0.005	-0.001	0.000	0.000	0.000	0.000
0.8	0.813	0.198	-0.012	0.002	0.000	0.000	0.000	0.000	0.000
0.7	0.863	0.142	-0.006	0.000	0.000	0.000	0.000	0.000	0.000
0.6	0.903	0.100	-0.003	0.000	0.000	0.000	0.000	0.000	0.000
0.5	0.934	0.067	-0.001	0.000	0.000	0.000	0.000	0.000	0.000
0.4	0.959	0.042	0.000	0.000	0.000	0.000	0.000	0.000	0.000
0.3	0.977	0.023	0.000	0.000	0.000	0.000	0.000	0.000	0.000
0.2	0.990	0.010	0.000	0.000	0.000	0.000	0.000	0.000	0.000
0.1	0.997	0.003	0.000	0.000	0.000	0.000	0.000	0.000	0.000

Using Equations (4.3.2) and (4.3.3) and the selected coefficients in Table 4.1, the three-phase, six-pulse cycloconverter are written as follows:

$$I_{aH} = -jB\left(\tilde{\tilde{V}}_{aH} - \tilde{\tilde{E}}_{aH}\right) \tag{4.3.5}$$

$$I_{bH} = -jB\left(\tilde{\tilde{V}}_{bH} - \tilde{\tilde{E}}_{bH}\right) \tag{4.3.6}$$

$$I_{cH} = -jB\left(\tilde{\tilde{V}}_{cH} - \tilde{\tilde{E}}_{cH}\right) \tag{4.3.7}$$

$$I_{aL} = G\left(\tilde{\tilde{V}}_{aL} - \tilde{\tilde{E}}_{aL}\right) \tag{4.3.8}$$

$$I_{bL} = G\left(\tilde{\tilde{V}}_{bL} - \tilde{\tilde{E}}_{bL}\right) \tag{4.3.9}$$

$$I_{cL} = G\left(\tilde{\tilde{V}}_{cL} - \tilde{\tilde{E}}_{cL}\right) \tag{4.3.10}$$

$$0 = \tilde{\tilde{V}}_{aL} - \tilde{\tilde{V}}_{ref} \tag{4.3.11}$$

$$0 = \mathrm{Re}\left\{\tilde{\tilde{V}}_{abcH}\,\tilde{\tilde{I}}^{*}_{abcH}\right\} + \mathrm{Re}\left\{\tilde{\tilde{E}}_{abcL}\,\tilde{\tilde{I}}^{*}_{abcL}\right\} \tag{4.3.12}$$

$$0 = \mathrm{Im}\left\{\tilde{\tilde{V}}_{abcH}\,\tilde{\tilde{I}}^{*}_{abcH}\right\} - 3\left|\tilde{\tilde{V}}_{a}\right|\left|I_1\right| y_4 \tag{4.3.13}$$

$$0 = I_p - \frac{3\sqrt{3}}{\pi}\left|I_{aL}\right| \cdot r \cdot y_1 \tag{4.3.14}$$

$$0 = I_q - \frac{12\sqrt{3}}{\pi^2}\left|I_{aL}\right|\left\{ a_{1_0} - \frac{a_{1_2}}{3} y_2 - \frac{a_{1_4}}{15} y_3 \right\} \tag{4.3.15}$$

$$0 = P_L + \mathrm{Re}\left\{ \tilde{E}_{abcL} \tilde{I}^*_{abcL} \right\} \tag{4.3.16}$$

$$0 = Q_L + \mathrm{Im}\left\{ \tilde{E}_{abcL} \tilde{I}^*_{abcL} \right\} \tag{4.3.17}$$

$$0 = \sqrt{P_L^2 + Q_L^2} \cdot y_1 - P_L \tag{4.3.18}$$

$$0 = y_2 - 2y_1^2 + 1 \tag{4.3.19}$$

$$0 = y_3 - 2y_2^2 + 1 \tag{4.3.20}$$

$$0 = |I_1| y_4 - I_q \tag{4.3.21}$$

$$0 = 3\left|\tilde{V}_{aH}\right| \cdot r - \tilde{V}_{ref} \tag{4.3.22}$$

$$-1 \le y_1 \le 1 \tag{4.3.23}$$

$$-1 \le y_2 \le 1 \tag{4.3.24}$$

$$-1 \le y_3 \le 1 \tag{4.3.25}$$

$$0 \le y_4 \le 1 \tag{4.3.26}$$

$$0 \le r \le 1 \tag{4.3.27}$$

Where: y_1, y_2, y_3, and y_4 represent $\cos\phi_o$, $\cos 2\phi_o$, $\cos 4\phi_o$, and $\sin\phi_i$ respectively, $\tilde{V}_{ref}$ is the reference voltage at low-frequency, and P_L and Q_L are real- and reactive-power at the low-frequency side. Equations (4.3.5) to (4.3.10) are external state equations and Equations (4.3.11) to (4.3.22) are internal state equations, while Equations (4.3.23) to (4.3.27) are constraints of the displacement factors at both sides.

The model equations derived from the three-phase, six-pulse cycloconverter can be represented as phasor representations and quadratized equations using model quadratization to convert nonlinear equations into linear and quadratic equations. The averaging model of the cycloconverter can be rewritten as follows:

$$I_{aHr} = BV_{aHi} - BE_{Hi} \tag{4.3.28}$$

$$I_{aHi} = -BV_{aHr} + BE_{Hr} \tag{4.3.29}$$

$$I_{bHr} = BV_{bHi} + \left(\sqrt{3}/2\right)B \cdot E_{Hr} + 0.5BE_{Hi} \tag{4.3.30}$$

$$I_{bHi} = -BV_{bHr} - 0.5B \cdot E_{Hr} + \left(\sqrt{3}/2\right)BE_{Hi} \tag{4.3.31}$$

$$I_{cHr} = BV_{cHi} - \left(\sqrt{3}/2\right)B \cdot E_{Hr} + 0.5BE_{Hi} \tag{4.3.32}$$

$$I_{cHi} = -BV_{cHr} - 0.5B \cdot E_{Hr} - \left(\sqrt{3}/2\right)BE_{Hi} \tag{4.3.33}$$

$$I_{aLr} = GV_{aLr} - GE_{Lr} \tag{4.3.34}$$

$$I_{aLi} = GV_{aLi} - GE_{Li} \tag{4.3.35}$$

$$I_{bLr} = GV_{bLr} + 0.5G \cdot E_{Lr} - \left(\sqrt{3}/2\right)G \cdot E_{Li} \tag{4.3.36}$$

$$I_{bLi} = GV_{bLi} + \left(\sqrt{3}/2\right)G \cdot E_{Lr} + 0.5G \cdot E_{Li} \tag{4.3.37}$$

$$I_{cLr} = GV_{cLr} + 0.5G \cdot E_{Lr} + \left(\sqrt{3}/2\right)G \cdot E_{Li} \tag{4.3.38}$$

$$I_{cLi} = GV_{cLi} - \left(\sqrt{3}/2\right)G \cdot E_{Lr} + 0.5G \cdot E_{Li} \tag{4.3.39}$$

$$0 = V_{aLr} - V_{ref \cdot r} \tag{4.3.40}$$

$$0 = V_{aLi} - V_{ref \cdot i} \tag{4.3.41}$$

$$0 = x_1 - V_{aHi} + E_{Hi} \tag{4.3.42}$$

$$0 = x_2 + V_{aHr} - E_{Hr} \tag{4.3.43}$$

$$0 = x_3 - V_{bHi} - \left(\sqrt{3}/2\right)E_{Hr} - 0.5E_{Hi} \tag{4.3.44}$$

$$0 = x_4 + V_{bHr} + 0.5E_{Hr} - \left(\sqrt{3}/2\right)E_{Hi} \tag{4.3.45}$$

$$0 = x_5 - V_{cHi} + \left(\sqrt{3}/2\right)E_{Hr} - 0.5E_{Hi} \tag{4.3.46}$$

$$0 = x_6 + V_{cHr} + 0.5E_{Hr} + \left(\sqrt{3}/2\right)E_{Hi} \tag{4.3.47}$$

$$0 = x_7 + 0.5E_{Lr} - \left(\sqrt{3}/2\right)E_{Li} \tag{4.3.48}$$

$$0 = x_8 + \left(\sqrt{3}/2\right)E_{Lr} + 0.5E_{Li} \tag{4.3.49}$$

$$0 = x_9 + 0.5E_{Lr} + \left(\sqrt{3}/2\right)E_{Li} \tag{4.3.50}$$

$$0 = x_{10} - \left(\sqrt{3}/2\right)E_{Lr} + 0.5E_{Li} \tag{4.3.51}$$

$$0 = x_{11} - V_{aLr} + E_{Lr} \tag{4.3.52}$$

$$0 = x_{12} - V_{aLi} + E_{Li} \tag{4.3.53}$$

$$0 = x_{13} - V_{bLr} + x_7 \tag{4.3.54}$$

$$0 = x_{14} - V_{bLi} + x_8 \tag{4.3.55}$$

$$0 = x_{15} - V_{cLr} + x_9 \tag{4.3.56}$$

$$0 = x_{16} - V_{cLi} + x_{10} \tag{4.3.57}$$

$$0 = x_{17}^2 - V_{aHr}^2 - V_{aHi}^2 \tag{4.3.58}$$

$$0 = x_{18}^2 - I_p^2 - I_q^2 \tag{4.3.59}$$

$$0 = 3x_{19}I_p - P_L \tag{4.3.60}$$

$$0 = x_{20}^2 - x_{11}^2 - x_{12}^2 \tag{4.3.61}$$

$$\begin{aligned} 0 = {} & BV_{aHr}x_1 + BV_{aHi}x_2 + BV_{bHr}x_3 + BV_{bHi}x_4 + BV_{cHr}x_5 + BV_{cHi}x_6 + \\ & - GE_{Lr}x_{11} - GE_{Li}x_{12} - Gx_7x_{13} - Gx_8x_{14} - Gx_9x_{15} - Gx_{10}x_{16} \end{aligned} \tag{4.3.62}$$

$$0 = -BV_{aHr}x_2 + BV_{aHi}x_1 - BV_{bHr}x_4 + BV_{bHi}x_3 - BV_{cHr}x_6 + BV_{cHi}x_5 - 3x_{19}y_4 \tag{4.3.63}$$

$$0 = I_p - \frac{3\sqrt{3}r}{\pi}G \cdot x_{20}y_1 \tag{4.3.64}$$

$$0 = I_q - \frac{12\sqrt{3}\cdot a_{1_0}}{\pi^2} G\cdot x_{20} + \frac{12\sqrt{3}\cdot a_{1_2}}{3\pi^2} G\cdot x_{20}y_2 + \frac{12\sqrt{3}\cdot a_{1_4}}{15\pi^2} G\cdot x_{20}y_3 \tag{4.3.65}$$

$$0 = P_L - GE_{Lr}x_{11} - GE_{Li}x_{12} - Gx_7x_{13} - Gx_8x_{14} - Gx_9x_{15} - Gx_{10}x_{16} \tag{4.3.66}$$

$$0 = Q_L + GE_{Lr}x_{12} - GE_{Li}x_{11} + Gx_7x_{14} - Gx_8x_{13} + Gx_9x_{16} - Gx_{10}x_{15} \tag{4.3.67}$$

$$0 = x_{21}^2 - P_L^2 - Q_L^2 \tag{4.3.68}$$

$$0 = x_{21}y_1 - P_L \tag{4.3.69}$$

$$0 = y_2 - 2y_1^2 + 1 \tag{4.3.70}$$

$$0 = y_3 - 2y_2^2 + 1 \tag{4.3.71}$$

$$0 = x_{18}y_4 - I_q \tag{4.3.72}$$

$$0 = y_1^2 + x_{22}^2 - 1 \tag{4.3.73}$$

$$0 = y_2^2 + x_{23}^2 - 1 \tag{4.3.74}$$

$$0 = y_3^2 + x_{24}^2 - 1 \tag{4.3.75}$$

$$0 = y_4^2 + x_{25}^2 - 1 \tag{4.3.76}$$

$$0 = y_4 - x_{26}^2 \tag{4.3.77}$$

$$0 = x_{17} - x_{27}^2 \tag{4.3.78}$$

$$0 = x_{18} - x_{28}^2 \tag{4.3.79}$$

$$0 = x_{20} - x_{29}^2 \tag{4.3.80}$$

$$0 = x_{21} - x_{30}^2 \tag{4.3.81}$$

$$0 = 3x_{17}\cdot r - \tilde{V}_{ref} \tag{4.3.82}$$

$$0 = r^2 + x_{31}^2 - 1 \tag{4.3.83}$$

$$0 = r - x_{32}^2 \tag{4.3.84}$$

$$0 = x_{33} \tag{4.3.85}$$

As shown in the quadratized equations above, the high-order equations are converted into linear and quadratic equations, introducing additional state variables. Also, the angle constraints are represented in the quadratic equations. The quadratized model can be denoted as an algebraic companion form, in which the components (or devices) are written in the same matrix-form so that all devices in the system to be analyzed can be merged. The algebraic companion form of the three-phase, six-pulse cycloconverter can be reformulated as follows:

$$\begin{bmatrix} I \\ 0 \end{bmatrix} = y_{eq} \begin{bmatrix} V \\ Y \\ X \end{bmatrix} - b_{eq} + \begin{bmatrix} 0 \\ \cdots \\ 0 \\ X^T F_{eq30} X \\ X^T F_{eq31} X \\ \cdots \\ X^T F_{eq57} X \\ 0 \end{bmatrix} \tag{4.3.86}$$

where: $X = [V \;\; Y \;\; X_1 \;\; X_2]^T$;

$$I = [I_{aHr} \;\; I_{aHi} \;\; I_{bHr} \;\; I_{bHi} \;\; I_{cHr} \;\; I_{cHi} \;\; I_{aLr} \;\; I_{aLi} \;\; I_{bLr} \;\; I_{bLi} \;\; I_{cLr} \;\; I_{cLi}]^T;$$

$$V = [V_{aHr} \;\; V_{aHi} \;\; V_{bHr} \;\; V_{bHi} \;\; V_{cHr} \;\; V_{cHi} \;\; V_{aLr} \;\; V_{aLi} \;\; V_{bLr} \;\; V_{bLi} \;\; V_{cLr} \;\; V_{cLi}];$$

$$Y = [E_{Hr} \;\; E_{Hi} \;\; E_{Lr} \;\; E_{Li} \;\; I_p \;\; I_q \;\; P_L \;\; Q_L \;\; y_1 \;\; y_2 \;\; y_3 \;\; y_4 \;\; r]$$

$$X_1 = [x_1 \;\; x_2 \;\; x_3 \;\; x_4 \;\; x_5 \;\; x_6 \;\; x_7 \;\; x_8 \;\; x_9 \;\; x_{10} \;\; x_{11} \;\; x_{12} \;\; x_{13} \;\; x_{14} \;\; x_{15} \;\; x_{16} \;\; x_{17} \;\; x_{18} \;\; x_{19} \;\; x_{20}]$$

$$X_2 = [x_{21} \;\; x_{22} \;\; x_{23} \;\; x_{24} \;\; x_{25} \;\; x_{26} \;\; x_{27} \;\; x_{28} \;\; x_{29} \;\; x_{30} \;\; x_{31} \;\; x_{32} \;\; x_{33}]$$

4.4 Averaging Model of a Three-Phase, PWM Converter

A three-phase, pulse-width-modulation (PWM) converter is modeled in the averaging modeling concept. The averaging method is used for two modes: a VQ-control (DC-voltage and reactive power control) mode and a PQ-control (real-power and reactive-power control) mode. Since the averaging model of the converter using the PQ-control mode is almost the same as that using VQ-control, the averaging model of the PWM converter with the VQ-control mode is only modeled in this subsection. The averaging model of the PWM converter consists of simplified limiting current reactors (-*jB*) and simplified internal admittances (*G*) as shown in Figure 4.3. The converter is controlled based on space-vector modulation (SVM) using the modulation index, which is the relationship between input voltage and output voltage. Note that converters with the PQ- and VQ-control mode can be used as both an inverter and a rectifier.

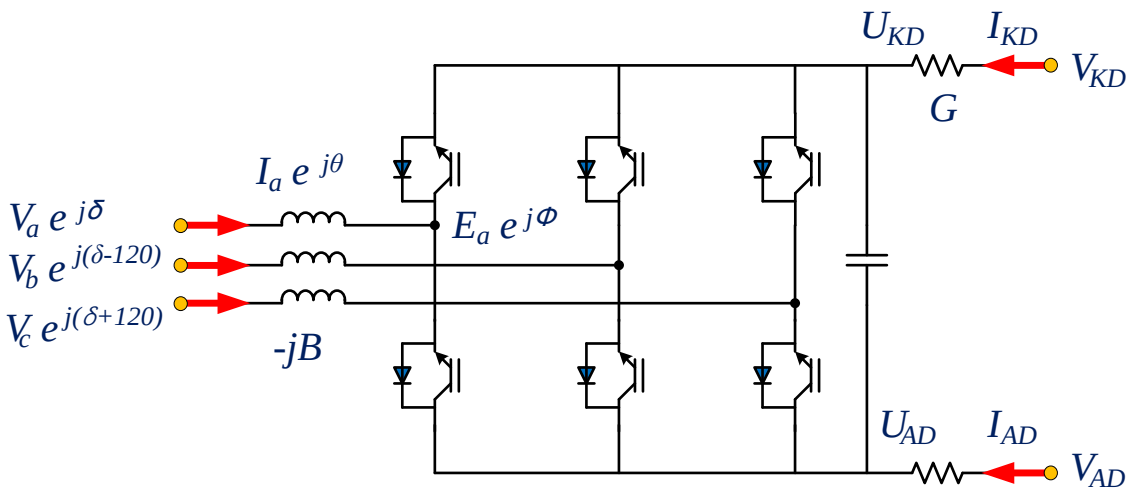

Figure 4.3: An averaging model of a three-phase, PWM converter.

For the VQ-control mode, the averaging model of the three-phase, PWM converter is denoted as state equations. The model equations are as follows:

$$\tilde{I}_a = -jB(\tilde{V}_a - \tilde{E}_a) \tag{4.4.1}$$

$$\tilde{I}_b = -jB(\tilde{V}_b - \tilde{E}_b) \tag{4.4.2}$$

$$\tilde{I}_c = -jB(\tilde{V}_c - \tilde{E}_c) \tag{4.4.3}$$

$$I_{KD} = G\left(V_{KD} - U_{KD}\right) \tag{4.4.4}$$

$$I_{AD} = G\left(V_{AD} - U_{AD}\right) \tag{4.4.5}$$

$$0 = (V_{kd} - V_{Ad}) \cdot I_{Ad} + \frac{2 \cdot I_{Ad}^2}{G} - \mathrm{Re}\left\{V_a I_a^* + V_b I_b^* + V_c I_c^*\right\} \tag{4.4.6}$$

$$0 = I_{KD} + I_{AD} = G\left(V_{KD} - U_{KD}\right) + G\left(V_{AD} - U_{AD}\right) \tag{4.4.7}$$

$$0 = \sqrt{3}\left|\tilde{E}_a\right| \cdot m_a - 0.707\left(U_{KD} - U_{AD}\right) \tag{4.4.8}$$

$$0 = \sqrt{3}\left|\tilde{E}_a\right| - 0.707 U_{dc.\max} \tag{4.4.9}$$

$$0 = -U_{dc.\max} \cdot m_a + V_{dc.ref} - 2U_{KD} + 2V_{KD} \tag{4.4.10}$$

$$0 = Q_{ref} - \mathrm{Im}\left\{V_a I_a^* + V_b I_b^* + V_c I_c^*\right\} \tag{4.4.11}$$

$$0 \le m_a \le 1 \tag{4.4.12}$$

where m_a is the modulation index, and $V_{dc.ref}$ is the reference voltage at the DC-side of the converter. Equations (4.3.1) to (4.3.5) are external state equations, and Equations (4.3.6) to (4.3.11) are internal state equations, while Equation (4.4.12) is a constraint of the modulation index.

The model equations derived from the PWM converter can be represented as phasor representations and quadratized equations using model quadratization to convert nonlinear equations into linear and quadratic equations. The averaging model of the PWM converter can be rewritten as follows:

$$I_{ar} = BV_{ai} - BE_i \tag{4.4.13}$$

$$I_{ai} = -BV_{ar} + BE_r \tag{4.4.14}$$

$$I_{br} = BV_{bi} + \left(\sqrt{3}/2\right)B \cdot E_r + 0.5 \cdot B \cdot E_i \tag{4.4.15}$$

$$I_{bi} = -BV_{br} - 0.5 \cdot B \cdot E_r + \left(\sqrt{3}/2\right)B \cdot E_i \tag{4.4.16}$$

$$I_{cr} = BV_{ci} - \left(\sqrt{3}/2\right)B \cdot E_r + 0.5 \cdot B \cdot E_i \tag{4.4.17}$$

$$I_{ci} = -BV_{cr} - 0.5 \cdot B \cdot E_r - \left(\sqrt{3}/2\right)B \cdot E_i \tag{4.4.18}$$

$$I_{KD \cdot r} = GV_{KD \cdot r} - GU_{KD \cdot r} \tag{4.4.19}$$

$$I_{KD \cdot i} = 1.0 \cdot V_{KD \cdot i} \tag{4.4.20}$$

$$I_{AD \cdot r} = GV_{AD \cdot r} - GU_{AD \cdot r} \tag{4.4.21}$$

$$I_{AD \cdot i} = 1.0 \cdot V_{AD \cdot i} \tag{4.4.22}$$

$$0 = GV_{KD \cdot r} - GU_{KD \cdot r} + GV_{AD \cdot r} - GU_{AD \cdot r} \tag{4.4.23}$$

$$0 = \sqrt{3}x_1 - 0.707U_{dc.\max} \tag{4.4.24}$$

$$0 = x_2 - V_{ai} + E_i \tag{4.4.25}$$

$$0 = x_3 + V_{ar} - E_r \tag{4.4.26}$$

$$0 = x_4 - V_{bi} - \left(\sqrt{3}/2\right)E_r - 0.5E_i \tag{4.4.27}$$

$$0 = x_5 + V_{br} + 0.5E_r - \left(\sqrt{3}/2\right)E_i \tag{4.4.28}$$

$$0 = x_6 - V_{ci} + \left(\sqrt{3}/2\right)E_r - 0.5E_i \tag{4.4.29}$$

$$0 = x_7 + V_{cr} + 0.5E_r + \left(\sqrt{3}/2\right)E_i \tag{4.4.30}$$

$$0 = x_8 - V_{AD.r} + U_{AD.r}$$

$$0 = G \cdot x_8(V_{KD.r} - V_{AD.r}) + 2G \cdot x_8^2 - B\left(x_2V_{ar} + x_3V_{ai} + x_4V_{br} + x_5V_{bi} + x_6V_{cr} + x_7V_{ci}\right) \tag{4.4.31}$$

$$0 = Q_{ref} - B \cdot x_2 V_{ai} + B \cdot x_3 V_{ar} - B \cdot x_4 V_{bi} + B \cdot x_5 V_{br} - B \cdot x_6 V_{ci} + B \cdot x_7 V_{cr} \tag{4.4.32}$$

$$0 = -U_{dc.\max} \cdot m_a + V_{ref} + 2U_{KD \cdot r} - 2V_{KD \cdot r} \tag{4.4.33}$$

$$0 = \sqrt{3} x_1 \cdot m_a - 0.707\left(U_{KD \cdot r} - U_{AD \cdot r}\right) \tag{4.4.34}$$

$$0 = x_1^2 - E_r^2 - E_i^2 \tag{4.4.35}$$

$$0 = 1 - m_a^2 - x_9^2 \tag{4.4.36}$$

$$0 = m_a - x_{10}^2 \tag{4.4.37}$$

$$0 = x_1 - x_{11}^2 \tag{4.4.38}$$

$$0 = x_{12} \tag{4.4.39}$$

As shown in the quadratized equations above, the high-order equations are converted into linear and quadratic equations, introducing additional state variables. Also, the constraint of the modulation index is represented in quadratic equations. The quadratized model can be denoted as an algebraic companion form, in which the components (or devices) are written in the same matrix form so that all devices in the system to be analyzed can be merged. The algebraic companion form of the three-phase, PWM converter can be reformulated as follows:

$$\begin{bmatrix} I \\ 0 \end{bmatrix} = y_{eq} \begin{bmatrix} V \\ Y \\ X \end{bmatrix} - b_{eq} + \begin{bmatrix} V \\ Y \\ X \end{bmatrix}^T \begin{bmatrix} 0 \\ \cdots \\ 0 \\ F_{eq19} \\ F_{eq20} \\ F_{eq21} \\ F_{eq22} \\ \vdots \\ F_{eq26} \\ 0 \end{bmatrix} \begin{bmatrix} V \\ Y \\ X \end{bmatrix} \tag{4.4.40}$$

where: $X = [V \quad Y \quad X]^T$;

$$I = \begin{bmatrix} I_{ar} & I_{ai} & I_{br} & I_{bi} & I_{cr} & I_{ci} & I_{KD\cdot r} & I_{KD\cdot i} & I_{AD\cdot r} & I_{AD\cdot i} \end{bmatrix};$$

$$V = \begin{bmatrix} V_{ar} & V_{ai} & V_{br} & V_{bi} & V_{cr} & V_{ci} & V_{KD\cdot r} & V_{KD\cdot i} & V_{AD\cdot r} & V_{AD\cdot i} \end{bmatrix};$$

$$Y = \begin{bmatrix} E_r & E_i & U_{KD\cdot r} & U_{AD\cdot r} & m_a & U_{dc.\max} \end{bmatrix}; \text{ and}$$

$$X = [\, x_1 \;\; x_2 \;\; x_3 \;\; x_4 \;\; x_5 \;\; x_6 \;\; x_7 \;\; x_8 \;\; x_9 \;\; x_{10} \;\; x_{11} \;\; x_{12} \,].$$

4.5 Summary

This section presents the averaging models of converters: a three-phase, six-pulse converter, a three-phase, six-pulse cycloconverter, and a three-phase, PWM converter. These models are based on model quadratization and phasor representation in the frequency-domain. The models have the advantages of simple and fast analysis in quantitative analysis, such as the power transfer capability of transmission systems, electrical loss analysis, etc. Also, the models can be used in a quasi-steady state in which the converters are operating in sinusoidal, steady-state condition, and it is assumed that mechanical system of generators is only working dynamically [29]. The quasi-steady-state models can be used to analyze the dynamical behavior of specific frequency.

CHAPTER 5

FULL TIME-DOMAIN MODELS OF CONVERTERS

5.1 Introduction

This section presents the time-domain models of a three-phase, six-pulse converter, a three-phase, six-pulse cycloconverter, and a three-phase, PWM converter. Time-domain models are utilized to better understand the dynamic behavior of power systems, such as the operation of electrical switches, harmonics, and power transients. In this section, realistic models of converters consisting of physical components (such as resistors, inductors, capacitors, electrical switches, etc.) are presented. The modeling methodology is based on a combination of model quadratization and quadratic integration (QMQI), which is explained in Chapter 3. Since the modeling process of converters is almost the same as that of the push-pull resonant converter shown in Chapter 3, converter models are explained below in brevity.

5.2 A Three-Phase, Six-Pulse Converter

A three-phase, six-pulse converter is modeled in two parts: modeling an equivalent circuit of the three-phase, six-pulse converter and designing a specific controller to generate switching pulses. The three-phase converter is based on an equidistant-control algorithm using the firing delay angle (α), in which the firing pulses are generated at the same interval of 60^{o}. The equidistant control algorithm has demonstrated a characteristic to minimize total harmonic distortion among phase-control algorithms for the three-phase,

six-pulse converter [28]. The modeling methodology and the equidistant firing angle control of the three-phase, six-pulse converter have been presented in previous research from [30] to [31], according to their own modeling methodology. In this subsection, the QMQI method is introduced to model the three-phase, six-pulse converter, thereby leading a more realistic and reliable model of the converter in time-domain.

5.2.1 Equivalent Circuit of a Three-Phase, Six-Pulse Converter

A six-pulse converter consists of six valves containing a thyristor, a snubber circuit, and a current-rate-limiting circuit. They are interconnected to yield the topology of the three-phase, six-pulse converter. The overall system of the three-phase, six-pulse converter is shown in Figure 5.1.

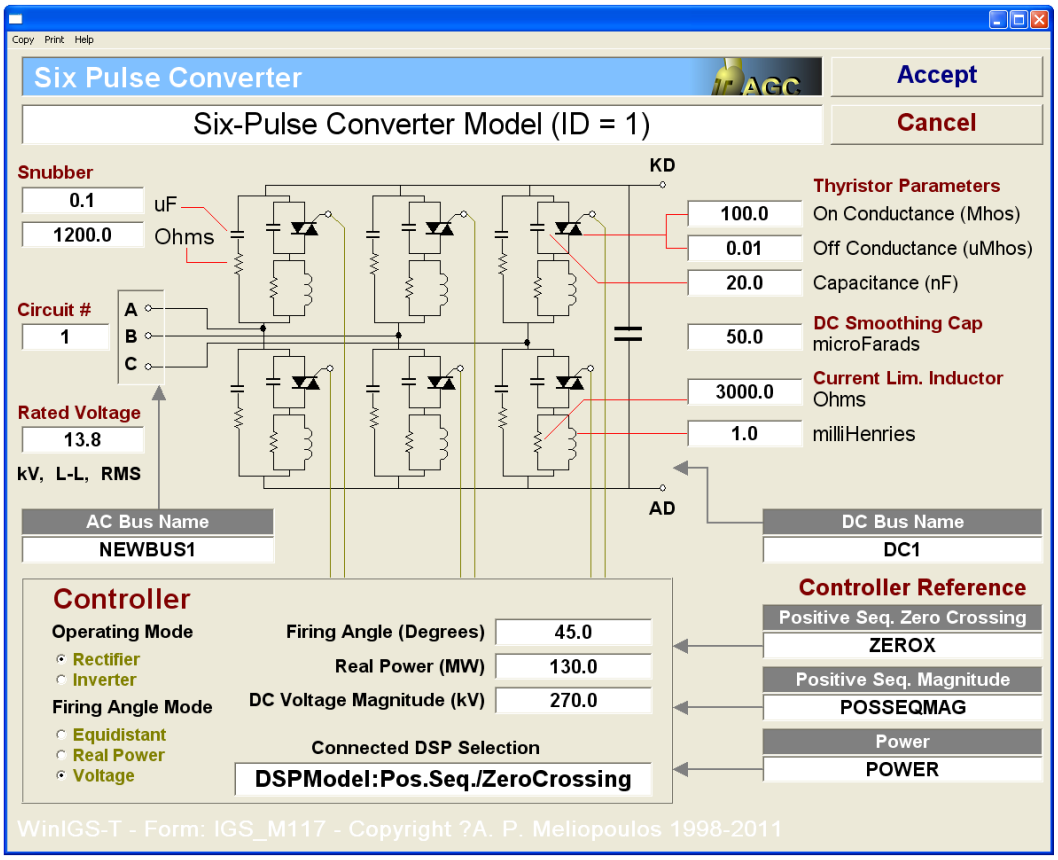

Figure 5.1: Input-data form of the three-phase six-pulse converter

The circuit parameters of the three-phase, six-pulse converter are as follows:

$G_{V1} \sim G_{V6}$: thyristor conductance of each valve;

R_S : snubber circuit resistance;

C_S : snubber circuit capacitance;

$R = 1/G$: resistance in parallel with reactor;

L : current rate limiting inductance;

C_P : thyristor parasitic capacitance; and

C : DC side smoothing capacitance.

Since the three-phase, six-pulse converter is a complex system with several physical components (of six valves and a capacitor), each component is modeled and merged to form an entire system. Thus, the QMQI method is applied to each component and Newton's method is performed after merging all components. Since the modeling process is presented in our previous research of [17], as well as in Chapter 3, the state equations of an electrical valve, shown in Figure 5.2 and a smoothing capacitor, shown in Figure 5.3 are only presented in this subsection.

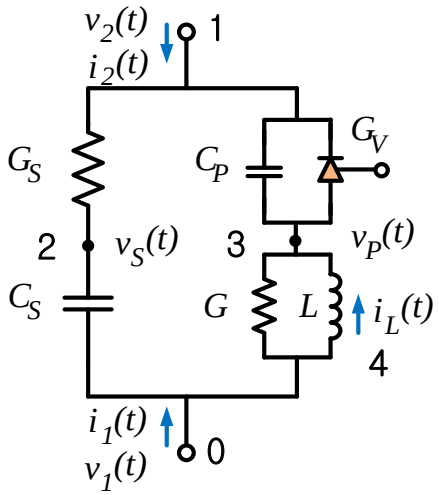

Figure 5.2: An electrical-valve model.

The state equations of the electrical valve are written as a set of algebraic equations and differential equations as follows:

$$i_1(t) = G \cdot [v_1(t) - v_P(t)] + G_s[v_S(t) - v_2(t)] + i_L(t) \quad (5.2.1)$$

$$i_2(t) = G \cdot [v_P(t) - v_1(t)] + G_s[v_2(t) - v_S(t)] - i_L(t) \quad (5.2.2)$$

$$0 = G_S \cdot [v_S(t) - v_2(t)] + C_S \frac{d}{dt}[v_S(t) - v_1(t)] \quad (5.2.3)$$

$$0 = G_V \cdot [v_P(t) - v_2(t)] + C_P \frac{d}{dt}[v_P(t) - v_2(t)] + G \cdot [v_P(t) - v_1(t)] - i_L(t) \quad (5.2.4)$$

$$0 = -v_1(t) + v_P(t) + L\frac{d}{dt} i_L(t) \quad (5.2.5)$$

Note that the electrical-valve model is represented with conductance G_V. This conductance-value (G_V) changes, according to the valve states (on-state: G_{Von} and off-state: G_{Voff}).

The smoothing capacitor, shown in Figure 5.3, is used for reducing voltage ripples at the DC-side, leading constant DC-voltage.

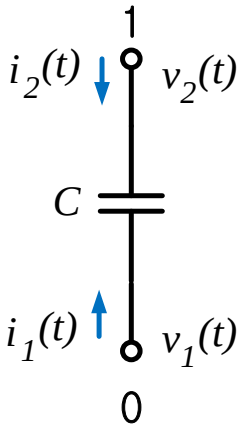

Figure 5.3: A smoothing capacitor model.

The state equations of the smoothing capacitor are as follows:

$$i_1(t) = Cy_1(t) \tag{5.2.6}$$

$$i_2(t) = -i_1(t) \tag{5.2.7}$$

$$\frac{dv_c(t)}{dt} = y_1(t) \tag{5.2.8}$$

$$0 = v_c(t) - v_1(t) + v_2(t) \tag{5.2.9}$$

5.2.2 Control Algorithm: Equidistant Firing Angle Control

The converter controller can be a complex system, depending on the sophistication of the control scheme and the objectives of the designers. In this section, a specific controller is demonstrated for the three-phase, six-pulse converter, which is referred as an equidistant firing controller, and its integration into the quadratic-integration method. The implementation of the control scheme consists of two steps. In the first step, an estimation method is applied to determine the control references. In the second step, the equidistant control scheme using the firing-delay angle, α, related to the control references, is applied to decide the switching time of the six valves. The six-pulse converter can be controlled with a number of strategies. The equidistant firing angle control is elected, since the control algorithm is suitable for high-power converters connected to grid systems. The digital controller for the equidistant control includes an estimator of control references, and the actual control in terms of the equidistant valve firing pulses [30]-[31].

The control references in the equidistant control algorithm consist of two parameters: magnitude and zero-crossing time of line-to-line voltage (V_{AB}) between phase

A and phase B. Since converter systems contain several components with nonlinear characteristics, V_{AB} can be distorted by harmonics. For better accuracy of the control scheme references, first the positive sequence of fundamental frequency is estimated by using Fourier-series analysis and modal decomposition, and then the reference is computed (V_{ab1}).

For the equidistant control scheme, the firing delay angle (α) is used to control the switching sequence. The scheme of equidistant control is shown in Figure 5.4.

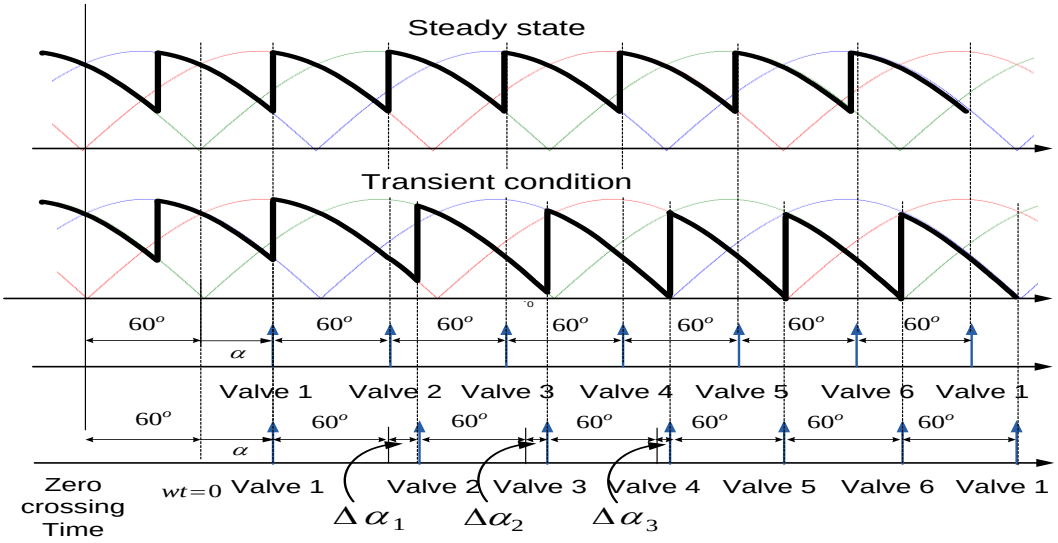

Figure 5.4: Scheme of equidistant control for switching sequence

In steady-state, the six firing signals for the six thyristors are generated from the zero-crossing time and are arranged in equal intervals of 60^0 from each signal pulse. Since the alternative transmission systems are dynamic systems with their specific transient responses, such as power order changes, feeding power variations, and frequency variations, the firing delay angle has to be regulated until the system reaches the steady-state, as shown in Figure 5.4. Thus, the controller of the six-pulse converter have to regulate the switching sequences in real-time to meet these requirements from the

systems. Therefore, the next subsection is dedicated to a dynamic control algorithm for the three-phase, six-pulse converter: the methodology to estimate the references and the equidistant firing controller with the following titles:

- Estimation of control references; and
- Dynamic control using the equidistant firing angle algorithm.

5.2.2.1 Estimation of Control References for Equidistant Control

The exact control of the three-phase, six-pulse converter depends on the estimation of references for the on-state switching sequence, since thyristors are automatically turned-off during reverse bias. Here, zero-crossing time, magnitude, and the phase angle of a voltage (line-to-line voltage between phase A and phase B) will be estimated as control references. For this purpose, a digital signal processor (DSP) is used as shown in Figure 5.5.

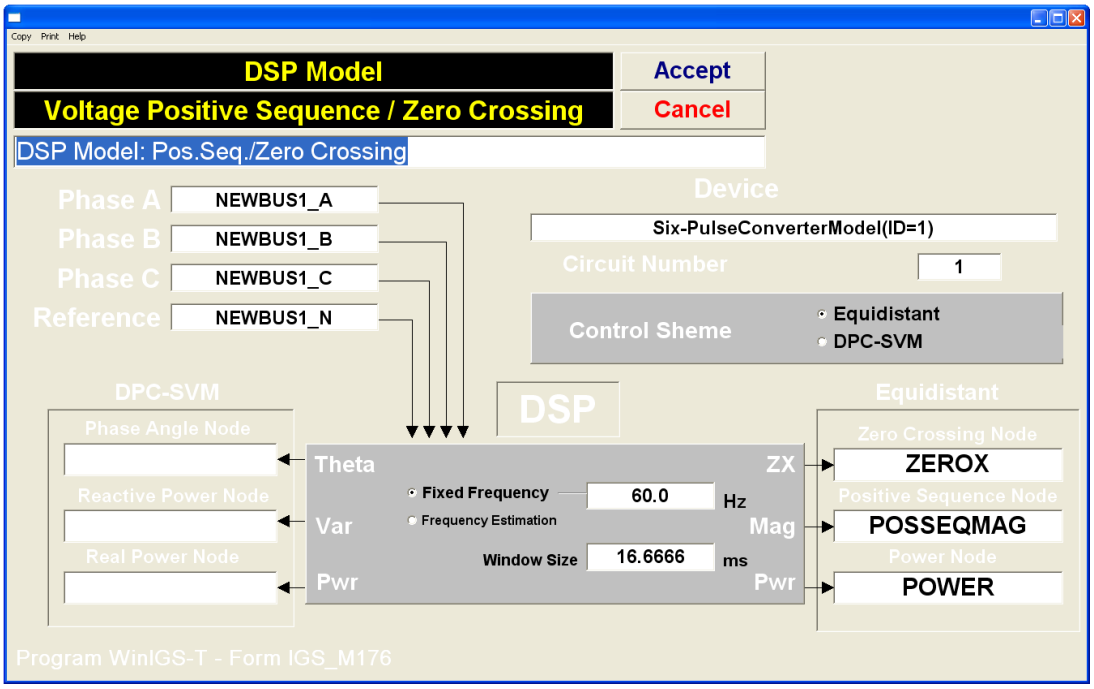

Figure 5.5: A DSP model to estimate control references.

First, the fundamental voltages of $v_{ab}(t)$, $v_{bc}(t)$, *and* $v_{ca}(t)$ can be estimated by the application of *Fourier Series* representation as follows:

$$v_{ab}(t) = \sum_{k=1}^{\infty} \left[a_{ABk} \cos k(\omega t) + b_{ABk} \sin k(\omega t) \right] \tag{5.2.10}$$

$$v_{bc}(t) = \sum_{k=1}^{\infty} \left[a_{BCk} \cos k(\omega t) + b_{BCk} \sin k(\omega t) \right] \tag{5.2.11}$$

$$v_{ca}(t) = \sum_{k=1}^{\infty} \left[a_{CAk} \cos k(\omega t) + b_{CAk} \sin k(\omega t) \right] \tag{5.2.12}$$

To compute the *Fourier* coefficient, a_{AB1}, of the fundamental component of the voltage $v_{ab}(t)$, Equation (5.2.10) is multiplied by $\cos(\omega t_j)$, which is described by the fundamental frequency, and the result is then integrated over one period *T* numerically as follows:

$$\int_{t}^{t+T} v_{ab}(\tau)\cos(\omega\tau)d\tau = \int_{t}^{t+T} a_{AB1}\cos^2(\omega\tau)d\tau \tag{5.2.13}$$

$$a_{AB1} = \frac{2}{m}\left[\sum_{j=1}^{m} v_{ab}(t_j)\cos(\omega t_j) \right] \tag{5.2.14}$$

where $j = 1, 2, \cdots, m$, which is equivalent to one period, and the period is the reciprocal of the fundamental frequency.

Also Equation (5.2.10) is multiplied by $\sin(\omega t_j)$ and the result is integrated. The coefficient b_{AB1} can be computed as follows:

$$b_{AB1} = \frac{2}{m}\left[\sum_{j=1}^{m} v_{ab}(t_j)\sin(\omega t_j) \right] \tag{5. 2.15}$$

Application of the same procedure to the voltage $v_{bc}(t)$ and $v_{ca}(t)$ yields:

$$a_{BC1} = \frac{2}{m}\left[\sum_{j=1}^{m} v_{bc}(t_j)\cos(\omega t_j)\right] \quad (5.\ 2.16)$$

$$b_{BC1} = \frac{2}{m}\left[\sum_{j=1}^{m} v_{bc}(t_j)\sin(\omega t_j)\right] \quad (5.\ 2.17)$$

$$a_{CA1} = \frac{2}{m}\left[\sum_{j=1}^{m} v_{ca}(t_j)\cos(\omega t_j)\right] \quad (5.\ 2.18)$$

$$b_{CA1} = \frac{2}{m}\left[\sum_{j=1}^{m} v_{ca}(t_j)\sin(\omega t_j)\right] \quad (5.\ 2.19)$$

Note that at each time-step, the quantities a_{AB1}, a_{BC1}, a_{CA1}, b_{AB1}, b_{BC1}, and b_{CA1} can be computed. The fundamental frequency components of all three-phase voltages in polar coordinates can be expressed as follows:

$$\tilde{V}_{AB1} = V_{AB1}\angle\phi_{AB1}, \text{ where } V_{AB1} = \sqrt{a_{AB1}^2 + b_{AB1}^2}, \quad \phi_{AB1} = \tan^{-1}\left(-\frac{b_{AB1}}{a_{AB1}}\right) \quad (5.\ 2.20)$$

$$\tilde{V}_{BC1} = V_{BC1}\angle\phi_{BC1}, \text{ where } V_{BC1} = \sqrt{a_{BC1}^2 + b_{BC1}^2}, \quad \phi_{BC1} = \tan^{-1}\left(-\frac{b_{BC1}}{a_{BC1}}\right) \quad (5.\ 2.21)$$

$$\tilde{V}_{CA1} = V_{CA1}\angle\phi_{CA1}, \text{ where } V_{CA1} = \sqrt{a_{CA1}^2 + b_{CA1}^2}, \quad \phi_{CA1} = \tan^{-1}\left(-\frac{b_{CA1}}{a_{CA1}}\right) \quad (5.\ 2.22)$$

Therefore, the fundamental frequency component of $v_{ab}(t)$ is written as follows:

$$v_{AB1}(t) = a_{AB1}\cos(\omega t) + b_{AB1}\sin(\omega t) = V_{AB1}\cos(\omega t + \phi_{AB1}) \quad (5.\ 2.23)$$

A similar expression can be written for the other two phases as follows:

$$v_{BC1}(t) = a_{BC1}\cos(\omega t) + b_{BC1}\sin(\omega t) = V_{BC1}\cos(\omega t + \phi_{BC1}) \quad (5.\ 2.23)$$

$$v_{CA1}(t) = a_{CA1}\cos(\omega t) + b_{CA1}\sin(\omega t) = V_{CA1}\cos(\omega t + \phi_{CA1}) \quad (5.\ 2.23)$$

The three-phase phasor notations may be unbalanced and may contain negative and zero sequence components. To use the positive sequence fundamental component as the

reference voltage, *modal decomposition* is performed to extract the positive sequence component from the three unbalanced phasors. The transformation process is expressed in the following relation:

$$\begin{bmatrix} \tilde{V}_{ab1} \\ \tilde{V}_{ab2} \\ \tilde{V}_{ab0} \end{bmatrix} = \frac{1}{3} \cdot \begin{bmatrix} 1 & a & a^2 \\ 1 & a^2 & a \\ 1 & 1 & 1 \end{bmatrix} \begin{bmatrix} \tilde{V}_{AB1} \\ \tilde{V}_{BC1} \\ \tilde{V}_{CA1} \end{bmatrix} \text{ where } a = e^{j\frac{2\pi}{3}} \qquad (5.\ 2.24)$$

where $\tilde{V}_{ab1}, \tilde{V}_{ab2}$ and $\tilde{V}_{ab0}$ are the positive, negative and zero sequence components of $\tilde{V}_{AB1}$, respectively.

Therefore, the positive sequence component of the fundamental components of line–to-line voltage $v_{ab1}(t)$ obtained from the Fourier analysis and modal decomposition can be expressed as follows:

$$v_{ab1}(t) = V_{ab1}\cos(\omega t + \phi_{V_{ab1}}) \qquad (5.\ 2.25)$$

$$= \frac{1}{3} \cdot \left[V_{AB1}\cos(\omega t + \phi_{AB1}) + V_{BC1}\cos\left(\omega t + \phi_{BC1} + \frac{2\pi}{3}\right) + V_{CA1}\cos\left(\omega t + \phi_{CA1} + \frac{4\pi}{3}\right) \right]$$

$$= \frac{1}{3} \cdot \left[V_X \cos(\omega t) + V_Y \sin(\omega t) \right]$$

where:

$$V_X = + \left[V_{AB1}\cos(\phi_{AB1}) + V_{BC1}\cos\left(\phi_{BC1} + \frac{2\pi}{3}\right) + V_{CA1}\cos\left(\phi_{CA1} + \frac{4\pi}{3}\right) \right];$$

$$V_Y = - \left[V_{AB1}\sin(\phi_{AB1}) + V_{BC1}\sin\left(\phi_{BC1} + \frac{2\pi}{3}\right) + V_{CA1}\sin\left(\phi_{CA1} + \frac{4\pi}{3}\right) \right].$$

Therefore, the peak value and phase angle of the line-to-line voltage $v_{ab1}(t)$ are calculated as follows:

$V_{ab1} = \frac{1}{3} \cdot \sqrt{V_X{}^2 + V_Y{}^2}$ is the peak line voltage; (5. 2.26)

$\phi_{V_{ab1}} = \tan^{-1}\left(-\frac{V_Y}{V_X}\right)$ is the phase angle of line voltage. (5. 2.27)

For power-flow control, it is necessary to compute the real power of the converter. The real-power is computed by using the positive sequence fundamental voltage and current. The positive sequence fundamental currents of $i_a(t)$, $i_b(t)$, and $i_c(t)$ are computed with the same procedure of the positive sequence fundamental voltage as follows:

$$i_a(t) = \sum_{k=1}^{\infty}\left[p_{Ak}\cos k(\omega t) + q_{Ak}\sin k(\omega t)\right] \quad (5.\ 2.28)$$

$$i_b(t) = \sum_{k=1}^{\infty}\left[p_{Bk}\cos k(\omega t) + q_{Bk}\sin k(\omega t)\right] \quad (5.\ 2.29)$$

$$i_c(t) = \sum_{k=1}^{\infty}\left[p_{Ck}\cos k(\omega t) + q_{Ck}\sin k(\omega t)\right] \quad (5.\ 2.30)$$

After computing the phasors, denoted by the magnitudes and angles of all three phases, the positive sequence fundamental current is also computed in a phasor form as follows:

$$I_X = +\left[I_{A1}\cos(\phi_{A1}) + I_{B1}\cos\left(\phi_{B1} + \frac{2\pi}{3}\right) + I_{C1}\cos\left(\phi_{C1} + \frac{4\pi}{3}\right)\right] \quad (5.\ 2.31)$$

$$I_Y = -\left[I_{A1}\sin(\phi_{A1}) + I_{B1}\sin\left(\phi_{B1} + \frac{2\pi}{3}\right) + I_{C1}\sin\left(\phi_{C1} + \frac{4\pi}{3}\right)\right] \quad (5.\ 2.32)$$

Also, the positive sequence fundamental current can be described as follows:

$$i_{a1}(t) = I_{a1}\cos(\omega t + \phi_{i_{a1}}) \quad (5.2.33)$$

where:

$$I_{a1} = \frac{1}{3} \cdot \sqrt{I_X{}^2 + I_Y{}^2} \quad \text{is the peak current;} \tag{5.2.34}$$

$$\phi_{i_{a1}} = \tan^{-1}\left(-\frac{I_Y}{I_X}\right) \quad \text{is the phase angle.} \tag{5.2.35}$$

The phasors of the positive sequence fundamental voltage and current are denoted as $\tilde{V}_{a1} = V_{ab1} e^{j\phi_{V}ab1}$ and $\tilde{I}_{a1} = I_{a1} e^{j\phi_{i}a1}$ from Equations (5.2.25) and (5.2.33). Here, using the computed values of the voltage and current, the real-power of the converter is computed as follows:

$$P = \frac{\sqrt{3}}{2} V_{ab1} I_{a1} \cos\left(\phi_{v_{ab1}} - \frac{\pi}{6} - \phi_{i_{a1}}\right) . \tag{5.2.36}$$

To calculate the zero-crossing time of V_{ab1}, the positive sequence fundamental voltage is used. The equation of the positive sequence component of the fundamental voltage is:

$$v_{ab1}(t) = V_{ab1} \cos(\omega t + \phi_V) \tag{5.2.37}$$

From the equation above, the zero-crossing time is calculated as follows.

$$\omega t_R + \phi_V - \frac{\pi}{2} = \phi_R \tag{5.2.38}$$

$$\omega t_{o1} + \phi_V = 2\pi n \quad where\ n = \frac{\phi_R}{360^o} \tag{5.2.39}$$

$$t_{o1} = \frac{2\pi n - \phi_v}{w} \tag{5.2.40}$$

$$t_o = t_{o1} - \frac{\pi}{2w} = \frac{2\pi n - \phi_v}{w} - \frac{\pi}{2w} \tag{5.2.41}$$

where: t_R is the nearest zero-crossing time from the running time;

t_{01} is the time at the maximum value of v_{ab1}; and

t_0 is the zero-crossing time.

5.2.2.2 Dynamic control using the equidistant firing angle algorithm

The three-phase, six-pulse converter can be controlled with a number of strategies. We have elected to use an equidistant control algorithm to minimize the THD (Total Harmonic Distortion). The digital controller for equidistant control includes an estimator of control references and control action in terms of equidistant valve firing pulses. The estimation of the control references was performed with the DSP model, shown in Figure 5.5, and a dynamic controller using the equidistant control scheme is presented in this subsection. The equidistant control scheme has two modes for a rectifier and an inverter. The rectifier uses the firing delay angle (α), while the inverter is controlled using the extinction angle (γ).

In the equidistant control, the firing pulses for thyristors are generated at equal intervals of 60^{o}. To keep the distance of firing pulses equal, all firing has to be delayed by the same delay angle, α in steady-state. The scheme for the firing sequence for the rectifier mode is shown in Figure 5.6.

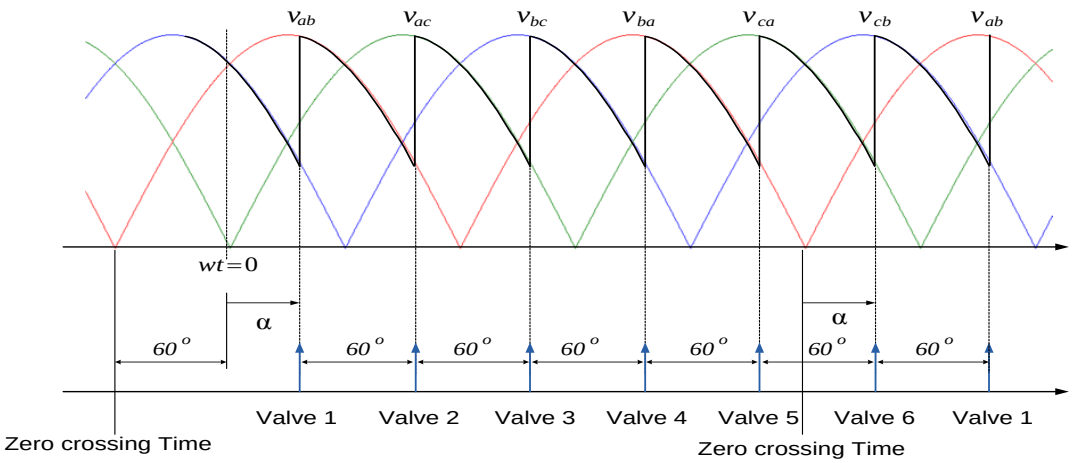

Figure 5.6: The scheme of the equidistant firing angle control in a converter mode.

To compute the firing delay angle, two steps are needed. First, the no-load direct voltage has to be computed, and then the firing delay angle should be calculated. The no-load voltage is a DC-voltage, while the firing angle is zero, as shown in Figure 5.7. The no-load voltage can be computed in the integration of *Area A* in Figure 5.7. The integration is as follows:

$$A=\int_0^{\frac{\pi}{3}}\sqrt{2}v_{LL}\cos\left(wt+\frac{\pi}{6}\right)d(wt)=\sqrt{2}v_{LL}\sin\left(\frac{\pi}{2}\right)-\sqrt{2}v_{LL}\sin(0)=\sqrt{2}v_{LL} \quad (5.2.42)$$

Since one period of the DC-voltage ripples is π/3, the no-load voltage is as follows:

$$V_{d0}=\frac{3}{\pi}\int_0^{\frac{\pi}{3}}\sqrt{2}v_{LL}\cos\left(wt+\frac{\pi}{6}\right)d(wt)=\frac{3\sqrt{2}}{\pi}v_{LL}, \quad (5.2.43)$$

where V_{d0} is the no-load voltage.

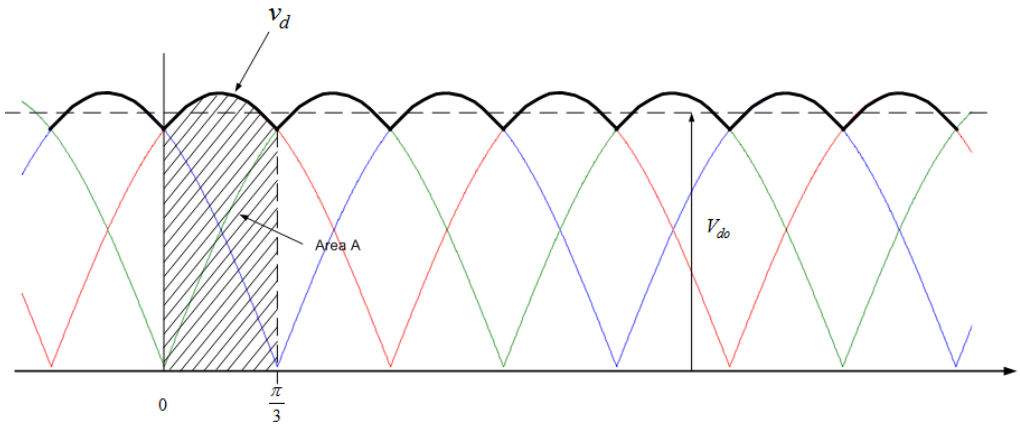

Figure 5.7: Direct voltage, V_d during the time firing delay angle is zero

The limit of integration of *Area A* has to be decreased by α as in Figure5.8. the voltage drop Area A_a is the integral of $v_{ab}-v_{cb}(=v_{ac})$ as follows:

$$v_{ac}=\sqrt{2}v_{LL}\sin wt \quad (5.2.44)$$

$$A_\alpha=\int_0^{\alpha}\sqrt{2}v_{LL}\sin wt\, d(wt)=\sqrt{2}v_{LL}(1-\cos\alpha) \quad (5.2.45)$$

The average DC-voltage from the three-phase, six-pulse converter is computed as follows:

$$V_d = V_{d0} - \frac{A_\alpha}{\pi/3} = \frac{3\sqrt{2}}{\pi} v_{LL} \cos\alpha \tag{5.2.46}$$

$$\alpha = \cos^{-1}\left(\frac{V_d}{V_{d0}}\right) \tag{5.2.47}$$

$$t_{delay} = \frac{\alpha}{360} \times T \tag{5.2.48}$$

where: V_{d0} = Ideal no-load direct voltage;

V_d = direct Voltage of Load side; and

I_d = direct Current of Load side.

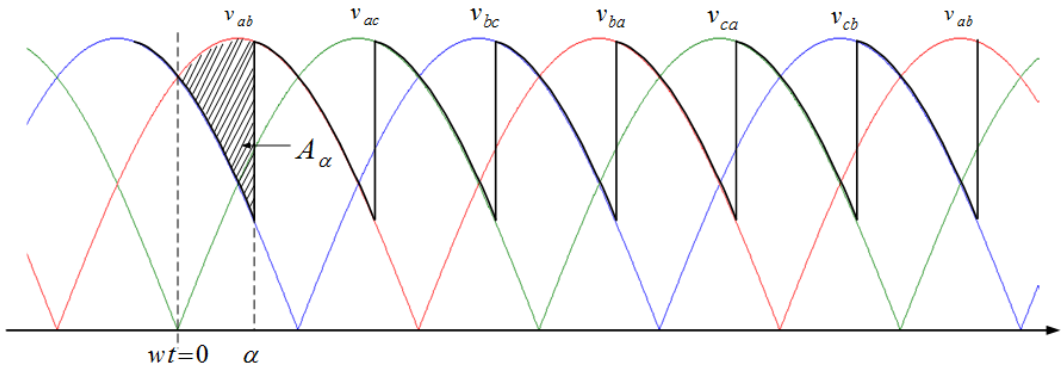

Figure 5.8: Voltage drop according to firing delay, α.

To dynamically control the three-phase, six-pulse converter, the firing delay angle α is controlled based on the calculated value from the relationship between the direct voltage (V_d) and the no-load direct voltage (V_{d0}) at every integration time-step. Figure 5.9 shows the block diagram of the control strategy for constant output-power for the rectifier mode.

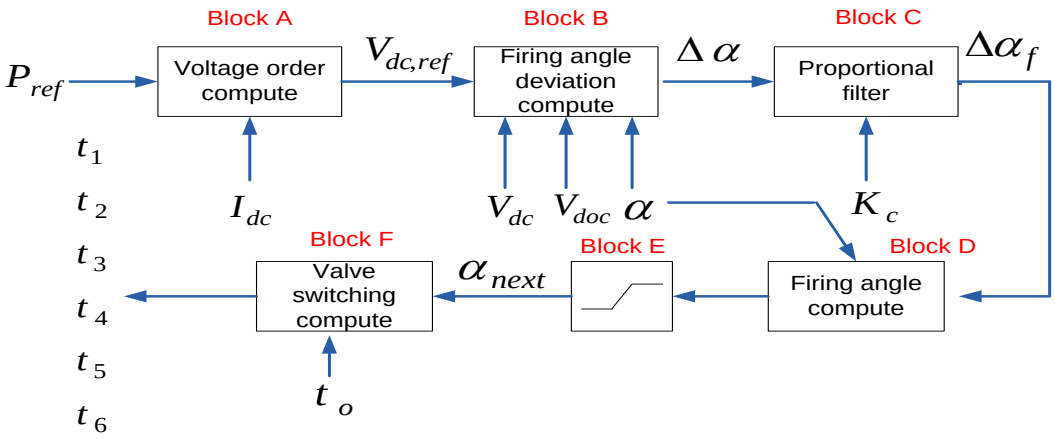

Figure 5.9: The principle of equidistant control for constant output-power in a rectifier mode.

The important parameters for the control scheme of the rectifier mode are as follows:

P_{ref} : Prospective output-power;

P_d : Output-power calculated by using measured voltage and current;

V_{do} : No-load direct-voltage ($V_{d0} = \frac{3\sqrt{2}}{\pi} V_{LL}$);

K : Proportionality constant;

$\Delta\alpha$: Firing angle deviation;

$\Delta\alpha_f$: Filtered firing angle-deviation; and

t_0 : Zero-crossing time of line-to-line voltage between Phase A and Phase B.

The design of each block is explained as follows:

Block A: To compute the voltage order from the prospective output-power.

The reference voltage can be calculated with the prospective output-power and a measured direct-current. The equation is:

$$V_{ref} = \frac{P_{ref}}{I_d} \tag{5.2.49}$$

Note that the maximum value of the direct voltage is ideally the same as the no-load direct voltage, so that the voltage reference has to be limited to the no-load direct voltage.

Block B: To compute the deviation of the firing angle.

The deviation of the firing delay angle for the next time-step is calculated with the present firing angle and no-load direct voltage. The deviation is computed as follows:

$$V_d = V_{d0}\cos\alpha \qquad \text{where } V_{d0} = \frac{3\sqrt{2}}{\pi}V_{LL} \tag{5.2.50}$$

$$\Delta V = -V_{d0}\sin\alpha \cdot \Delta\alpha \qquad \text{where } \Delta V = V_{ref} - V_d \tag{5.2.51}$$

$$\Delta\alpha = \frac{\Delta V}{-V_{d0}\sin\alpha} \tag{5.2.52}$$

Block C: To compute the filtered deviation of the firing angle.

Since sudden changes of the firing angle can generate switching failure or malfunction of the valves, the deviation has to be filtered in order to reduce the changing rate of the firing angle.

$$\Delta\alpha_f = K \cdot \Delta\alpha \qquad \text{where } K \text{ is a proportionality constant} \tag{5.2.53}$$

Block D: To compute the firing angle.

The firing angle for the next step is calculated by summing the present firing-angle and filtered deviation of the firing angle.

$$a_{next} = a_{present} + \Delta a_f \tag{5.2.54}$$

Block E: To check the limitation of the firing angle.

The firing angle has to be limited between 5^0 and 90^0 because assuming that the firing angle is not in this boundary, the deviation of the firing angle cannot be calculated properly. For example, the Δa goes to infinity, assuming that the firing angle is zero,

while assuming that the firing delay angle is bigger than 90^o, the DC voltage will change to its opposite direction, and the converter will work as an inverter.

If the firing angle is smaller than 5^o, then $a = 5^o$

If the firing angle is bigger than 85^o, then $a = 85^o$

Block F: To compute the switching time of each valve.

Once the firing delay t_{delay} has been computed, the closing time of the thyristor valves will be computed as the following time-steps:

$$t_{delay} = \frac{\alpha}{360} \times T$$

Valve 1: $$t_1 = t_o + t_{delay} + \frac{1}{6 f_o} \quad (5.2.55)$$

Valve 2: $$t_2 = t_o + t_{delay} + \frac{2}{6 f_o} \quad (5.2.56)$$

Valve 3: $$t_3 = t_o + t_{delay} + \frac{3}{6 f_o} \quad (5.2.57)$$

Valve 4: $$t_4 = t_o + t_{delay} + \frac{4}{6 f_o} \quad (5.2.58)$$

Valve 5: $$t_5 = t_o + t_{delay} + \frac{5}{6 f_o} \quad (5.2.59)$$

Valve 6: $$t_6 = t_o + t_{delay} + \frac{6}{6 f_o} \quad (5.2.60)$$

where f_o is the fundamental frequency.

The next subsection presents the strategy of inverter control, which is also an equidistant control scheme. However, the relationship between three-phase voltages and DC-voltage in the inverter mode is based on the extinction angle γ, as shown in Figure

5.10. The equations below show the relationship between DC-voltage and no-load voltage in the inverter mode: $V_{di} = V_{d0i}\cos\gamma$,

(5.2.61)

where V_{di} is the DC-voltage, and V_{d0i} is the no-load direct voltage in the inverter mode. From the equation above, the firing angle α is calculated. The relationship between the firing angle and the extinction angle is $\alpha = 180^{o} - \gamma$.

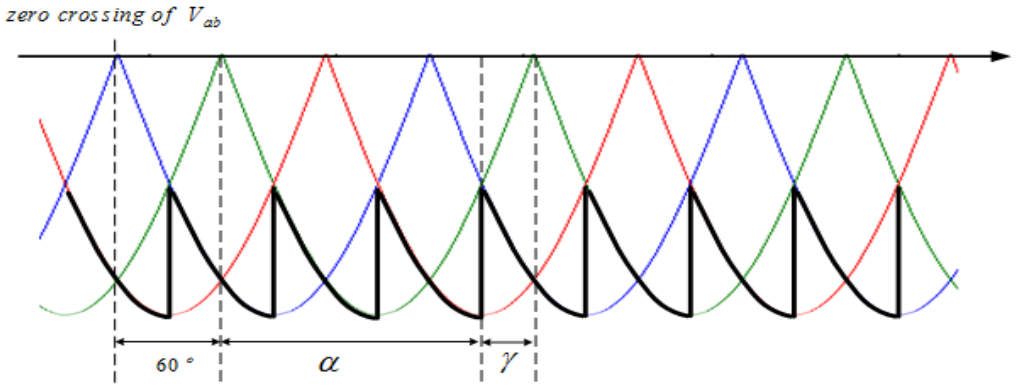

Figure 5.10: The scheme of equidistant-firing-angle control in an inverter mode

To dynamically control the three-phase six-pulse converter, firing delay angle α is controlled based on the calculated value from the relationship between direct voltage (V_d) and ideal no-load direct voltage (V_{d0}) at every integration time-step. Figure 5.11 shows the block diagram of the control strategy for constant output-power for the inverter mode.

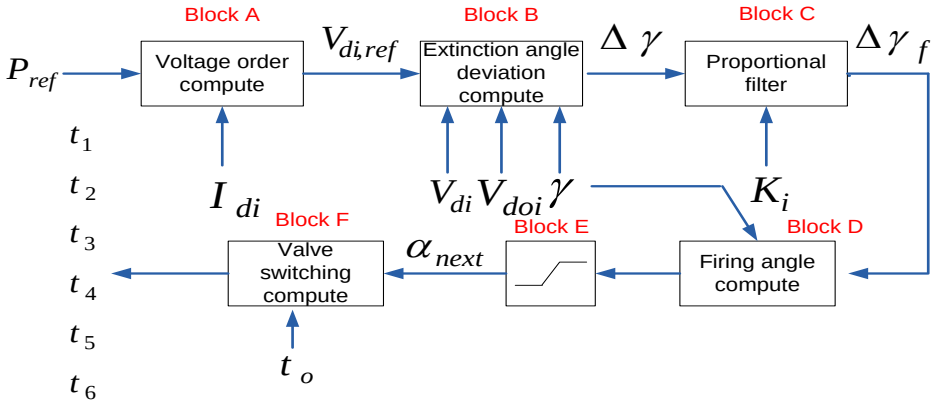

Figure 5.11: The principle of equidistant control for constant output-power in an inverter mode.

The important parameters for the control scheme of the inverter mode are as follows:

p_{ref} :	Prospective DC-power of an inverter;
I_{di} :	DC-current at the inverter side;
$V_{di,\,ref}$:	Reference voltage at the inverter side;
V_{di} :	DC-voltage at inverter side;
γ :	Extinction angle;
$\Delta\gamma$:	Deviation of the extinction angle; and
t_0 :	Zero-crossing time of V_{ab1}.

The design of each block is explained as follows:

Block A: To compute the voltage order from the reference power.

The reference voltage is calculated from the power order p_{ref} and a measured direct current I_{di}. The equation is as follows:

$$V_{di,ref} = \frac{P_{ref}}{I_{di}} \tag{5.2.62}$$

Note that the maximum value of the direct voltage is ideally the same as the no-load direct voltage, so that the voltage reference has to be limited to the no-load voltage.

Block B: To compute the deviation of the extinction angle.

The deviation of the extinction angle is calculated with the present extinction-angle, and the no-load direct-voltage. The deviation is computed as follows:

$$V_{di} = V_{d0i}\cos\gamma \qquad \text{where } V_{d0i} = \frac{3\sqrt{2}}{\pi}V_{LL} \tag{5.2.63}$$

$$\Delta V_i = -V_{d0i}\sin\gamma\cdot\Delta\gamma \qquad \text{where } \Delta V_i = V_{di,ref} - V_{di} \tag{5.2.64}$$

$$\Delta\gamma = \frac{\Delta V_i}{-V_{d0i}\sin\gamma} \tag{5.2.65}$$

Block C: To compute the filtered deviation of the extinction angle.

Since sudden changes of the extinction angle can lead to sudden changes of the firing angle, the deviation has to be filtered in order to reduce the changing rate of the firing angle.

$$\Delta\gamma_f = K\cdot\Delta\gamma \qquad \text{where } K \text{ is a proportional constant.} \tag{5.2.66}$$

Block D: To compute the firing angle.

The firing delay angle is computed in Block D. The firing angle for the next-step is computed by using the extinction angle, the deviation of the extinction angle, and the commutation angle.

$$a_{next} = 180^o - \gamma - \Delta\gamma - \mu \qquad \text{where } \mu \text{ is commutation angle.} \tag{5.2.67}$$

Block E: To check the limitation of the firing angle.

The firing angle has to be limited between 90 degrees and $a_{\max}$ degrees. Assuming that the firing angle is not bigger than 90 degrees, the inverter will work as a rectifier, and assuming that the firing angle is not smaller than $a_{\max}$ degrees, the switching of valves can experience switching failure.

If the firing angle is smaller than 90^o, then $a = 90^o$

If the firing angle is bigger than $a_{\max}$, then $a = a_{\max}$

where $a_{\max} = 180 - \gamma_{\min} - \mu$

Block F: To compute the switching time of each valve.

Once the firing delay t_{delay} has been computed, the closing time of the thyristor valves will be computed as the following time steps:

$$t_{delay} = \frac{\alpha}{360} \times T$$

Valve 1: $$t_1 = t_o + t_{delay} + \frac{1}{6 f_o} \quad (5.2.68)$$

Valve 2: $$t_2 = t_o + t_{delay} + \frac{2}{6 f_o} \quad (5.2.69)$$

Valve 3: $$t_3 = t_o + t_{delay} + \frac{3}{6 f_o} \quad (5.2.70)$$

Valve 4: $$t_4 = t_o + t_{delay} + \frac{4}{6 f_o} \quad (5.2.71)$$

Valve 5: $$t_5 = t_o + t_{delay} + \frac{5}{6 f_o} \quad (5.2.72)$$

Valve 6: $$t_6 = t_o + t_{delay} + \frac{6}{6 f_o} \quad (5.2.73)$$

where f_o is the fundamental frequency.

5.3 A Three-Phase, Six-pulse Cycloconverter

A three-phase, six-pulse cycloconverter is modeled in two parts: modeling an equivalent circuit of the three-phase, six-pulse cycloconverter and designing a specific controller to generate switching pulses. The three-phase, six-pulse cycloconverter is based on a cosine-wave-crossing algorithm using the firing delay angle (α), in which firing pulses are generated according to the output-voltage reference. The cosine-wave-crossing algorithm has demonstrated a characteristic to minimize total harmonic distortion among phase control algorithms for the three-phase, six-pulse cycloconverter [28]. The modeling methodology and the cosine wave-crossing method of the three-phase, six-pulse cycloconverter have been presented in previous research from [33] to [37], according to their own modeling-methodology. In this subsection, the QMQI method is applied to model the three-phase, six-pulse cycloconverter, leading to a more realistic and reliable model of a converter in full time-domain.

5.3.1 Equivalent Circuit of a Three-Phase, Six-Pulse Cycloconverter

The three-phase, six-pulse cycloconverter consists of three single-phase, six-pulse cycloconverters, and the each single-phase, six-pulse cycloconverter consists of twelve electrical-valves, (which consist of a limiting current reactor and resistor, and a snubber capacitor and resistor) circulating current reactors, and three-phase isolation transformers. Figure 5.12 shows the entire system of the three-phase, six-pulse cycloconverter.

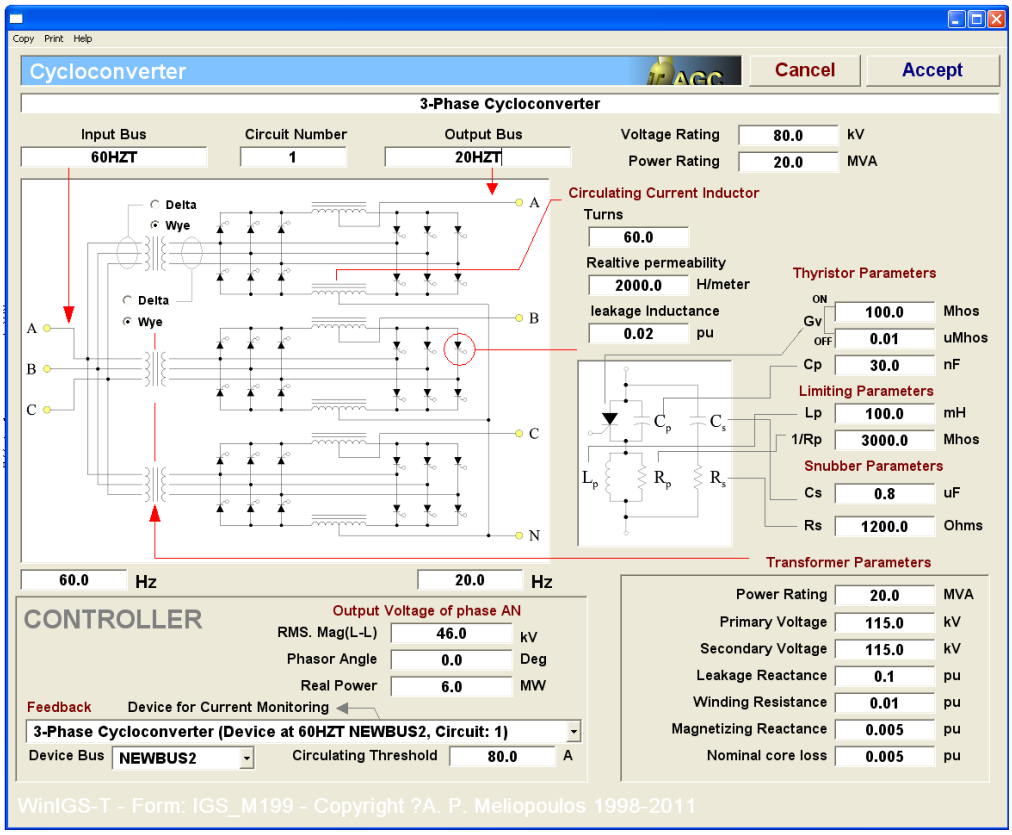

Figure 5.12: Input-data form of the three-phase six-pulse cycloconverter.

The circuit parameters of the cycloconverter above are represented as follows:

G_v : Thyristor conductance of each valve (G_{v_off} and G_{v_on});

R_S : Snubber circuit resistance;

$R = 1/G$: Resistance in parallel with the reactor;

L : Current rate limiting inductance ;

C_P : Thyristor parasitic capacitance;

C_S : Snubber capacitance; and

L_C : Circulating-current reactance.

Since the three-phase, six-pulse cycloconverter is a complex system with several physical components as shown in Figure 5.12, each component is modeled and merged to form an entire system. Thus, the QMQI method is applied to each component and Newton's method is applied after merging all components. Since the modeling process is presented in our previous research of [35], [36], and [37], as well as in Chapter 3, the state equations of a single-phase transformer and a circulating-current reactor are only presented in this subsection. Note that the time-domain model of the three-phase isolation transformers is formed by the proper combinations of three single-phase transformers, as shown in Figure 5.13. Also, since the state equations of the electrical valve (thyristor) are presented in Chapter 5.2, the model of the electrical valve is omitted in this subsection.

The three-phase isolation transformers are used for electrical isolation of each individual six-pulse bridge, since the three-phase, six-pulse cycloconverter does not have any common connected points between the input and output [28].

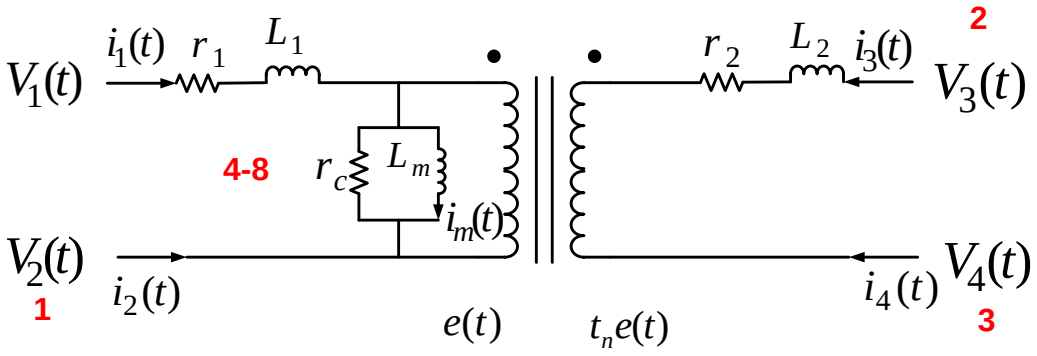

Figure 5.13: An equivalent circuit of a single-phase transformer.

The single-phase transformer consists of winding resistance (r_1 and r_2), leakage reactance (L_1 and L_2), core loss (r_C), and magnetizing reactance (L_m), as shown in Figure 5.13.

Using the parameters, the state equations are written as a set of algebraic equations and differential equations as follows:

$$i_1(t) = i_{1L}(t) \tag{5.3.1}$$

$$i_2(t) = -i_{1L}(t) \tag{5.3.2}$$

$$i_3(t) = i_{3L}(t) \tag{5.3.3}$$

$$i_4(t) = -i_{3L}(t) \tag{5.3.4}$$

$$0 = -r_c i_{1L}(t) - r_c t\, i_{3L}(t) + r_c i_m(t) + e(t) \tag{5.3.5}$$

$$0 = L_m i_m(t) - \lambda(t) \tag{5.3.6}$$

$$0 = v_1(t) - v_2(t) - e(t) - r_1 i_{1L}(t) - L_1 \frac{d}{dt} i_{1L}(t) \tag{5.3.7}$$

$$0 = v_3(t) - v_4(t) - t\, e(t) - r_2 i_{3L}(t) - L_2 \frac{d}{dt} i_{3L}(t) \tag{5.3.8}$$

$$0 = e(t) - \frac{d}{dt} \lambda(t) \tag{5.3.9}$$

The discontinuous transactions between the positive and negative converter (bank) generate abnormal distortions of output-voltages. Here, circulating current circuits are introduced to avoid voltage distortions from discontinuous transactions, since the circulating current circuits should support continuous conduction of both converters. Also, the circulating current circuits can support both a full circulating current mode and a partial circulating current mode in which the electrical loss can be reduced compared to the full circulating current model. Figure 4 shows the equivalent circuit of the circulating current circuit.

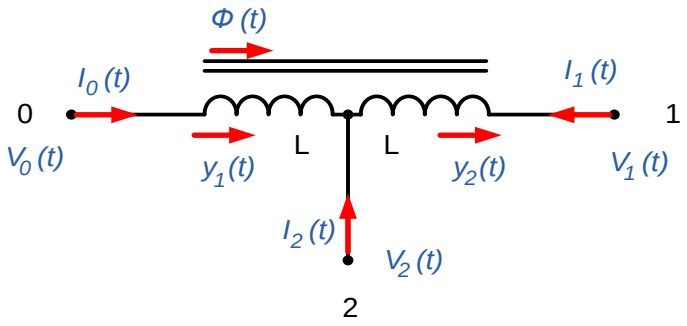

Figure 5.14: An equivalent circuit of a circulating-current circuit

The state equations for the circulating current circuit can also be denoted by a set of algebraic equations and differential equations. The model equations are:

$$i_0(t) = y_1(t) \tag{5.3.10}$$

$$i_1(t) = -y_2(t) \tag{5.3.11}$$

$$i_2(t) = -y_1(t) + y_2(t) \tag{5.3.12}$$

$$0 = N_1 y_1(t) + N_2 y_2(t) - \Re\phi(t) \tag{5.3.13}$$

$$0 = v_0(t) - v_2(t) - \frac{dN_1\phi(t)}{dt} + L_l \frac{d}{dt} y_1(t) \tag{5.3.14}$$

$$0 = v_2(t) - v_1(t) - \frac{dN_2\phi(t)}{dt} + L_l \frac{d}{dt} y_2(t) \tag{5.3.15}$$

Note that L_l is the leakage inductance of the circulating current circuit, and N_1 and N_2 are coil-turns.

5.3.2 Control Algorithm: Cosine Wave-Crossing Method

The basic control principle of the three-phase, six-pulse cycloconverter is to continuously modulate the firing angles of the individual converters (positive and negative converters), according to its control algorithms. Here, the cosine wave-crossing

method with the partial circulating current mode is selected for its switching sequences, since the proposed control algorithm has demonstrated the following properties:

- Partial circulating current mode
  - The partial circulating current mode can prevent discontinuous operations during bank-exchange operations from the positive to negative bank, or conversely, with minimal circulating loss;
  - Distortion of output-currents can be eliminated in this mode.
- Cosine wave-crossing controller
  - Firing pulses are generated by the crossing points of both wanted and threshold voltages of reference voltages;
  - This method demonstrates superior properties, such as minimum total harmonic distortion of output-voltages, and simplicity of implementation.

The control action for the three-phase, six-pulse cycloconverter can modulate the frequency, magnitude, and phase angle of output-voltages. The operating-frequency level in this work is limited to 20-Hz, since frequencies higher than 20Hz can cause high THD (Total Harmonic Distortion). The voltage level and phase angle are also controlled by the application of the cosine wave-crossing method, since electrical power (capacity) can be regulated by the voltage level and phase angle.

The control action is based on the references (zero-crossing time, magnitude, and phase angle of the estimated voltages) from the DSP (Digital Signal Processor); thus, switching sequences are generated for positive and negative converters using the references from the DSP. Note that the DSP model is omitted, since the model is already

presented in Chapter 5.2. The entire control algorithm is presented in Figure 5.15, and the control action is explained in steps as follows:

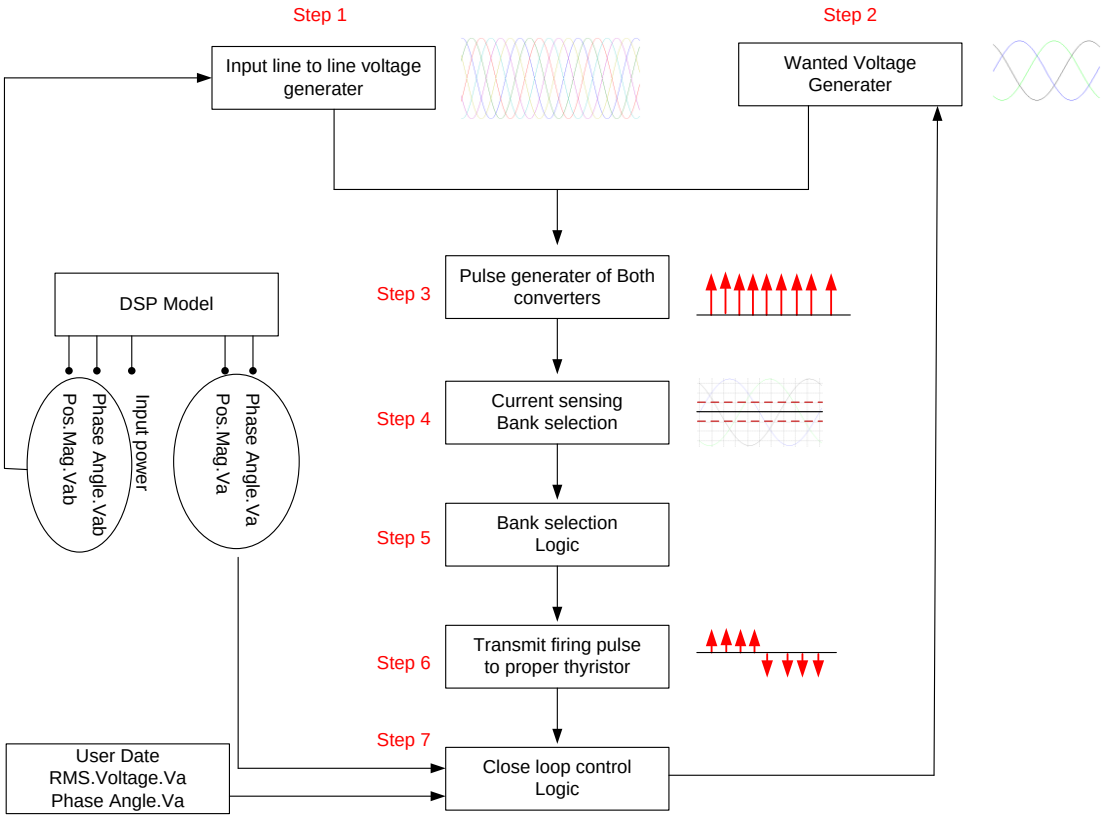

Figure 5.15: Entire control scheme of the cycloconverter.

Step 1: To generate line-to-line voltage at the high-frequency side.

From the DSP, the magnitude (V_{ab1}) and phase angle (θ_{iab}) of $V_{ab1}(t)$ are estimated. Therefore, three-phase, line-to-line voltages at the high-frequency side are estimated, based on the magnitude and phase angle of $V_{ab}(t)$as follows:

$$V_{ab}(t) = V_{ab1}\cos(w_i t + \theta_{iab}) \tag{5.3.16}$$

$$V_{ac}(t) = V_{ac1}\cos(w_i t + \theta_{iab} - 60^o) \tag{5.3.17}$$

$$V_{bc}(t) = V_{ac1}\cos(w_i t + \theta_{iab} - 120^o) \tag{5.3.18}$$

$$V_{ba}(t) = V_{ac1}\cos(w_i t + \theta_{iab} - 180^o) \tag{5.3.19}$$

$$V_{ca}(t) = V_{ac1}\cos(w_i t + \theta_{iab} - 240^o) \quad (5.3.20)$$

$$V_{cb}(t) = V_{ac1}\cos(w_i t + \theta_{iab} - 300^o) \quad (5.3.21)$$

Step 2: To generate wanted output-voltages.

Wanted output-voltages are computed by user given values of $V_r \angle \theta_r$ and positive sequence fundamental output-voltage from the DSP model. The detailed explanation is given in Step 7.

$$V_{wa}(t) = V_{wa}\cos(w_o t + \theta_o) \quad (5.3.22)$$

$$V_{wb}(t) = V_{wa}\cos(w_o t + \theta_o - 120^o) \quad (5.3.23)$$

$$V_{wc}(t) = V_{wa}\cos(w_o t + \theta_o - 240^o) \quad (5.3.24)$$

where V_{wa} is the wanted output-voltage of *Phase A*, w_0 is $2\pi f_o$, f_o is frequency of the output-voltage, and θ_o is the phase angle of *Phase A*.

Step 3: To generate switching pulses of both converters.

Firing pulses are generated by comparing V_T with V_w, as in the algorithm below. The threshold voltage (V_T) is generated by the average value of adjacent input-voltages. For example, assuming that V_{ab} and V_{ac} are the adjacent input voltages, $V_T(t) = \frac{V_{ab}(t) + V_{ac}(t)}{2}$. Therefore, the firing pulses are generated at the point, $V_T(t)=V_w(t)$, as in Figure 5.16.

Positive

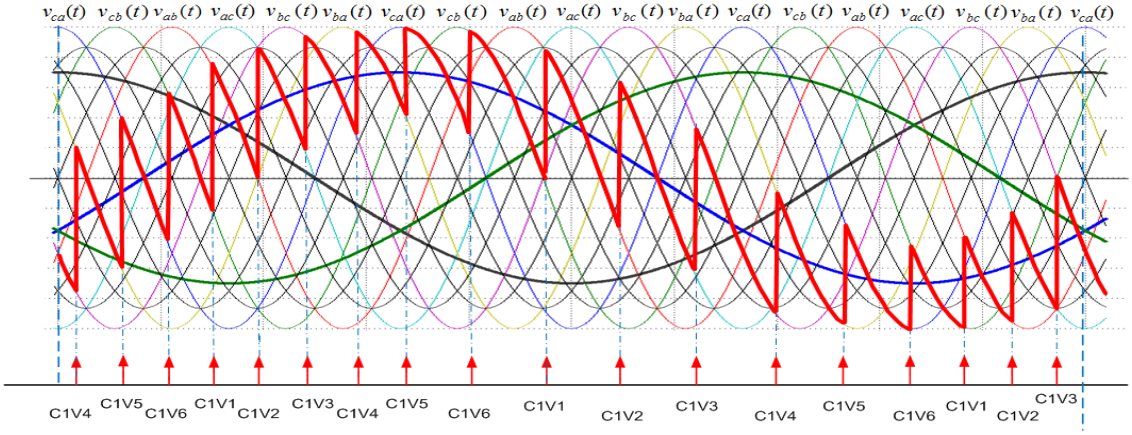

Negative

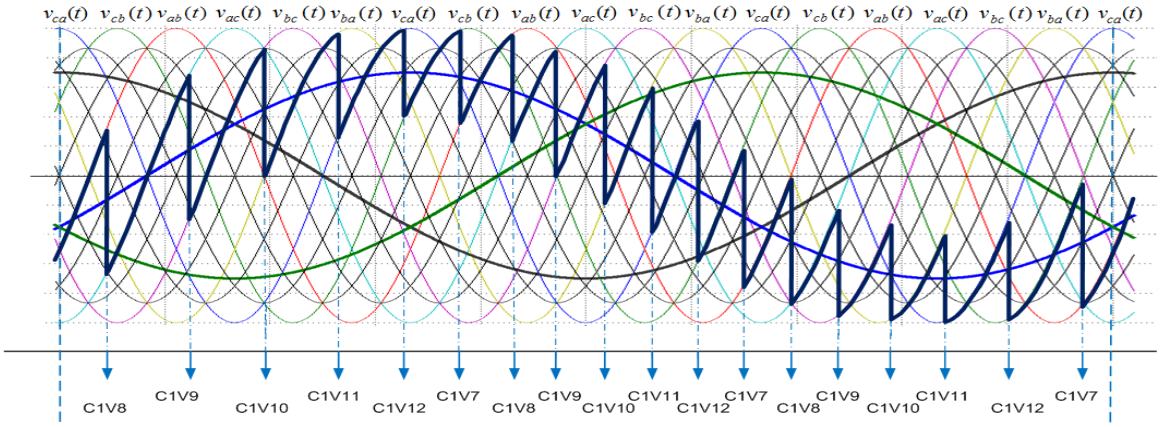

Figure 5.16: The scheme of pulse generation for both converters

Step 5: To check the magnitude of the output-current and select the proper banks.

To fulfill the cosine wave-crossing method with partial circulating current mode, the output-currents have to be measured at every time-step. The magnitude of the output-currents is used to select either the positive or negative bank. Assuming that the output-current is bigger than $-I_T$, the positive bank is active; assuming that the output-current is smaller than I_T, the negative bank is active. Figure 5.17 shows an example of bank selection(s) according to $i_{oa}(t)$. Note that $i_{oa}(t)$ is the output-current of phase A.

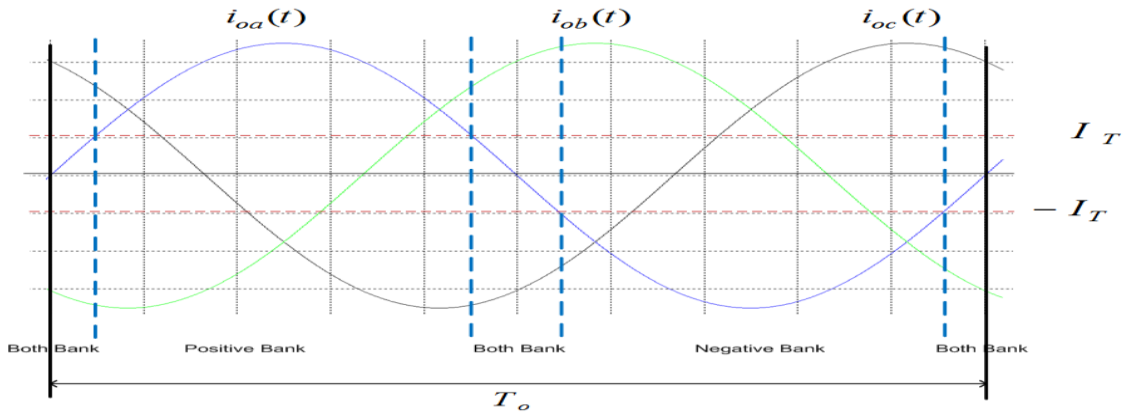

Figure 5.17: The explanation of bank selection (i_{oa}, i_{ob}, and i_{oc} are a three-phase output-current).

Step 6: To transmit firing pulses to Proper Thyristors.

Assuming that the positive bank is activated, pulse signals are transmitted to the positive converter, and assuming that the negative bank is activated, pulse signals are transmitted to the negative converter. Note that since the switches are thyristor valves, there is no control algorithm for off-state conditions. Figure 5.18 shows the theoretical output-voltage by the application of the cosine wave-crossing method with the partial circulating current mode.

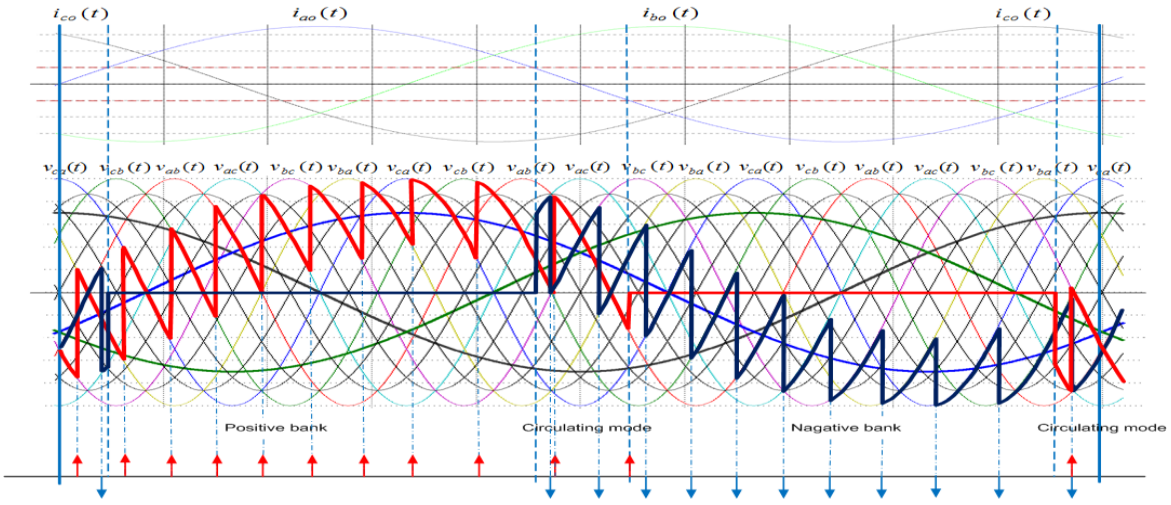

Figure 5.18: Firing-pulse transmission in the proper manner.

Step 7: To perform close-loop control.

The closed-loop controller regulates the magnitude and phase angle of output-voltage by manipulating the wanted output-voltages. The magnitude and phase angle, which are estimated by the DSP model, are compared to the magnitude and phase angle of the reference voltage. Therefore, the mismatched values between the wanted output-voltages and output-voltages from the DSP are continuously regulated to meet the reference values. Note that the magnitude of the output-voltages is inherently bigger than those of the wanted voltages in the application of the cosine wave-crossing method; thus, closed-loop control is needed to regulate the exact magnitude of the output-voltage. Figure 5.19 shows a block diagram for controlling the magnitude of the output-voltages.

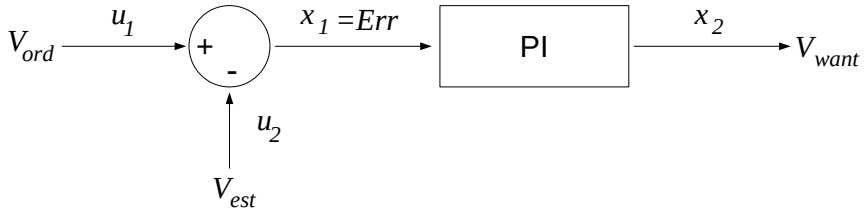

Figure 5.19: Block diagram to control the magnitude of the output-voltages.

The equations to control the magnitude of the output-voltage are as follows:

$$x_1(t) = u_1(t) - u_2(t) \tag{5.3.25}$$

$$x_2(t) = k_p x_1(t) + k_I \int x_1(t) \tag{5.3.26}$$

where $u = \begin{bmatrix} u_1 & u_2 \end{bmatrix}^T = \begin{bmatrix} V_{ord} & V_{est} \end{bmatrix}^T$, and $x = \begin{bmatrix} x_1 & x_2 \end{bmatrix}^T = \begin{bmatrix} Err & V_{want} \end{bmatrix}^T$.

The algebraic-companion form via the application of quadratic integration to the control equations is as follows: (5.3.27)

$$\begin{bmatrix} 1 & 0 & 0 & 0 \\ k_p+\frac{h}{6} & -1 & \frac{2h}{3} & 0 \\ 0 & 0 & 1 & 0 \\ -\frac{h}{24} & 0 & k_p+\frac{h}{3} & -1 \end{bmatrix}\begin{bmatrix} x_1(t) \\ x_2(t) \\ x_1(t_m) \\ x_2(t_m) \end{bmatrix}=\begin{bmatrix} 0 & 0 \\ k_p-\frac{h}{6} & -1 \\ 0 & 0 \\ k_p-\frac{5h}{24} & -1 \end{bmatrix}\begin{bmatrix} x_1(t-h) \\ x_2(t-h) \end{bmatrix}+\begin{bmatrix} 1 & -1 & 0 & 0 \\ 0 & 0 & 0 & 0 \\ 0 & 0 & 1 & -1 \\ 0 & 0 & 0 & 0 \end{bmatrix}\begin{bmatrix} u_1(t) \\ u_2(t) \\ u_1(t_m) \\ u_2(t_m) \end{bmatrix}$$

Phase angles of the output-voltages also have to be controlled for to meet the power-order, since the real power depends on the differences between the voltage angles of the sending bus and the receiving bus. The block diagram to control the phase angle of the output-voltage is shown in Figure 5.20.

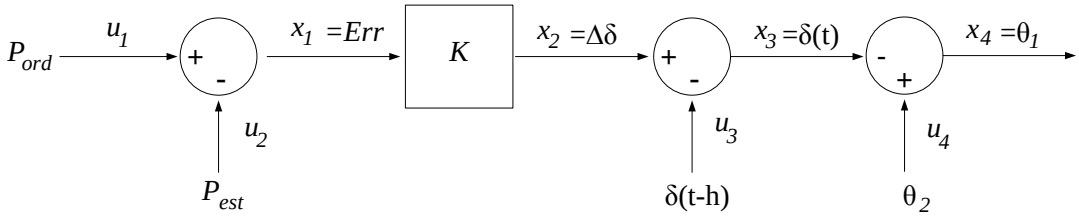

Figure 5.20: Block diagram to control the angle of the output-voltages.

The relationship between real power and the power angle is as follows:

$$p = \frac{V_1 \cdot V_2}{X}\sin\delta \tag{5.3.28}$$

Obviously the power and power angle do not have a linear relationship. However, power deviation is regulated linearly by the deviation of the power angle.

$$\Delta P = \frac{V_1 \cdot V_2}{X}\cos\delta \cdot \Delta\delta \qquad \text{where } \Delta P = P_{ord} - P_{est} \tag{5.3.29}$$

$$\Delta P = K \cdot \Delta\delta \qquad \text{where } K = \frac{V_1 \cdot V_2}{X}\cos\delta \tag{5.3.30}$$

$$\delta(t) = \delta(t-h) + \Delta\delta \tag{5.3.31}$$

$$\theta_1(t) = \theta_2(t) - \delta(t) \tag{5.3.32}$$

The control equation is presented as follows.

$$x_1(t) = u_1(t) - u_2(t) \tag{5.3.33}$$

$$K \cdot x_1(t) - x_2(t) = 0 \tag{5.3.34}$$

$$-x_2(t) + x_3(t) = -u_3(t) \tag{5.3.35}$$

$$x_3(t) + x_4(t) = u_4(t) \tag{5.3.36}$$

The compact matrix form of the equations is denoted as follows:

$$\begin{bmatrix} x_1(t) \\ x_2(t) \\ x_3(t) \\ x_4(t) \end{bmatrix} = \begin{bmatrix} 1 & 0 & 0 & 0 \\ K & -1 & 0 & 0 \\ 0 & -1 & 1 & 0 \\ 0 & 0 & 1 & 1 \end{bmatrix}^{-1} \cdot \begin{bmatrix} 1 & -1 & 0 & 0 \\ 0 & 0 & 0 & 0 \\ 0 & 0 & 1 & 0 \\ 0 & 0 & 0 & 1 \end{bmatrix} \begin{bmatrix} u_1(t) \\ u_2(t) \\ u_3(t) \\ u_4(t) \end{bmatrix} \tag{5.3.37}$$

5.4 A Three-Phase PWM Converter

The modeling methodology for the three-phase, pulse-width-modulation (PWM) converter is presented in this subsection. The three-phase, PWM converter is widely used for the integration of renewable resources, since phase-controlled converters using thyristors are impractical for weak synchronous systems and induction machines for wind farms. Also, the three-phase PWM converters have demonstrated several superior properties, such as (a) bi-directional power-flow control, (b) low-harmonic distortion of AC-line currents, and (c) flexible reactive power control [38]. The purpose of converters is to support maximum power capturing from wind turbine systems and to offer constant output-voltage frequency from variable-speed wind [38]. For the control algorithm, the direct-power control algorithm (DPC) is utilized, since the control algorithm has demonstrated some outstanding characteristics, including: a simple algorithm, a superior dynamic response, and steady-state performance [41].

5.4.1 Equivalent Circuit of a Three-Phase, PWM Converter

The three-phase PWM converter consists of six electrical valves (IGBTs) and a smoothing capacitor, as shown in Figure 5.21. Furthermore, controllers are needed to generate switching sequences for on/off-controllable switches of the three-phase PWM converter. The controllers are based on a direct-power control algorithm using space vectors, since the controllers have demonstrated a rapid dynamic response with a simple structure [40].

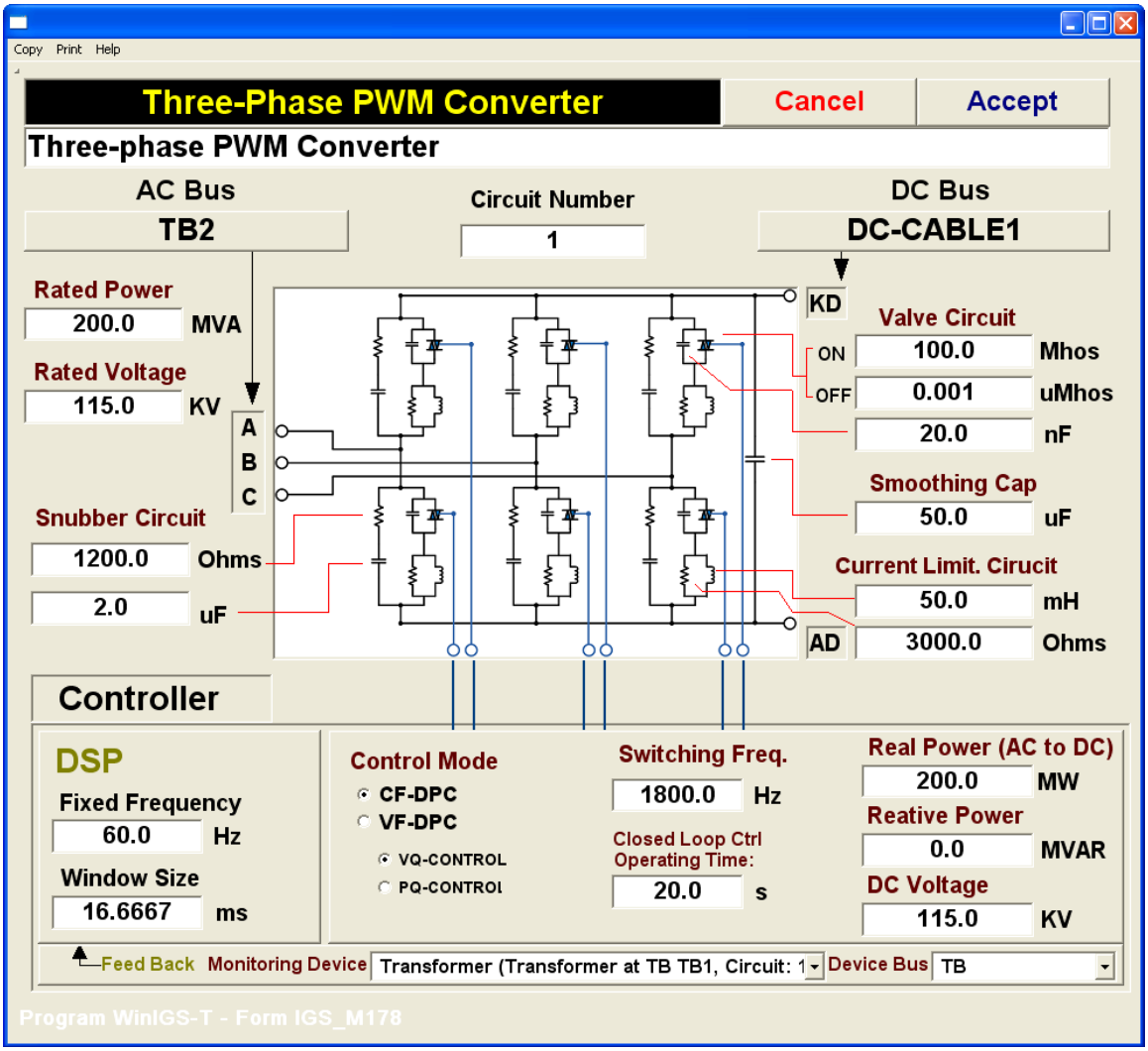

Figure 5.21: Input-data form of the three-phase PWM converter.

The models of the electrical-valves and the smoothing capacitor in the three-phase PWM converter are the same as those in the three-phase, six-pulse converter in Chapter 5.2, except that the electrical switches are on/off-controllable switches. Even though the physical structure of the electrical valves in the three-phase PWM converter is different from those of the electrical valves in the three-phase, six-pulse converter, the mathematical equations for the valve are equivalent to each other. Thus, the mathematical models of the three-phase PWM converter are omitted in this subsection.

5.4.2 Control Algorithm: Direct-Power-Control Algorithm

The direct-power control (DPC) algorithm is used to control the three-phase PWM converters, since the control algorithm has demonstrated some outstanding properties, including the following advantages: a simple algorithm, a superior dynamic response, and steady-state performance [41]. The DPC algorithm is modeled for both (1) constant frequency applications and (2) variable frequency applications. Generally, the three-phase PWM converter with a control algorithm in constant operating frequency (for brevity, the control algorithm is denoted as a constant frequency control algorithm), which is referred to a grid-side converter (GSC), is directly connected to the grid systems, and the GSC supports constant DC-voltage and reactive power controllability for grid-connected systems. Otherwise, the PWM converter with the control algorithm in variable operating frequency (for brevity, the control algorithm is denoted as the variable frequency control algorithm), which is referred to the machine-side converter (MSC), is directly connected to the wind turbines, and the MSC supports maximum power capturing from the wind-turbine systems and the reactive power controllability to them. Note that the MSC is directly connected to the rotor of a doubly fed induction generator

(DFIG) in Type-3 wind-generation units, and the stator of a permanent magnet synchronous generator (PMSG) in Type-4 wind-generation units. Since the control algorithms of the three-phase PWM converter are very diverse, according to the control purpose and controlled devices, all cannot be considered in this subsection. Thus, two general control algorithms are only presented for both a constant frequency controller and a variable frequency controller as shown in Figure 5.22 and Figure 5.23. Note that the constant frequency controller is only presented since the DPC algorithms for the Type-4 wind-generation unit are easily found in previous research from [39]to [43].

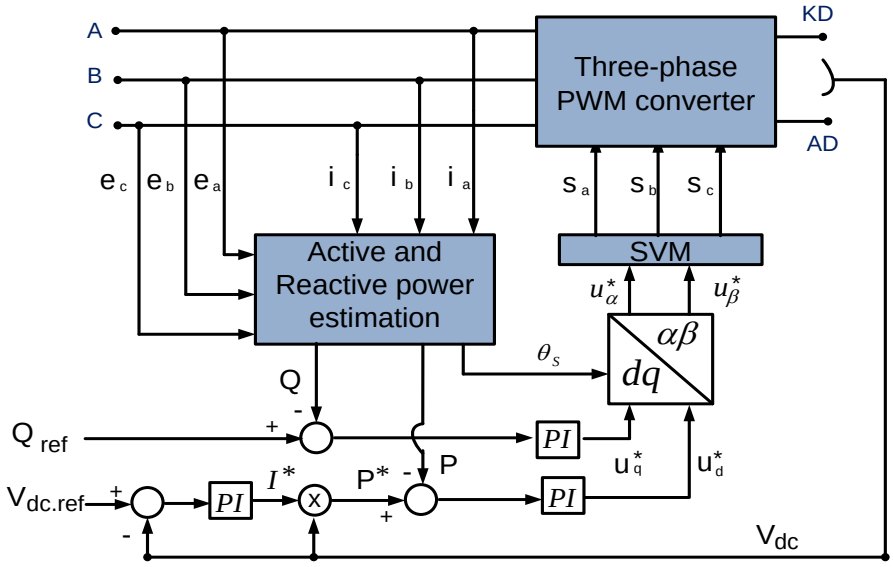

Figure 5.22: A constant frequency controller using direct-power algorithm with space-vector modulation.

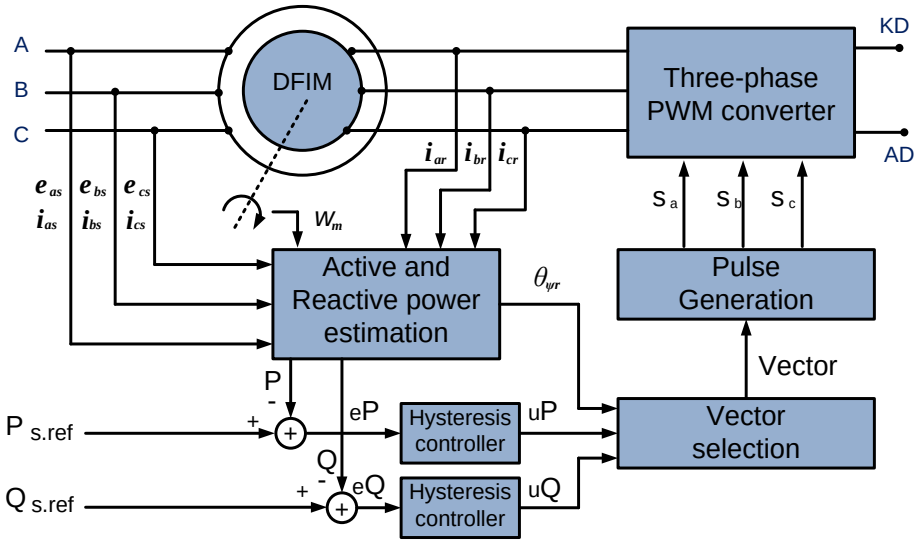

Figure 5.23: A variable frequency controller using the direct-power algorithm with hysteresis controllers.

Figure 5.22 shows a constant frequency control algorithm, which is based on a direct-power control algorithm with a space-vector modulation (DPC-SVM). The control algorithm is modeled, based on three steps as follows:

Step 1: To estimate active- and reactive-power and synchronous-position angle.

Active- and reactive-power and the synchronous position angle are estimated with the DSP model, as shown in Figure 5.5. The powers are easily computed using positive sequence fundamental voltages and positive sequence fundamental currents from the DSP model, as follows:

$$P = \frac{3}{2} V_{a1} I_{a1} \cos\left(\phi_{v_{a1}} - \phi_{i_{a1}}\right) \tag{5.4.1}$$

$$Q = \frac{3}{2} V_{a1} I_{a1} \sin\left(\phi_{v_{a1}} - \phi_{i_{a1}}\right) \tag{5.4.2}$$

To find the synchronous position angle, the voltages in $\alpha\beta$-coordination are calculated while the *Clarke direct transformation* is applied to the positive sequence fundamental voltages as follows:

$$\begin{bmatrix} v_\alpha \\ v_\beta \end{bmatrix} = \frac{2}{3} \cdot \begin{bmatrix} 1 & -\frac{1}{2} & -\frac{1}{2} \\ 0 & \frac{\sqrt{3}}{2} & -\frac{\sqrt{3}}{2} \end{bmatrix} \cdot \begin{bmatrix} V_{a1} \\ V_{b1} \\ V_{c1} \end{bmatrix} \tag{5.4.3}$$

Using the v_α and v_β from Equation (5.4.3), the synchronous angle-position (θ_s) is computed as follows:

$$\theta_s = atan\left(\frac{v_\beta}{v_\alpha}\right) \tag{5.4.4}$$

Step 2: To estimate voltage references in $\alpha\beta$-coordination.

The reference voltages in $\alpha\beta$-coordination are computed based on the DPC algorithm. In the DPC algorithm, the errors between the estimated references (real-time DC-voltage, powers, and the synchronous position angle) and prospective references (power order and DC-voltage order) are collected and manipulated, using three PI controllers to compute the reference voltages in $\alpha\beta$-coordination. Figure 5.24 is the entire block diagram of the DPC algorithm. The block diagram of the DPC algorithm can be represented as state-space equations.

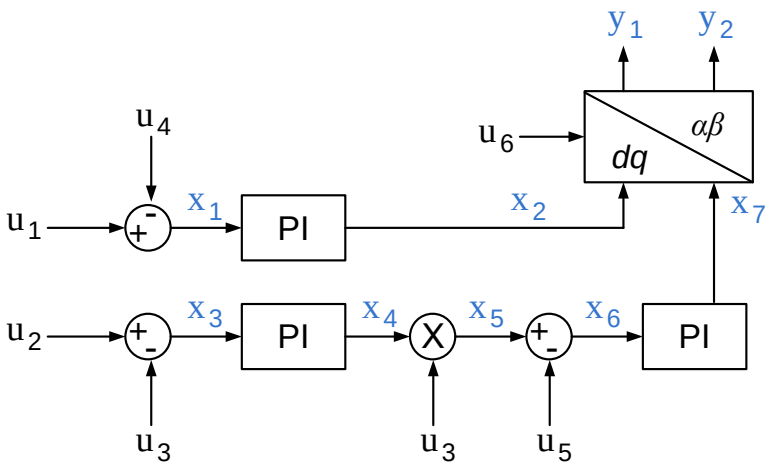

Figure 5.24: Block Diagram of the DPC Control Algorithm

The vectors of *U* and *X* are a set of the inputs and states in the DPC, and the vectors are denoted in mathematic representation as follows:

$$U=\left[u_1\ \ u_2\ \ u_3\ \ u_4\ \ u_5\ \ u_6\right]^T=\left[Q_{ref}\ \ V_{dc.ref}\ \ V_{dc}\ \ Q\ \ P\ \ \theta_s\right]^T$$

$$X=\left[x_1\ \ x_2\ \ x_3\ \ x_4\ \ x_5\ \ x_6\ \ x_7\right]^T=\left[Q_{ref}-Q\ \ U_q^*\ \ V_{dc.ref}-V_{dc}\ \ I^*\ \ P^*\ \ P^x-P\ \ U_d^*\right]^T$$

The state-space equations of the DPC are as follows:

$$0=x_1(t)-u_1(t)+u_4(t) \tag{5.4.5}$$

$$-k_{p1}\cdot\dot{x}_1(t)+\dot{x}_2(t)=k_{I1}\cdot x_1(t) \tag{5.4.6}$$

$$0=x_3(t)-u_2(t)+u_3(t) \tag{5.4.7}$$

$$-k_{p2}\cdot\dot{x}_3(t)+\dot{x}_4(t)=k_{I2}\cdot x_3(t) \tag{5.4.8}$$

$$0=u_3(t)x_4(t)-x_5(t) \tag{5.4.9}$$

$$0 = x_5(t) - x_6(t) - u_5(t) \tag{5.4.10}$$

$$-k_{p3} \cdot \dot{x}_6(t) + \dot{x}_7(t) = k_{I3} \cdot x_6(t) \tag{5.4.11}$$

The state-space equations of the DPC algorithm are represented in a compact matrix form as follows:

$$A \cdot \dot{X} = B \cdot X + C \cdot U \tag{5.4.12}$$

where:

$$A = \begin{bmatrix} 0 & 0 & 0 & 0 & 0 & 0 & 0 \\ -k_{p1} & 1 & 0 & 0 & 0 & 0 & 0 \\ 0 & 0 & 0 & 0 & 0 & 0 & 0 \\ 0 & 0 & -k_{p2} & 1 & 0 & 0 & 0 \\ 0 & 0 & 0 & 0 & 0 & 0 & 0 \\ 0 & 0 & 0 & 0 & 0 & 0 & 0 \\ 0 & 0 & 0 & 0 & 0 & -k_{p3} & 1 \end{bmatrix}, B = \begin{bmatrix} 1 & 0 & 0 & 0 & 0 & 0 & 0 \\ k_{I1} & 0 & 0 & 0 & 0 & 0 & 0 \\ 0 & 0 & 1 & 0 & 0 & 0 & 0 \\ 0 & 0 & k_{I2} & 0 & 0 & 0 & 0 \\ 0 & 0 & 0 & u_3(t) & -1 & 0 & 0 \\ 0 & 0 & 0 & 0 & 1 & -1 & 0 \\ 0 & 0 & 0 & 0 & 0 & k_{I3} & 0 \end{bmatrix}, \text{ and}$$

$$C = \begin{bmatrix} -1 & 0 & 0 & 1 & 0 & 0 \\ 0 & 0 & 0 & 0 & 0 & 0 \\ 0 & -1 & 1 & 0 & 0 & 0 \\ 0 & 0 & 0 & 0 & 0 & 0 \\ 0 & 0 & 0 & 0 & 0 & 0 \\ 0 & 0 & 0 & 0 & -1 & 0 \\ 0 & 0 & 0 & 0 & 0 & 0 \end{bmatrix}.$$

Note that k_{pj} and k_{Ij} are constant coefficients for PI controllers, and j represents integer numbers from 1 to 3.

Since the state-space equations are written as differential and algebraic equations, the quadratic-integration method is applied to convert the state-space equations into an algebraic companion form as the previous algebraic models of the physical components in converters. In the algebraic equations, the voltages of u_q^* and u_d^* in *dq*-coordination are

denoted as x_2 and x_7, and the voltages are transformed into reference voltages in $\alpha\beta$-coordination as follows:

$$\begin{bmatrix} u_\alpha^* \\ u_\beta^* \end{bmatrix} = \begin{bmatrix} \cos u_6 & -\sin u_6 \\ \sin u_6 & \cos u_6 \end{bmatrix} \begin{bmatrix} x_7 \\ x_2 \end{bmatrix} \tag{5.4.13}$$

Step 3: To estimate the switching sequence from the SVM-algorithm.

The SVM-diagram shown in Figure 5.25 is used to calculate the switching sequence and switching interval of on/off-states. The SVM is popularly used as one of the digital control algorithms for the three-phase PWM converter connected to the constant frequency systems.

The switching sequence and switching intervals are decided, according to the reference voltages in $\alpha\beta$-coordination. For this purpose, the reference voltages are written in polar form as follows:

$$\vec{v}_{svm,ref} = \left|V_{svm.ref}\right| \angle \theta_\alpha \tag{5.4.14}$$

where $\left|V_{svm.ref}\right| = \sqrt{(u_\alpha^*)^2 + (u_\beta^*)^2}$ and $\theta_\alpha = arctan\left(\frac{u_\beta^*}{u_\alpha^*}\right)$.

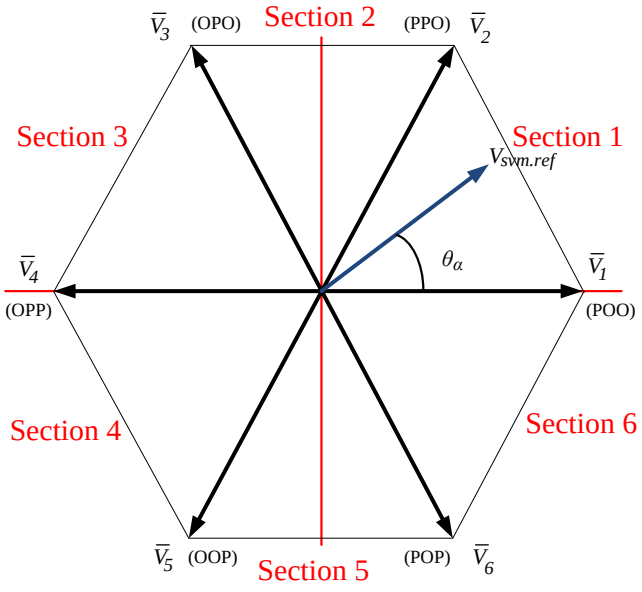

Figure 5.25: A diagram for space-vector modulation

The dwelling time (pulse-width) that denotes the switching interval of on/off-states is calculated by using the *volt-second-balancing* principle as follows.

$$T_a = T_S m_a \sin\left(\frac{\pi}{3} - \theta\right), \tag{5.4.15}$$

$$T_b = T_S m_a \sin\theta), \text{ and} \tag{5.4.16}$$

$$T_0 = T_S - T_a - T_b \tag{5.4.17}$$

where: $m_a = \dfrac{\sqrt{3}V_{ref}}{V_{dc}}$, $\theta = \theta_\alpha - (n-1)\dfrac{\pi}{3}$, and n is the section number in the SVM diagram.

Note T_a, T_b, and T_c are the dwelling times (switching intervals) of each phase of *phase A*, *phase B*, and *phase C*, respectively, and the modulation index m_a exists in the range of $0 \le m_a \le 1$. As soon as the dwelling times are computed, the switching sequence is

arranged for the three legs: The switching sequence is based on a *seven–segment* arrangement with switching patterns for *even-order-harmonics* elimination, as shown in Figure 5.26. The switching sequence is selected for the following requirements [44]:

- Only two switches in the same leg have to be involved during the transition from one-state to another.
- None or a minimum number of switching is required during the transition from one section to another in the SVM diagram.

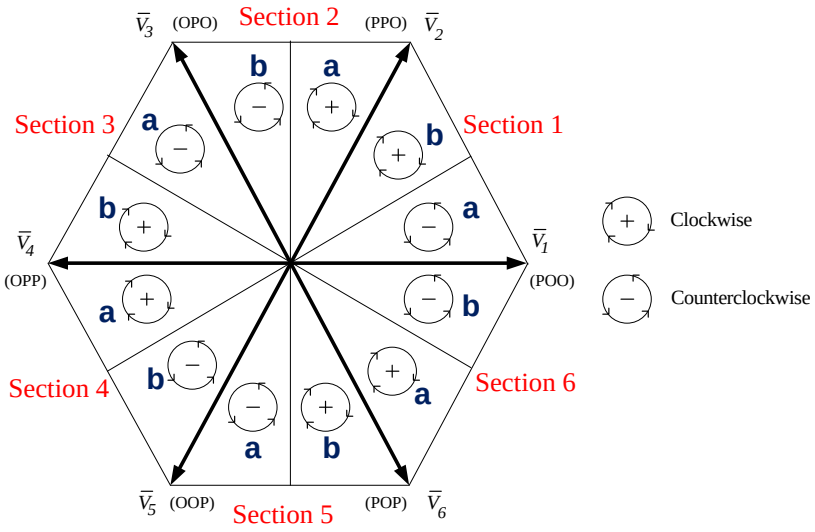

Figure 5.26: Mirror image in the SVM diagram.

Elimination of even-order harmonics can be accomplished while waveforms are arranged in half-wave symmetry. For this purpose, two regions facing each other in the SVM diagram can be arranged in a mirror image as shown in Figure 5.26 and the line-t-line voltages at the AC-side become half-wave symmetrical forms. Note that the switching sequences rotate clockwise or counterclockwise to achieve the mirror image.

5.5 Summary

This section presents time-domain models of converters: a three-phase, six-pulse converter, a three-phase, six-pulse cycloconverter, and a three-phase PWM converter. These models are based on model quadratization and quadratic integration, leading to reliable and accurate models. These converters are controlled by using a specific control algorithm according to their purposes.

The converter models in the time-domain help to conduct accurate analyses of alternative transmission systems, such as harmonics analyses, power-transient analyses, switching performance analyses, etc.

CHAPTER 6

DEMONSTRATIVE EXAMPLES

6.1 Introduction

In this section, demonstrative examples of alternative transmission systems are presented and studied, using reliable models in the frequency-domain, quasi steady-state, and time-domain. First, in the frequency-domain models, averaging converter models are used for operational studies of LFAC-transmission systems interconnecting wind-farm systems and synchronous grid systems. The next involves transient-stability studies, using averaging converter models in quasi steady-states. In these studies, the voltage ride through (VRT) capability of wind farm systems, using LFAC-transmission systems, is analyzed. The last concern time-domain studies using time-domain models of converters. In these studies, power transient studies and harmonics studies are performed using example configurations of wind farm systems. Note that more detailed studies and knowledge of the LFAC-transmission system are shown in [14], since this chapter is a partial fulfillment of the technical research supported by PESEC (the Power Systems Engineering Research Center)

6.2 Operational Study in Steady-State

In this study, the maximum power transfer capability (MPTC) of alternative transmission systems using LFAC-transmission systems, in which the operational frequency is 20-Hz, is compared to that of nominal frequency (60-Hz) transmission

systems. LFAC-transmission systems use the averaging models of a three-phase, PWM converter and a three-phase, six-pulse cycloconverter, since the power transfer capability is a quantitative analysis. In the quantitative analysis of power transfer capability, the ability of electrical power systems to transfer electrical power from one to another place is analyzed in the operational constraints of physical and electrical limitations that assure robust and secure operation of the power systems. For the power-transfer capability studies of LFAC-transmission systems, several constraints are considered, such as the operational margins of converters (cycloconverters and PWM converters) and voltage-drop margins on AC transmission lines interconnecting a common connection point (PCC) of wind farm systems and a synchronous grid system.

Note that the limitation of power transfer capability is decided as the maximum quantity of power-transfer capability under the most restrictive among several constraints.

6.2.1 Technical Approach of Power Transfer Capability Study

The studies of power transfer capability are comparative studies between two transmission systems interconnecting a PCC of wind farm systems and a synchronous grid. For this purpose, two different transmission systems are introduced, as shown in Figure 6.1: Type-1 is a typical transmission system to transfer 60-Hz electrical power, while Type-2 is one of the LFAC-transmission systems using a PWM converter and a cycloconverter. Type-1 is a simple configuration using a three-phase, overhead transmission line and a three-phase, step-up transformer. Type-2 seems like a combined configuration of the typical transmission system of type-1 and the converters of a PWM inverter and a cycloconverter.

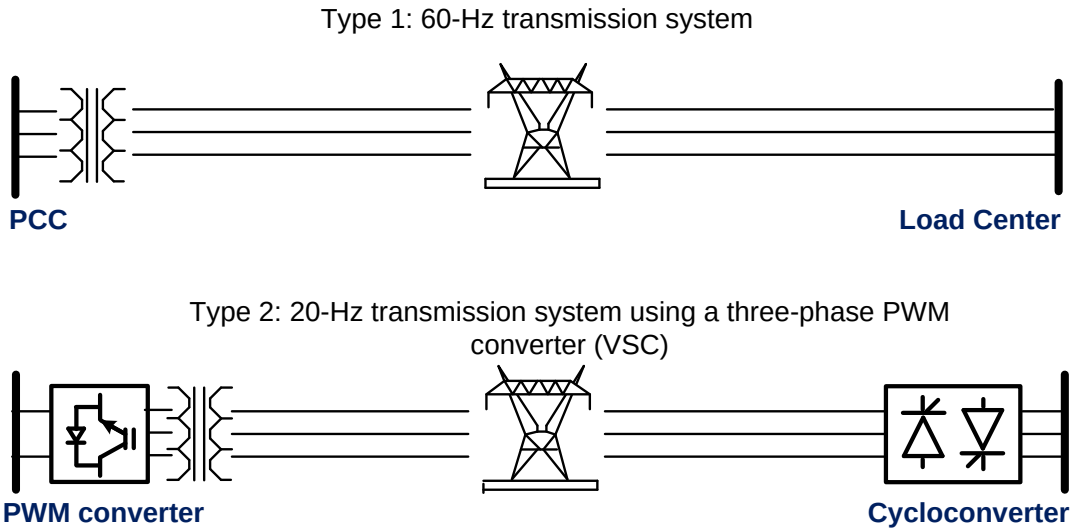

Figure 6.1: Two Types of Transmission Configurations for Case Studies.

Since the MPTC study is a quantitative analysis, the frequency-domain models of the three-phase transmission lines and three-phase transformers are needed, as well as the averaging models of a three-phase, six-pulse cycloconverter and a three-phase PWM inverter. The overhead transmission line and the three-phase transformer should have the ability to support different frequency operations, since the models are used for a 60-Hz system (Type-1) and a 20-Hz system (Type-2). The three-phase cycloconverter allows the interconnection between the LFAC-transmission system and a grid system, as well as the controllability of the AC-voltage level at the LFAC-transmission system. The three-phase PWM inverter permits the possibility to control the DC voltage level and reactive power level in the LFAC-transmission system. Also, the AC voltage level of the PWM inverter is automatically synchronized to the voltage level derived from the cycloconverter.

For the MPTC study, the physical and electrical constraints are considered such as the AC-voltage and the DC-voltage limit at transmission lines, and the modulation-index limits of converters. The mathematical representation is written as follows:

MPTC = minimum{AC-voltage limit, DC-voltage limit, modulation index limits, etc.}

The maximum power transfer capability is the maximum power that satisfies all of the constraints. That is, the maximum power-transfer capability is decided under the most restrictive among the three constraints [45].

6.2.2 Case Studies of Power Transfer Capability

The studies of the maximum power transfer capability are based on a quantitative analysis using computer models. The quantity of maximum power transfer capability is a scalar parameter, which can vary in the system configurations. The amount of transfer is gradually increased from the minimum to the maximum quantity of transfer power under operational constraints, and the maximum quantity is recorded, according to distances [14]. The quantity of the maximum power transfer capability varies according to the operating voltage, the operating frequency, and the transmission distances in the test configuration, as shown in Figure 6.1. The MPTC should be recorded according to the variation of the three parameters.

Since the variations of the operational frequency, voltage, and distance are boundless, only some cases among the variations are considered in these operational studies: the operational voltages of 38-kV, 76-kV, and 115-kV, operational frequencies of 20-Hz and 60-Hz, and the distances from 0 to 200 miles. Note that the operating

voltages are selected at 1/3 of the nominal voltages of 115-kV, 230-kV, and 345-kV, since one of the advantages by introducing LFAC-transmission systems is that one can use the devices (of the same V/H operating value) that have generally been used in nominal frequency such as transmission lines, transformers, and protection relays [14]. Table 6.1 shows three cases, according to operational voltages. In the three cases, the transmission distance is changed from 0 to 200 miles, and the MPTC is recorded according to the transmission distance.

Table 6.1: Operating Voltages for Power Transfer Studies

	Case 1	Case 2	Case 3
Operating Frequency of 60Hz	38-kV	76-kV	115-kV
Operating Frequency of 20Hz	38-kV	76-kV	115-kV

In this operational study, the maximum transmitted power from the PCC to the grid system is investigated in the variations of the three parameters (operational voltage and frequency, and transmission distance), while the voltage drop between the sending and the receiving terminal of the three-phase transmission lines remains between -5% and 5% of the operating voltage. Also, the modulation indices of the converters are checked as to whether the converters are working within reasonable limits of the modulation indices (around 0.93-0.85) and of the DC-voltage level. Note that small modulation indices can generate huge harmonics, leading to impractical filter designs. The inverter should support DC voltage for the rectifiers connecting wind turbine systems, since the DC voltage level is important for the reliable operation of the LFAC-transmission systems. Here, the simulation results of three cases shown in Table 6.1 are presented in

tables and graphs, in which the maximum power transfer capability is recorded, according to the transmission distance from 10 to 200 miles.

Case 1: Rated Power Line Voltage: 38 kV (line-to-line).

Table 6.2: Maximum Transmission Capability at the Operation Voltage of 38kV.

	Capability of Power Transmission (MW)										
Distance (miles)	10	30	50	70	90	100	120	140	160	180	200
Transfer Capability (MW) at 60Hz	64.0	23.05	13.94	9.96	7.73	6.95	6.05	5.29	4.89	4.59	4.40
Transfer Capability (MW) at 20Hz	124.7	65.44	41.40	29.68	23.07	20.39	17.36	14.23	11.72	9.49	7.24

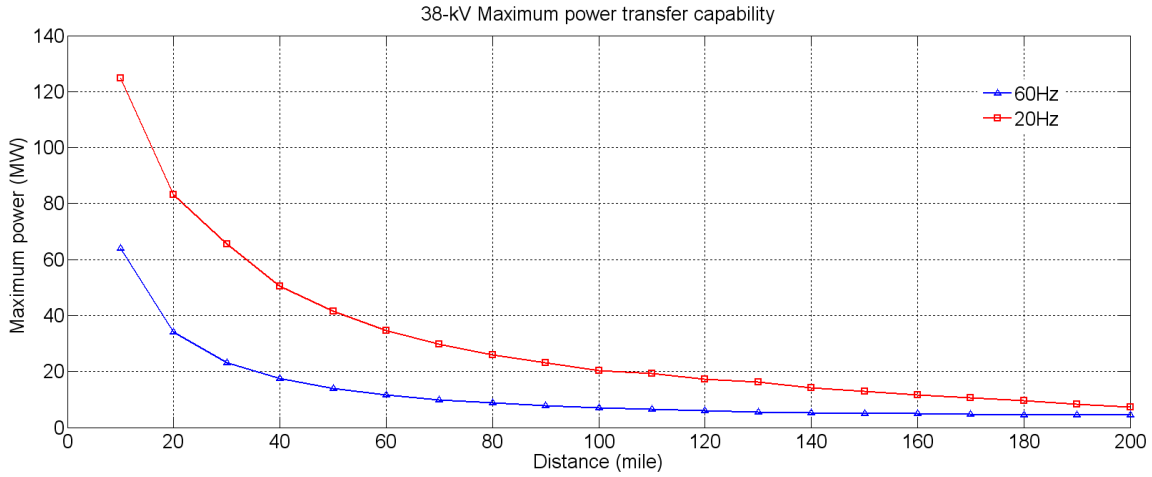

Figure 6.2: Power Transmission Capability of the Operation Voltage of 38-kV.

Case 2: Rated Power Line Voltage: 76 kV (line-to-line).

Table 6.3: Maximum Transmission Capability at the Operation Voltage of 76-kV.

	Capability of Power Transmission (MW)										
Distance (miles)	10	30	50	70	90	100	120	140	160	180	200
Transfer Capability (MW) at 60Hz	180.3	82.8	57.54	44.17	36.78	34.31	30.56	27.98	26.19	24.84	23.38
Transfer Capability (MW) at 20Hz	225.3	141.3	106.1	86.28	73.49	68.29	60.19	54.27	49.22	45.21	41.96

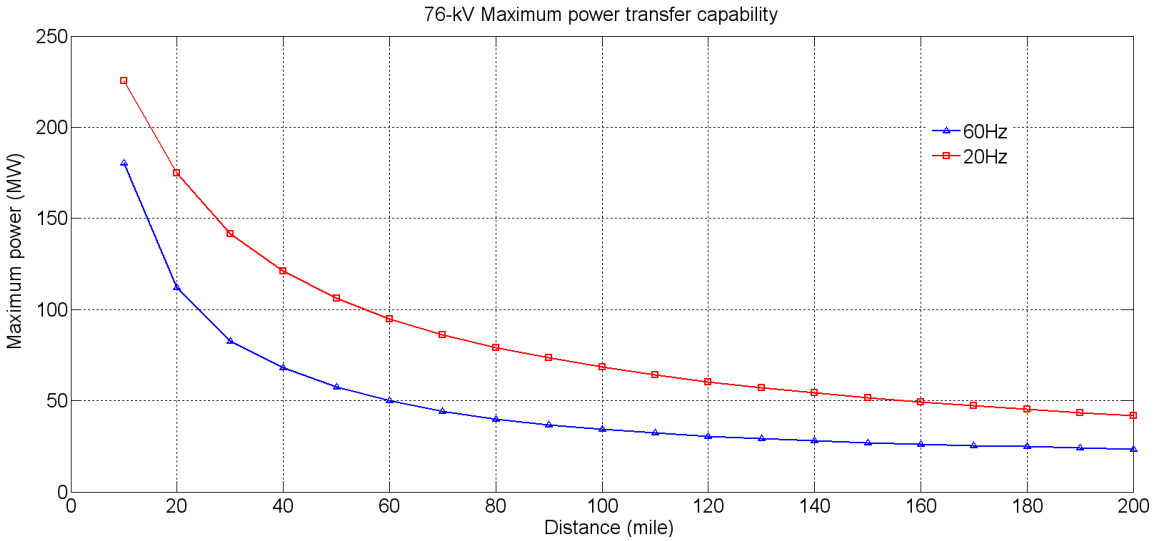

Figure 6.3: Power Transmission Capability of the Operation Voltage of 76-kV.

Case 3: Rated Power Line Voltage: 115 kV (line-to-line).

Table 6.4: Maximum Transmission Capability at the Operation Voltage of 115-kV.

	Capability of Power Transmission (MW)										
Distance (miles)	10	30	50	70	90	100	120	140	160	180	200
Transfer Capability (MW) at 60Hz	301.4	147.8	101.8	79.21	66.44	61.54	55.60	51.14	48.01	45.62	43.98
Transfer Capability (MW) at 20Hz	401.5	264.9	202.8	169.0	143.8	135.7	120.7	108.1	98.69	91.16	84.60

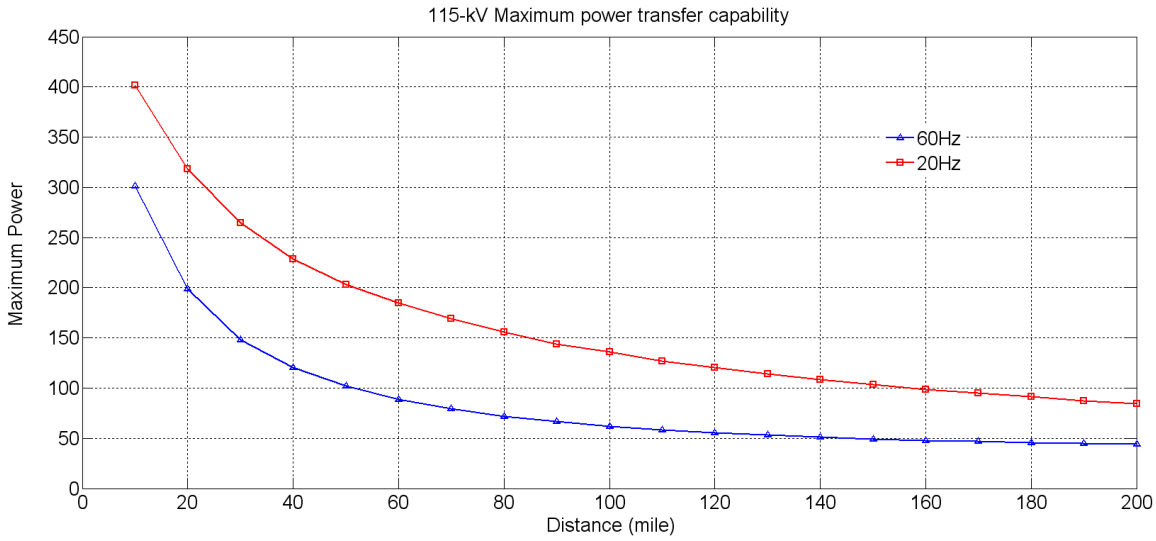

Figure 6.4: Power Transmission Capability of the Operation Voltage of 115-kV.

6.3 Transient-Stability Study in Quasi-Steady State

This section presents the transient stability studies of LFAC-transmission systems using a three-phase, six-pulse cycloconverter. For this purpose, the averaging models of converters in quasi steady-state are used. The converter models in quasi steady-state operate in sinusoidal, steady-state condition, and it is assumed that the mechanical system of generators is only working dynamically [29]. These models are presented in Chapter 4.

Power systems are subjected to frequent disturbances, which may be small or large [46]. The small disturbances in power systems should be state variations of electrical switches, transformer-tap, load configurations, etc. Since these small disturbances occur continuously, the disturbances must be managed continuously and appropriately in power systems for secure system operation. However, the large disturbances of a short circuit on transmission systems, the loss of a large generator, etc., become reasons for fluctuation of system voltages and severe damage to power systems. In transient stability studies, the ability of LFAC-transmission systems to sustain steady voltages from transient conditions is investigated in several cases.

6.3.1 Technical Approach of Transient Stability Studies

Voltage stability and voltage recovery have been recognized to be of paramount importance for secure system operation. As a well-known fact, slow voltage recovery after disturbance causes significant damage, in which voltage collapse and blackout can be caused by power system instability in power systems [47] .

The integration of renewable resources (wind, solar, and hydro energy, etc.) and transmission using converters have highly increased electrical stress on power systems. The knowledge and understanding of the impact on alternative transmission systems during contingencies, such as system faults and partial shut-down of wind-farm systems, help secure the operation of wind farm systems. In the past, wind farms could be disconnected from power systems during excessive voltage instability since the total capacity of wind-energy generation was small, compared to that of other sources. However, the penetration of wind energy into the grid is rapidly increasing, and the transmission capacity from wind farms may be a substantial portion of the overall generation. Thus, the recent grid requirements demand the continuing operation of wind farms like synchronous power plants, during and after contingencies [48]. Therefore, grid codes for wind systems have become stricter than those of the past, and it even seems that wind farms are expected to work as synchronous power plants in order to be connected to other systems.

Voltage ride-through (VRT) capability for wind power systems is essential for secure operation of power systems. The VRT capability requirement for wind power systems is described by NERC standards. Table 6.5 and Figure 6.5 provide voltage profiles from NERC standards: the wind-power systems should be sustained within the voltage requirement during system disturbances [49]. High voltage ride-through (HVRT) refers to the upper limits, and low voltage ride-through (LVRT) refers to the lower limits, according to contingency time.

Table 6.5: NERC PRC-024-1 Voltage-Ride-Through Requirement.

HVRT DURATION	
Time (second)	Voltage (pu)
0.20	1.200
0.50	1.175
1.00	1.150
4.00	1.100

LVRT DURATION	
Time (second)	Voltage (pu)
0.15	0.000
0.30	0.450
2.00	0.650
3.00	0.750
4.00	0.900

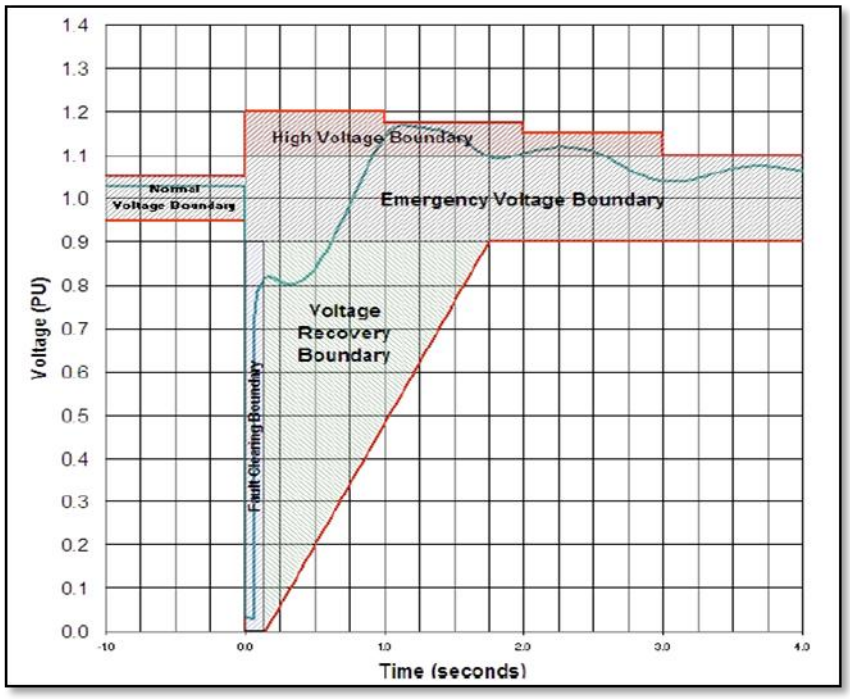

Figure 6.5: NERC PRC-024-1 Voltage-Ride-Through Requirement Curve.

For transient stability studies, quasi steady-state models are introduced in an averaging concept. Since the quasi steady-state models consider dynamics at specific frequency, the analysis using averaging models in quasi steady-state presents a more reliable analysis, compared to earlier attempts for which wind generation systems are modeled in steady-state. Note that the transient stability analysis in the steady-state requires excessive simplicity leading to an erroneous assessment of system stability.

All models in power systems are modeled in quasi steady-state, but the modeling concepts are the similar to those in the steady-state. For example, the converters are modeled in averaging modeling concepts in phasor representation; however, the continuous power flow and control constraints in converters are allowed to vary in dynamics in each time-step. Therefore, the power systems modeled in quasi steady-state are desirable in voltage stability and voltage recovery phenomena, while avoiding either excessive modeling or simulation in the full time-domain [14].

The methodology for stability study is also based on computer simulation over case configurations of wind farm systems, using LFAC-transmission systems. While the example configurations are operating under a normal conditions, a three-phase fault or a partial shutdown of wind farm systems are generated at a specific point in the example configuration. From the disturbance, the example systems are observed as to whether the example configurations using the LFAC-transmission systems can sustain continuing operation, and whether the configuration can satisfy the grid-code requirements.

6.3.2 Case Studies of Voltage Stability Study

Here, we introduce two wind farm configurations using LFAC-transmission systems for voltage stability studies: the first configuration (Configuration 1) is an LFAC-transmission system interconnecting 20-Hz series wind farms and a 60-Hz grid system, while the second configuration (Configuration 2) is a network connection of LFAC-transmission systems connecting DC wind farms. The transient stability studies are performed on the two wind farm configurations, using the voltage ride-through

requirement. The two configurations are investigated over their own scenarios, according to fault position, disturbance type, clearing time, etc. after a disturbance.

Configuration 1: An LFAC-transmission system connecting 20-Hz series wind farms

This configuration 1 presents an example configuration of a series LFAC-transmission system interconnecting two wind farms of 25-MW and a grid system, as shown in Figure 6.6. The wind farm consists of tens of wind turbines and full-size inverters/converters. Each wind-turbine generates 20-Hz AC power of 5-MW with 2.5-kV rating voltage and series connected to each other with 300-meter spacing. The distance of the LFAC-transmission system is 25-miles with a rating voltage of 35-kV. At the end of the LFAC-transmission line, a cycloconverter interconnects the LFAC-transmission system and main grid system. A step-up transformer boosts the voltage to 115-kV for voltage synchronization with the main grid system.

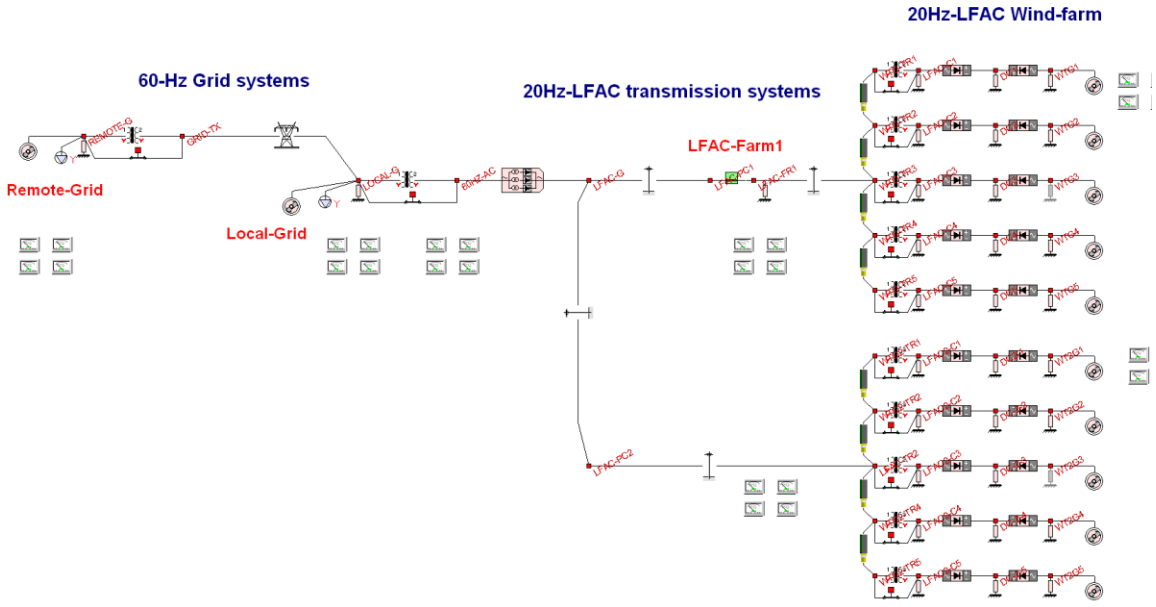

Figure 6.6: Single-Line Diagram of an LFAC-Transmission System Connecting a Series LFAC Wind Farm to the Main Grid.

Scenario 1: While the wind farms transmit 50-MW electrical power into grid systems in steady state, a three-phase fault is generated at the remote grid (at the point of REMOT-GRID in Figure 6.6). A three-phase fault has an impact on Configuration 1 during 0.15 seconds from the initial fault time and is clear at 0.25 seconds. Figure 6.7 represents the simulation results from 0.0 to 4.0 seconds: the graphs from (A) to (C) represent the magnitude of phase-A voltage at the remote grid, the local grid, and the high-frequency side of the cycloconverter, respectively. Also, Figure 6.8 shows that the frequency and active power are oscillating on the equilibrium points after the three-phase fault is cleared. In this scenario, the wind-farm configuration using the LFAC-transmission system has the ability to operate continually after the three-phase fault is cleared.

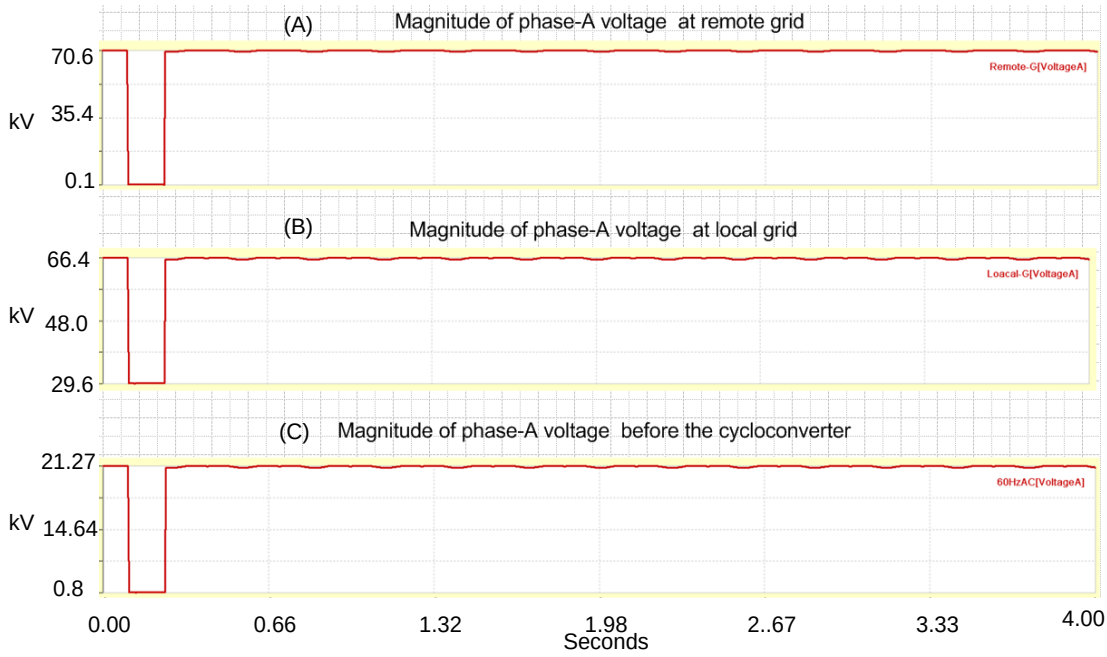

Figure 6.7: Configuration 1: Voltage Magnitude of Phase A at (A) the Remote Grid; (B) the Local Grid; (C) before the Cycloconverter.

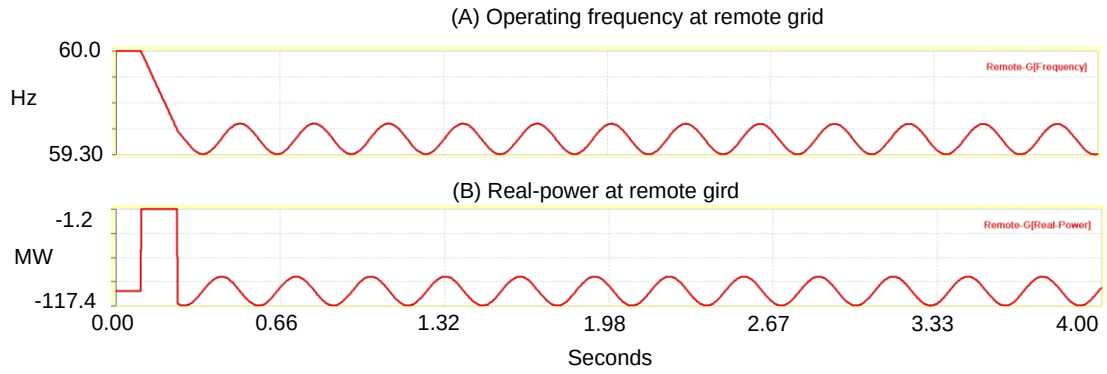

Figure 6.8: Configuration 1: (A) Operating Frequency; and (B) Real Power at the Remote Grid during a Three-Phase Fault at the Remote Grid.

Scenario 2: While the wind farm transmits 50-MW electrical power into grid systems in steady-state, a three-phase breaker opens during 0.15 seconds at PCC (at LFAC-Farm 1 as shown in Figure 6.6). This simulation shows a contingency in which a large part of the electrical sources (25-MW) is separated from the power system and is then reconnected. Figure 6.9 represents the simulation results from 0.0 to 4.0 seconds: the graphs from (A) to (C) represent the magnitude of the phase-A voltage at the remote grid, the local grid, and the high-frequency side of the cycloconverter, respectively. Also, Figure 6.10 shows that the frequency and real-power are oscillating on the equilibrium points after the contingency is cleared. Even though the test system is swing, the voltages are in-bound of the VRT requirement. Therefore, the systems have the ability to continue operation after the contingency.

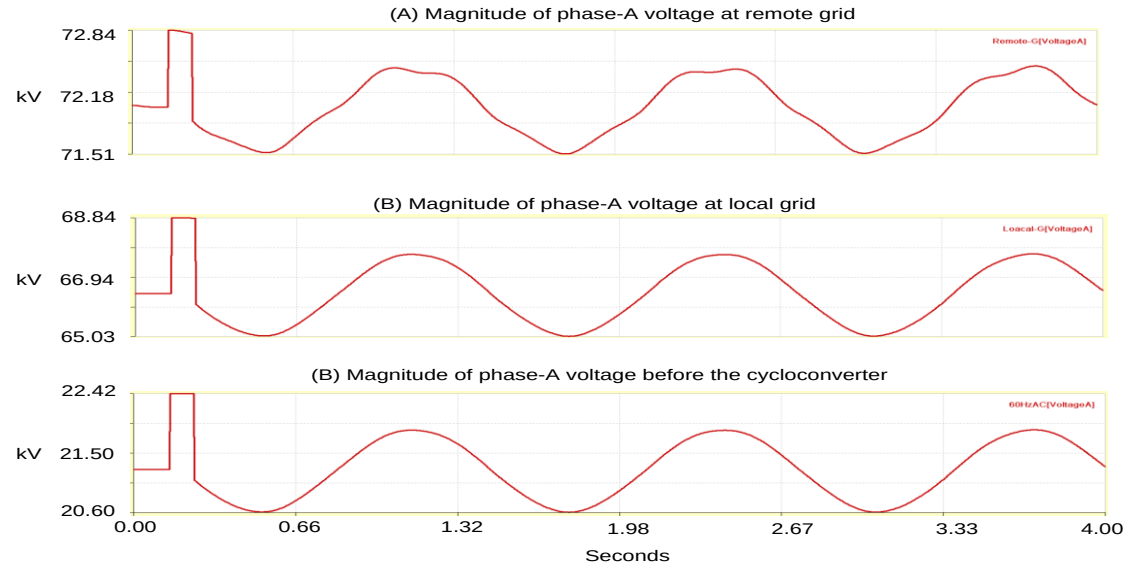

Figure 6.9: Configuration 1: Voltage Magnitude of Phase A at (A) the Remote Grid; (B) the Local Grid; and (C) before the Cycloconverter.

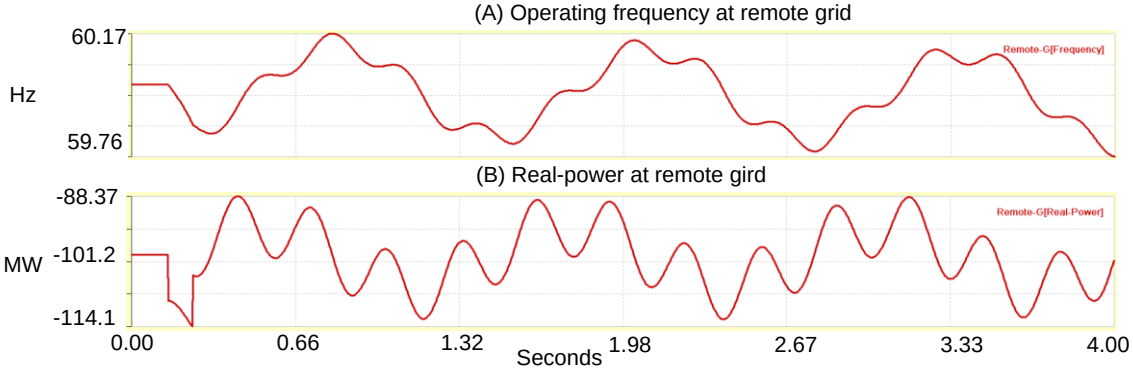

Figure 6.10: Configuration 1: (A) Operating Frequency; and (B) Real Power at the Remote Grid during the Recloser Operation.

Configuration 2: An LFAC-transmission system connecting the DC wind farm

This configuration 2 presents a network configuration of LFAC-transmission systems interconnecting DC wind-farms and main grid systems as shown in Figure 6.11. Each wind turbine generates 20-Hz AC power of 5-MW at a 2.5-kV rating voltage and series connected to each other with 300-meter spacing. The distance of the LFAC-transmission systems is 25-miles with a rating voltage of 35-kV. At the end of the LFAC-transmission line, a cycloconverter interconnects the LFAC-transmission system and the grid system. A step-up transformer boosts the voltage to 115-kV to voltage synchronization.

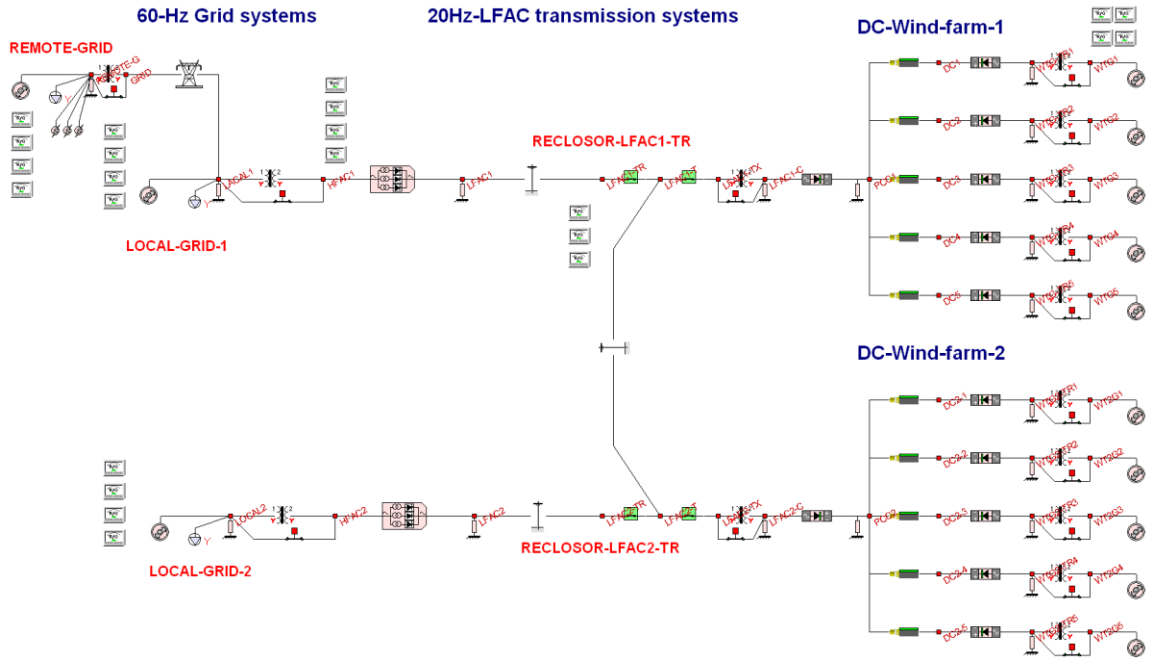

Figure 6.11: Single-Line Diagram of LFAC Transmission Network Connecting a Series DC Wind Farms.

Scenario 1: While the wind farm transmits 50-MW electrical power into grid systems in steady-state, a three-phase fault is generated at the remote grid (at the point of REMOT-GRID in Figure 6.11). A three-phase fault has an impact on the configuration 2 during 0.15 seconds from the initial fault time and is cleared at 0.25 seconds. Figure 6.12 represents the simulation results from 0.0 to 4.0 seconds: the graphs from (A) to (C) represent the magnitude of phase-A voltage at the remote grid, the local grid, and the high-frequency side of the cycloconverter, respectively. Also, Figure 6.13 shows that the frequency and real power are oscillating on the equilibrium points after the three-phase fault is cleared. In this scenario, the wind farm configuration, using the LFAC-transmission systems, has the ability to operate continually after the three-phase fault is cleared, since the VRT requirement is satisfied.

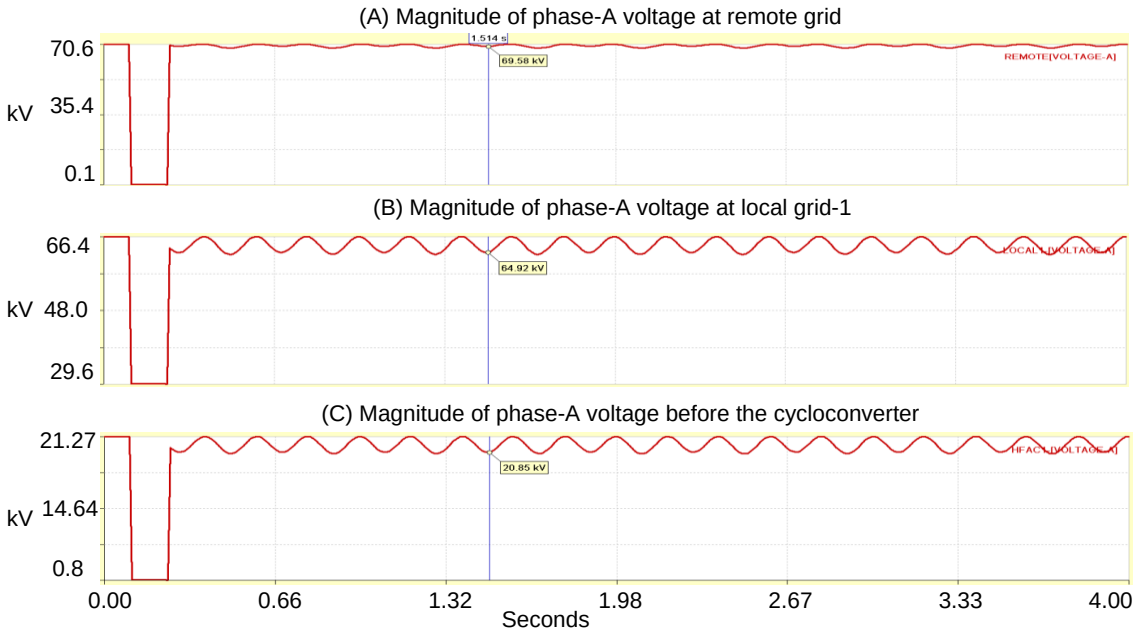

Figure 6.12: Configuration 2: Voltage Magnitude of Phase A (A) at the Remote Grid; (B) at the Local Grid 1; and (C) before the Cycloconverter during a Three-Phase Fault at the Remote Grid

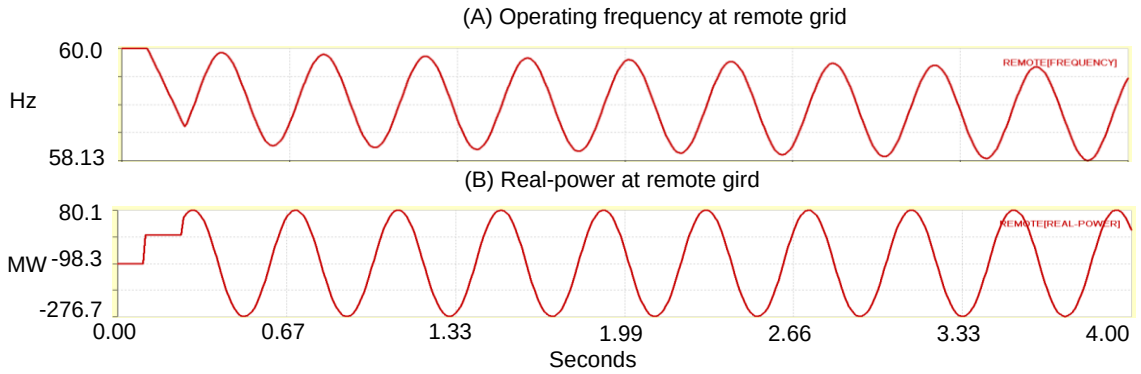

Figure 6.13: Configuration 2: (A) Operating Frequency; and (B) Real Power at the Remote Grid during a Three-Phase Fault at the Remote Grid.

Scenario 2: While the wind farm transmits 50-MW electrical power into the grid systems in steady-state, a three-phase fault is generated at the local grid (at the point of LOCAL-GRID-1 in Figure 6.11). A three-phase fault has an impact on configuration 2 during 0.15 seconds from the initial fault time and is cleared at 0.25 seconds. Figure 6.14 represents the simulation results from 0.0 to 4.0 seconds: graph (A) represents the magnitude of phase-A voltage at the remote grid, while the graph (B) represents the magnitude of phase-A voltage at the local grid. Also, Figure 6.14 shows that the real-power (C) and frequency (D) are swing after the three-phase fault is cleared. Even though the voltages are recovered, the phase-A voltage at the remote grid oscillates and is smaller than the LVRT requirement. Thus, configuration 2 is unstable after the three-phase fault is cleared.

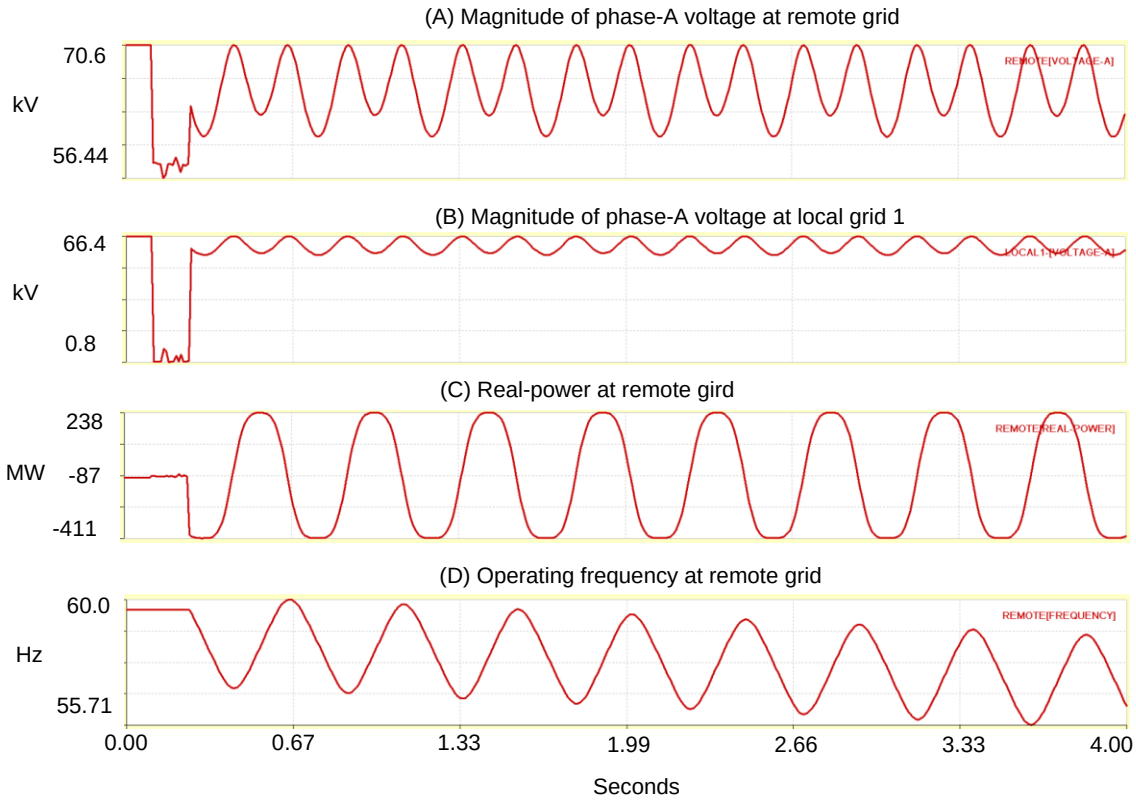

Figure 6.14: Configuration 2: Magnitude of Phase A Voltages at (A) the Remote Grid; and (B) the Local Grid 1; and (C) Real Power and Operating Frequency at the Remote Grid.

Scenario 3: While the wind farms transmit 50-MW electrical power into grid systems in steady-state, a three-phase breaker opens at 0.5 seconds at the point (RECLOSOR-LFAC1-TR in Figure 6.11). This example simulation shows a contingency in which large parts of power generation units are disconnected, and the configuration of the power system is dramatically changed. Figure 6.15 represents the simulation results from 0.0 to 4.0 seconds: graph (A) represents the magnitude of the phase-A voltage at the remote grid. Note that since the phase-A voltage at the local-grid 1 is not satisfied by the VRT requirement, in which the operational voltage exists between 0.9 and 1.1 of rated voltage. Thus, the system is in instability after the contingency is cleared.

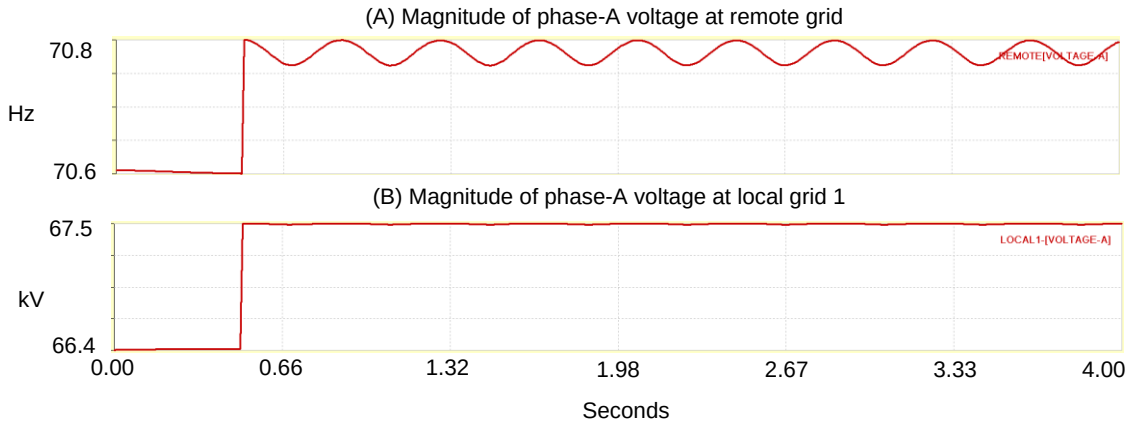

Figure 6.15: Configuration 2: Magnitude of Phase A Voltages at (A) the Remote Grid; and (B) the Local Grid 1 during the Recloser Operation at RECLOSOR-LFAC1-TR.

6.4 Time-domain Study

This section presents time-domain studies of alternative transmission systems using LFAC-transmission systems. The LFAC-transmission systems consist of full time-domain models which are realistic and accurate models directly derived from physical components using QMQI. The converter models of the three-phase, six-pulse converter, the three-phase, six-pulse cycloconverter, and the three-phase PWM converter shown in Chapter 5 are used for time-domain studies, such as power transient simulations and harmonics studies. These time-domain studies allow for a better understanding of the dynamic behavior of LFAC-transmission systems.

LFAC-transmission systems employ a number of three-phase, PWM converters to connect wind turbine systems, and a three-phase, six-pulse cycloconverter to interconnect grid systems and an LFAC-transmission system. Since these converters use solid-state electronics to alter one wave-form to another according to their own purposes, the converters are highly productive harmonic sources. Harmonic pollution in power system causes several problems: heat problems in transformer and electrical machines, aging problems of isolation in power-system devices, malfunction of dynamic control systems, and inductive interference over communication networks [14],[50]. Harmonics should be eliminated and wave-forms, such as voltages and currents are nearly pure sinusoidal signals in power systems. Understanding harmonics from LFAC-transmission systems help to optimally design harmonic filters and allow power systems using LFAC-transmission systems to operate with high quality.

LFAC-transmission systems should support continuing operation, while either electrical loads or variable wind sources vary in real-time. The flexible control of LFAC-transmission systems is required for the reliable and robust operation of power systems. The converters in LFAC-transmission systems can support controllability for continuing operation: the three-phase PWM converters offer the controllability of active and reactive power and voltage level, while the three-phase, six-pulse converter allows frequency and voltage level control of a low-frequency side. However, inappropriate controller and circuit designs can become the reason for switching malfunctions, leading to voltage and current spikes. Note that electrical switches should be damaged physically, and then system shutdowns can occur from these spikes. Power transient studies are expected to help optimally design control systems of converters and understand the knowledge for continuing operation of LFAC-transmission systems.

6.4.1 Technical Approach of Time-Domain Studies

Time-domain studies are performed using two LFAC-transmission systems interconnecting a wind farm and main grid systems, as shown in Figure 6.16 and Figure 6.17. For the LFAC-transmission systems, variable-speed wind turbine systems (Type-3 and Type-4 wind-generation units) are considered, since variable-speed wind generation systems are attractive for increasing energy capture and reducing mechanical-fatigue damage. The variable-speed wind turbine systems cannot be directly connected to grid systems and converters are used to connect systems with different frequencies. In the proposed wind farm configurations, three-phase PWM converters and a three-phase, six-pulse cycloconverter are used to interconnect systems with different frequencies. The three-phase PWM converters interconnect wind farms and an LFAC-transmission system,

while the three-phase cycloconverter interconnects the LFAC-transmission system and nominal frequency grid systems. Also, each converter performs its own roles: the cycloconverter controls the operating frequency of the LFAC-transmission system and allows voltage synchronization for the three-phase PWM inverters; the three-phase PWM inverters should support the DC voltage level and the controllability of the reactive power of the LFAC-transmission systems; and the three-phase PWM rectifiers allow power tracking to extract the maximum power from the wind turbines [14], [36],[37].

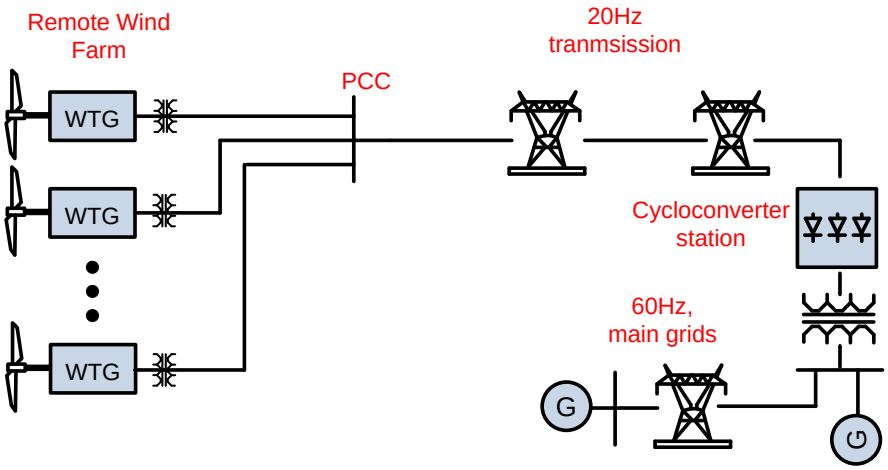

Figure 6.16: Wind Farm Configuration: LFAC Wind Farm and LFAC Transmission.

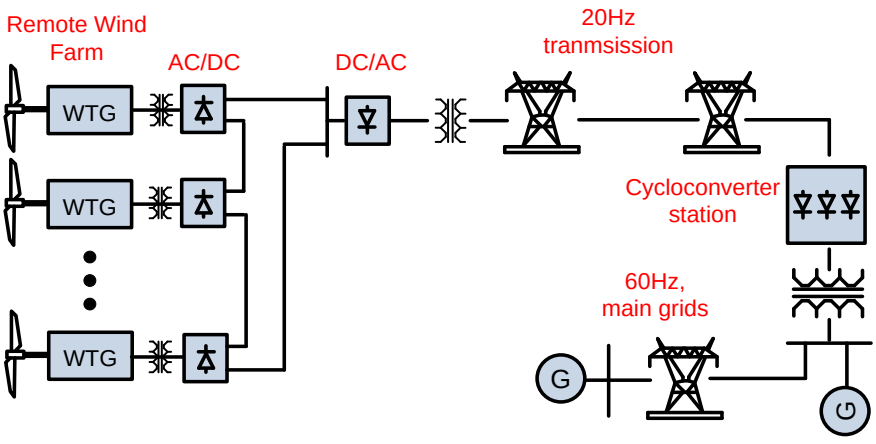

Figure 6.17: Wind Farm Configuration: Series DC Wind Farm and LFAC Transmission.

Using the example systems, power transient studies and harmonics studies are performed. For the power transient studies, power-step changes (the required power-order) suddenly occur, while the LFAC-transmission systems are operating in steady-state. Also, harmonics studies are performed, according to the control modes (partial- and full-circulating current modes), and the modulation indices of the cycloconverter. Since the cycloconverter is directly connected to the grid systems, the harmonic studies of the cycloconverter are of importance.

6.4.2 Power Transient Studies of LFAC-Transmission Systems

For power transient studies, we introduce two wind farm configurations using an LFAC-transmission system. The first wind farm configuration uses a parallel low-frequency wind farm and a radial LFAC-transmission system, as shown in Figure 6.18, and the second configuration uses DC wind farm in series and a radial LFAC-transmission system as shown, in Figure 6.22. Using the two wind farm configurations, power transient studies are performed. In this simulation, the power-step change suddenly occurs, while the LFAC-transmission system operates in steady-state.

Case 1: Wind-Farm configuration: LFAC wind farm and LFAC-transmission system

Case 1 presents the simulation results of an example wind farm with an LFAC-transmission system connected to a power grid, as shown in Figure 6.18. The wind farm consists of many wind turbine systems - the example system includes three of them. The wind-generated power is rectified to DC, and then it is converted to 20-Hz AC power. A transformer boosts the voltage to 46-kV. An LFAC-transmission line operated at 46-kV transmits the power over a distance of 100-km to the nearest power grid substation. At

that point, a cycloconverter converts the 20-Hz AC power into 60-Hz AC power and another transformer boosts the voltage to 115-kV for the interconnection. The transformer is connected to the power grid, which is a 115-kV, 60-Hz system at that point. The three-phase six-pulse cycloconverter operates in a full circulating-current mode, and the control algorithm for generating the switching pulses is the cosine wave-crossing method [36].

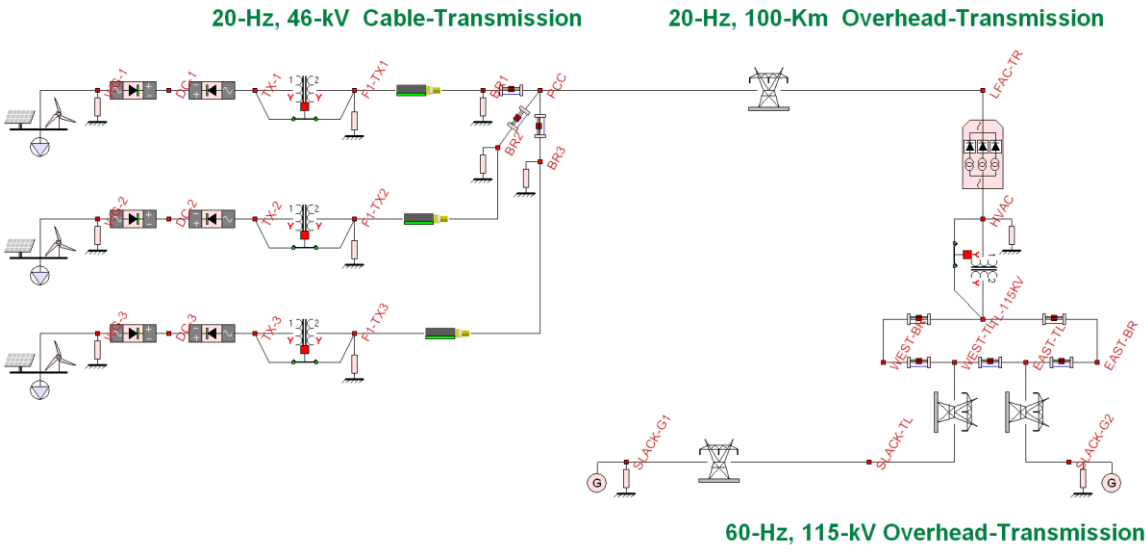

Figure 6.18: Wind Farm Configuration: LFAC Wind Farm and LFAC Transmission

Each wind turbine/generator system consists of a wind-turbine, full-rectifier and full-inverter that converts variable frequency power into 20-Hz power and a transformer that boosts the voltage to 46 kV. The power from all wind turbine/generator systems is collected at a common connection point (PCC), and the total power is transmitted via an LFAC-transmission line to the interconnection point with the power grid. The interconnection is achieved with the cycloconverter and the step-up transformer. The wind farm system using the LFAC-transmission system was simulated in a transient

condition. Specifically, while the system is operating with 4-MW through the LFAC line, suddenly the wind power changes to the point that requires the LFAC line to transmit 9-MW.

Figure 6.19 represents three-phase (a) line-to-line voltages and (d) currents at the 60Hz AC-transmission system connected to the three-phase, six-pulse cycloconverter, three-phase (c) voltages and (b) currents at the LFAC-transmission system connected to the three-phase, six-pulse cycloconverter, and the (e) real power from the wind farm and the (f) RMS voltage at the LFAC-transmission system, while the power demand suddenly changes from 4MW to 9MW after 3 seconds. Figure 6.20 shows the results during the transient condition from 2.80 to 3.40 (seconds) – a zoom-in view, and Figure 6.21 represents the results during steady-state from 6.75 to 7.00 (seconds). Note that the output power can be automatically regulated by controlling the power angle δ. The transient conditions last shorter than 0.15 seconds.

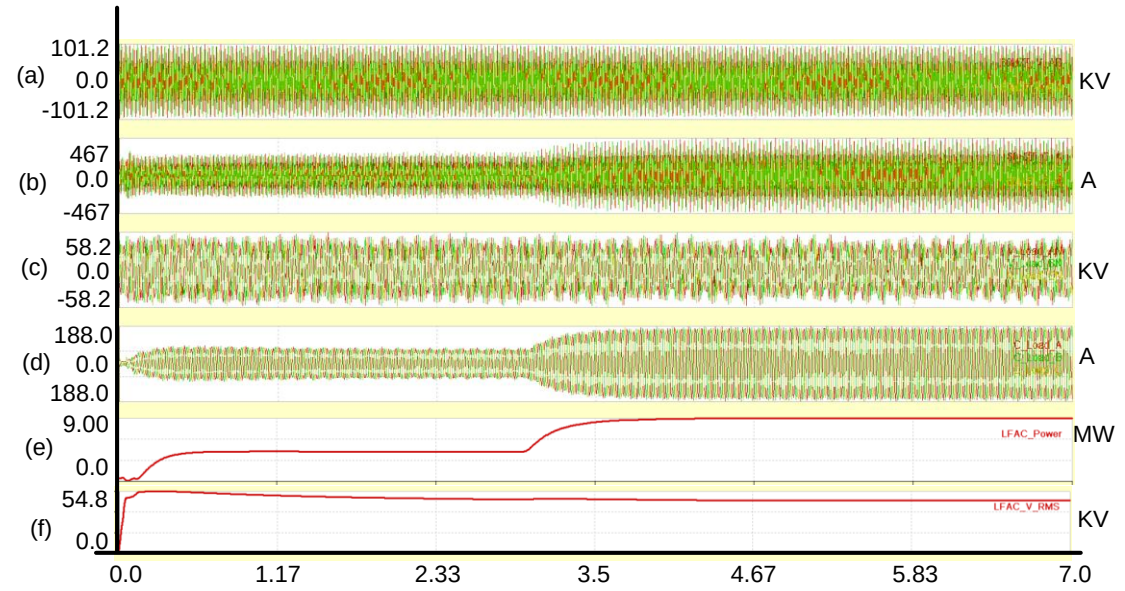

Figure 6.19: Three-Phase (a) Line-to-Line Voltages and (d) Currents at 60Hz AC Transmission Connected to the Cycloconverter; Three-Phase (c) Voltages and (b) Currents at LFAC Transmission Connected to the Cycloconverter; and (e) Real Power from the Wind Farm and (f) the RMS Voltage at the LFAC from 0.0 to 7.0 Seconds.

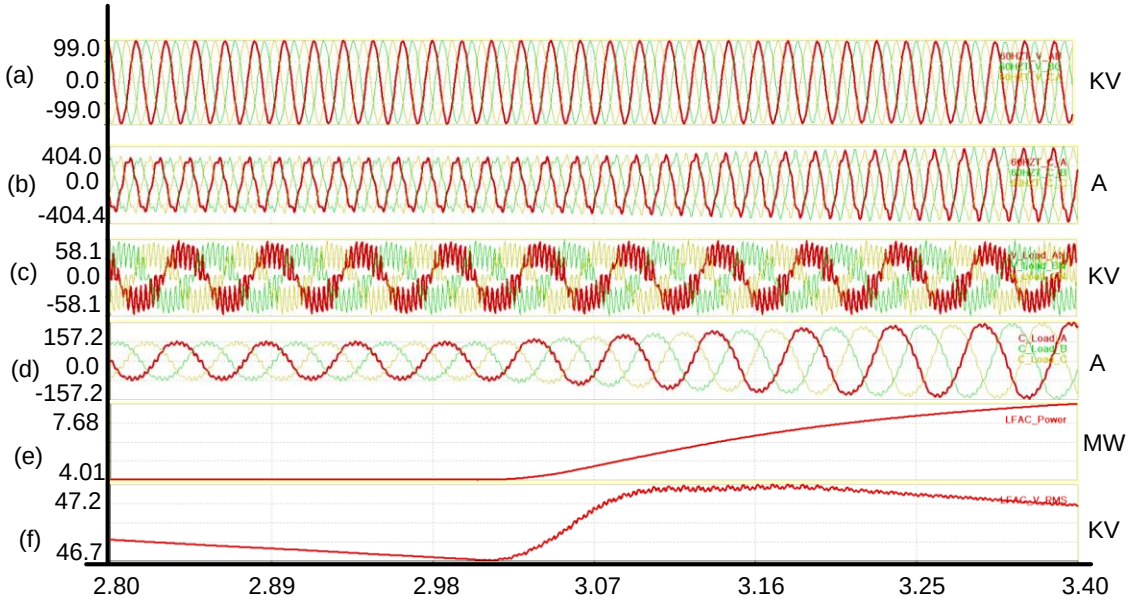

Figure 6.20: Three-Phase (a) Line-to-Line Voltage and (d) Currents at 60Hz AC Transmission Connected to the Cycloconverter; Three-Phase (c) Voltages and (b) Currents at LFAC Transmission Connected to the Cycloconverter; and (e) Real Power from the Wind Farm and (f) the RMS Voltage at the LFAC from 2.8 to 3.4 Seconds.

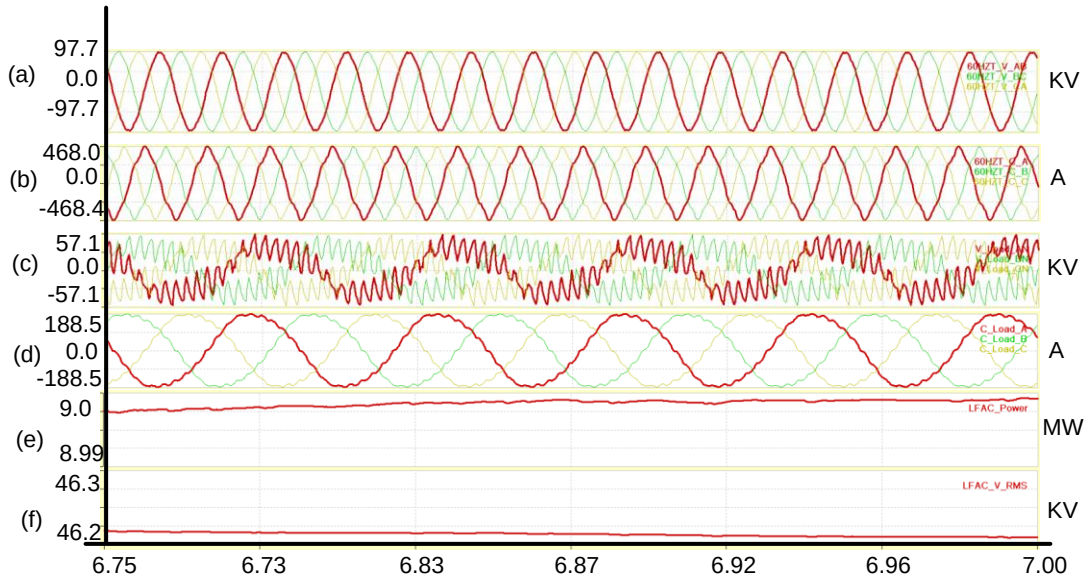

Figure 6.21: Three-Phase (a) Line-to-Line Voltage and (d) Current at 60Hz AC Transmission Connected to the Cycloconverter; Three-Phase (c) Voltages and (b) Currents at LFAC Transmission Connected to the Cycloconverter; and (e) Real Power from the Wind Farm and (f) the RMS Voltage at the LFAC from 6.75 to 7.0 Seconds

Case 2: Wind farm configuration: DC wind farm and LFAC-transmission system

This case study presents the simulation results of an example wind-farm with an LFAC-transmission system connected to a power grid, as shown in Figure 6.22. The wind farm consists of many wind turbine systems - the example system includes three of them. The wind turbine systems are connected in series after the wind-generated power is rectified to DC, and the DC power is converted to 20-Hz AC power using an inverter. A transformer boosts the voltage to 46-kV. An LFAC line operated at 46-kV transmits the power over a distance of 80-Km to the nearest power grid substation. At that point, a cycloconverter converts the LFAC power into 60-Hz AC power for the interconnection, and another transformer boosts the voltage to 115-kV. The transformer is connected to the power grid, which is a 115-kV, 60 Hz-transmission at that point [37].

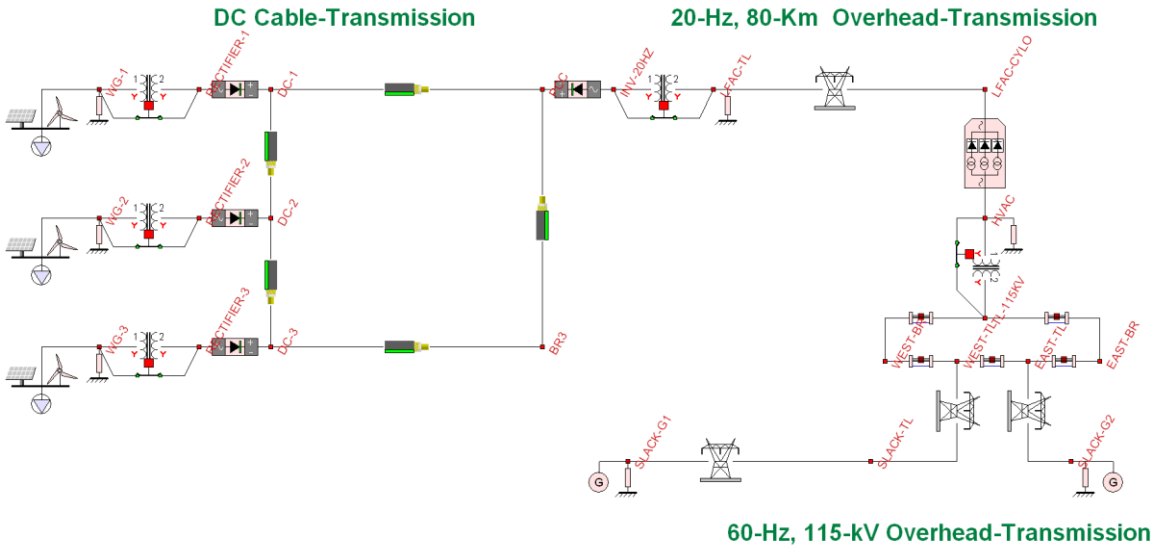

Figure 6.22: Single-Line Diagram of a Power Transient Test System.

The results illustrate the operation of a wind farm transmission system by using a three-phase, six-pulse cycloconverter. The three-phase, six-pulse cycloconverter operates in a partial circulating-current mode and the control algorithm used to generate switching pulses is the cosine-wave crossing method.

Figure 6.23 and Figure 6.25 represent three-phase (a) line-to-line voltages and (b) currents at the 60Hz AC transmission system connected to the three-phase, six-pulse cycloconverter, and three-phase (c) voltages and (d) currents at the LFAC- transmission system connected to the three-phase, six-pulse cycloconverter. In Figure 6.24, the power demand is 6-MW and the operation mode is a partial circulating-current mode of 0.7-pu of the phase currents at the LFAC side. Figure 6.25 shows the results with the following conditions: the power demand is 10MW, and the operation mode is a partial circulating-current mode of 0.4-pu of the phase current at the LFAC side.

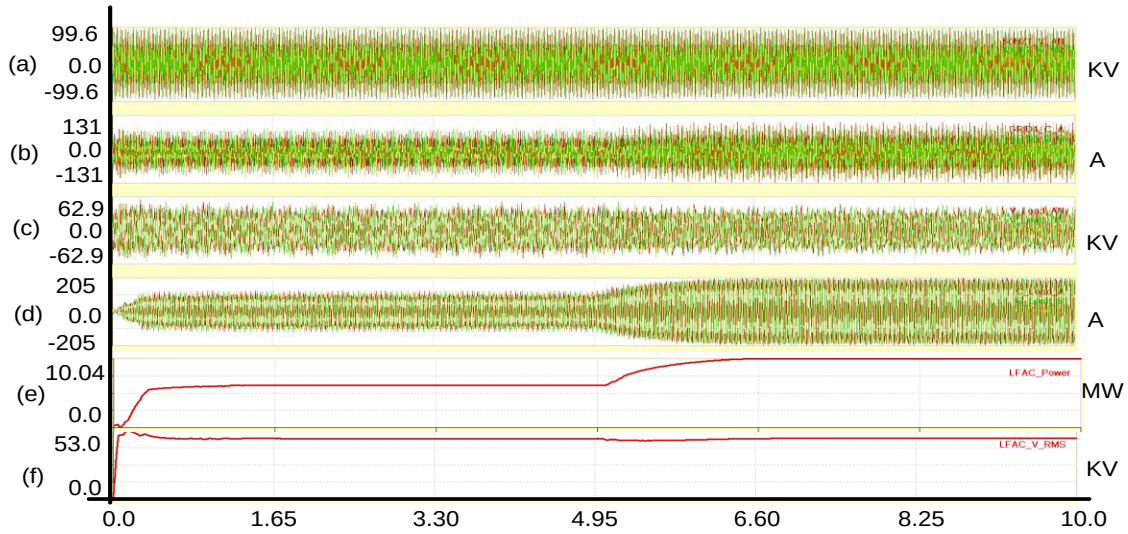

Figure 6.23: (a) Three-Phase Line-to-Line Voltages and (b) Three-Phase Currents at 60Hz AC Transmission Connected to the Cycloconverter; Three-Phase (c) Voltages and (b) Currents at LFAC Transmission Connected to the Cycloconverter; and (e) Real Power from the Wind Farm and (f) the RMS Voltage at the LFAC from 0.0 to 8.0 Seconds.

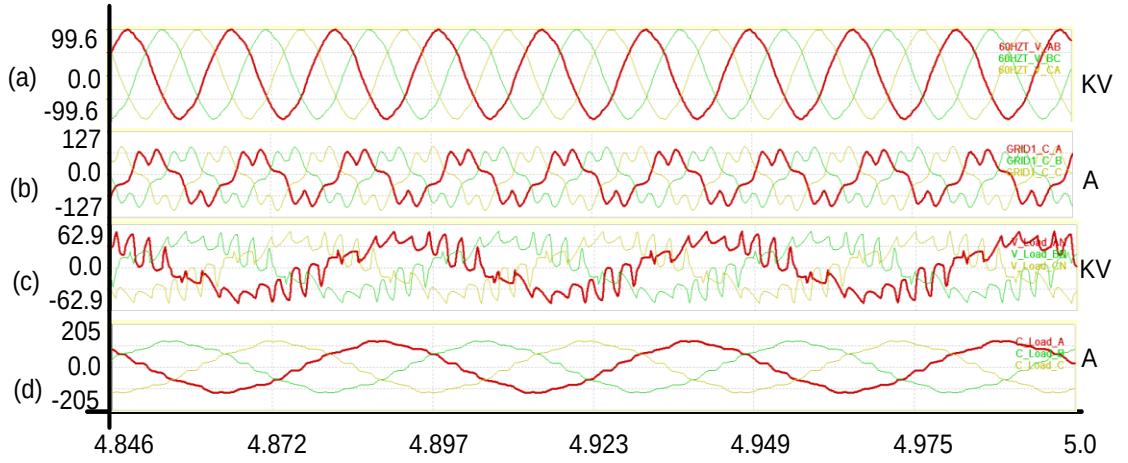

Figure 6.24: (a) Three-Phase Line-to-Line Voltages and (b) Three-Phase Currents at 60Hz AC Transmission Connected to the Cycloconverter; and Three-Phase (c) Voltages and (b) Currents at LFAC Transmission Connected to the Cycloconverter during Steady-State from 4.846 to 5.0 Seconds.

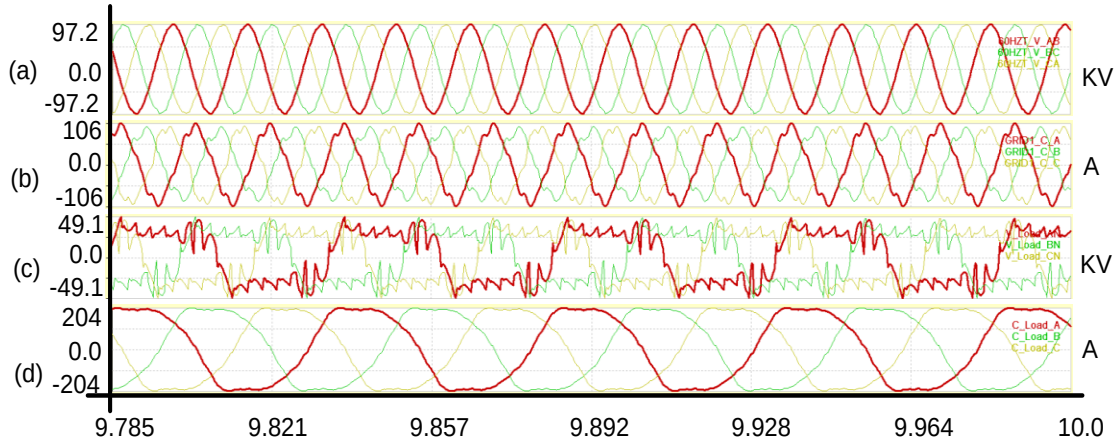

Figure 6.25: (a) Three-Phase Line-to-Line Voltages and (b) Three-Phase Currents at 60Hz AC Transmission Connected to the Cycloconverter; Three-Phase (c) Voltages and (b) Currents at LFAC Transmission Connected to the Cycloconverter during Steady-State from 9.785 to 8.0 Seconds.

Figure 6.26 and Figure 6.27 represent the results in transient conditions: (a) three-phase currents at the 60Hz AC transmission system connected to the three-phase, six-pulse cycloconverter, three-phase (b) voltages and (c) currents at the LFAC-transmission system connected to the three-phase, six-pulse cycloconverter. Figure 6.26 shows the initial transient condition from 0.0 to 0.5 seconds. The cycloconverter is operated in a full circulating-current mode, while the maximum currents at the LFAC-transmission system are smaller than 80-A; otherwise, the cycloconverter is operated in a partial circulating-current mode. In Figure 6.27, the power demand suddenly changes from 6MW to 10MW after 5.0 seconds. Note that the output power can be automatically regulated by controlling the power angle δ. The transient conditions last longer than 1.0 second.

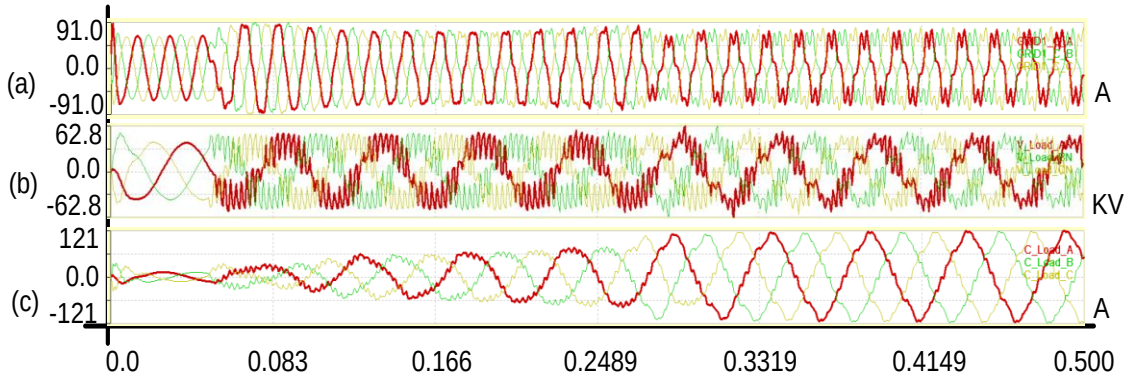

Figure 6.26: (a) Three-Phase Currents at 60Hz AC Transmission Connected to the Cycloconverter; and Three-Phase (b) Voltages and (c) Currents at LFAC Transmission Connected to the Cycloconverter during Steady-State from 0.0 to 0.500 Seconds.

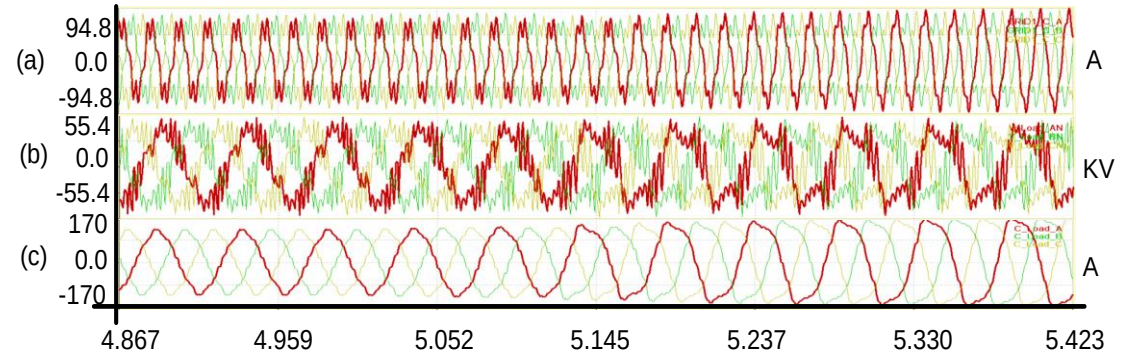

Figure 6.27: (a) Three-Phase Currents at 60Hz AC Transmission Connected to the Cycloconverter; and Three-Phase (b) Voltages and (c) Currents at LFAC Transmission Connected to the Cycloconverter during Steady-State from 4.867 to 5.423 Seconds.

6.4.3 Harmonic Study of LFAC-Transmission Systems

In this subsection, harmonic studies are performed using the LFAC-transmission system, shown in Figure 6.18. The operating voltage of the cycloconverter is 70-kV (RMS) at the high-frequency side, and the operating voltage at the low-frequency side is regulated according to the modulation index of the cycloconverter. The harmonics from a three-phase, six-pulse cycloconverter are changed over the modulation index and the power factor at the low-frequency side. The modulation index is calculated as follows:

$$r = \frac{V_{a-output}}{V_{LL-input} \cdot \cos 30^{o}} \tag{6.1}$$

The transmitted power from the LFAC-transmission system is 10-MW from the wind farm to the grid systems.

Here, the LFAC-transmission system of Figure 6.18 is first analyzed with the modulation index of 1.0, since the wave forms of the voltages and currents are expected to contain a small quantity of harmonics compared to the wave forms from other modulation indices. Figure 6.28 represents the simulation results: (A) the line-to-line voltage between phase *A* and phase *B* and (B) the current at phase *A,* and (C) the phase-voltage and (D) the phase-current at phase *A.* Note that the cycloconverter is operating in full circulating-current mode. The harmonics shown in Figure 6.29 are computed using discrete-Fourier analysis and the harmonic spectra are represented in logarithmic scale: graph (A) is line-to-line voltage between Phase A and Phase B, graph (B) is the current at

Phase A, graph (C) is the phase voltage at Phase A, and (D) is the phase-current at Phase A.

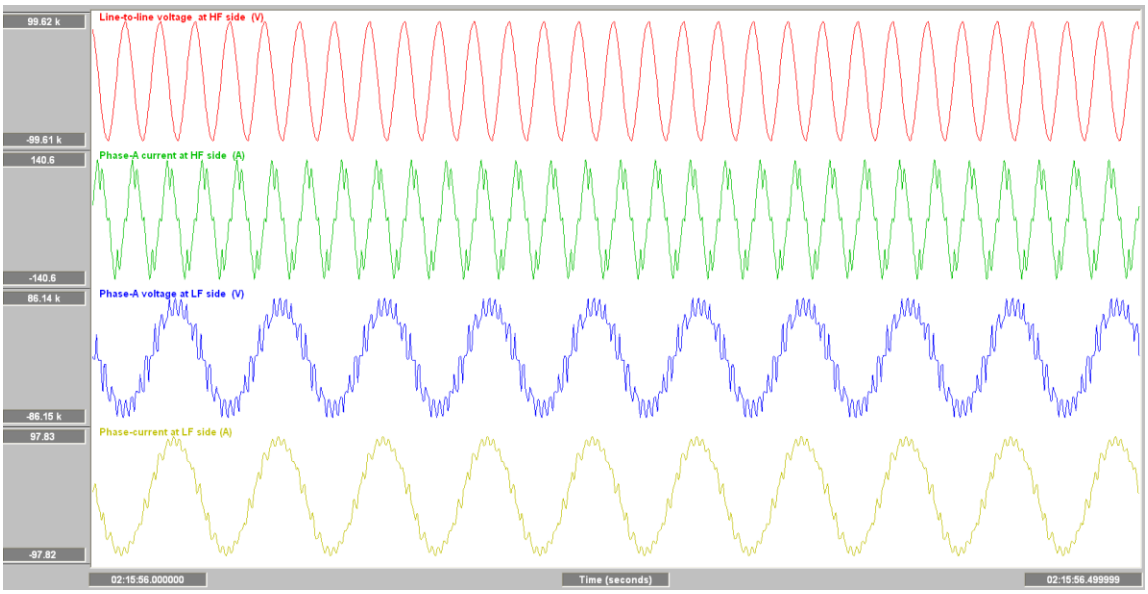

Figure 6.28: (A) Line-to-Line Voltage between Phase A and Phase B; (B) Current at Phase A; (C) Phase Voltage and (D) Phase Current at Phase A.

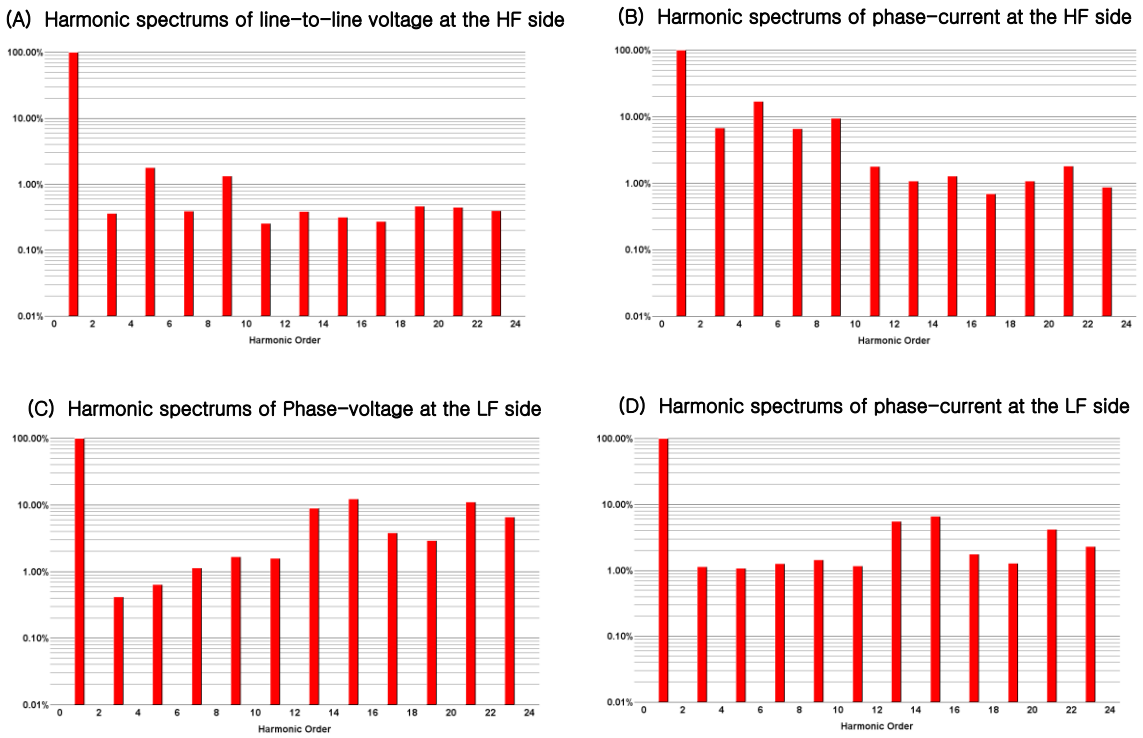

Figure 6.29: Harmonic Spectra: (A) Line-to-Line Voltage between Phase A and Phase B; (B) Current at Phase A; (C) Phase Voltage at Phase A; and (D) Phase Current at Phase A.

Note that the harmonic order is computed as follows:

$$Harmonic\,order = \frac{high\ frequency}{fundamentd\ \ frequency} \tag{6.2}$$

where the fundamental frequency is 60-Hz at the high-frequency side and 20-Hz at the low-frequency side.

To investigate the harmonic spectra of phase voltages at the low-frequency side, the modulation index of the three-phase, six-pulse cycloconverter is continuously increased from 0.35 to 1.0, and numerical values are recorded in Table 6.6, according to harmonic orders. Figure 6.30 represents the harmonic spectra to clearly show that the harmonics are increasing while the modulation index is decreased. As shown in Table 6.6 and Figure 6.30, the unite modulation index only presents 20% of the total harmonic distortions (THDs) while the modulation index of 0.38 generates about 50% of THDs. Therefore, the harmonics are managed by manipulating the proper tap-setting of a transformer and the modulation index of the cycloconverter.

Table 6.6: Numerical Values of Harmonic Contents of the Phase Voltage at LFAC

Modulation Index m_a	Harmonic Order										
	3	5	7	9	11	13	15	17	19	21	THDs
1.00	0.41	0.62	1.2	1.8	1.7	8.9	8.3	3.8	2.9	8.1	20.1
0.88	1.4	1.6	1.8	0.87	0.8	6.3	8.7	3.3	4	8.3	22.52
0.75	2	1.8	2.1	0.51	1.1	4.6	8.7	8.1	8.4	8.3	26.43
0.63	3.9	3.3	1.8	0.22	0.69	3	8.6	20	22	8.1	33.78
0.50	8	3	1	0.77	2.5	8.9	8.9	31	30	6.5	42.14
0.38	17	4.8	3.7	1.4	1.2	0.4	0.04	39	37	2.4	48.87

Unit: percentage (%)

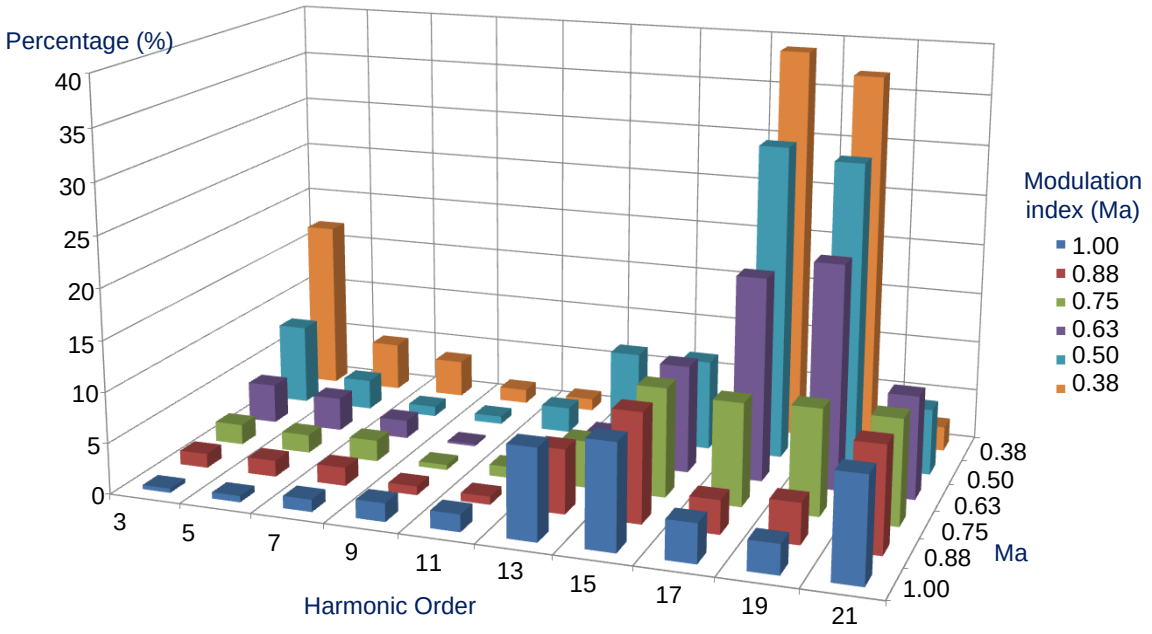

Figure 6.30: Harmonic Spectra of the Phase Voltage at the LFAC Side

As mentioned in Chapter 5, the circulating-current circuits are introduced to reduce abnormal distortions on wave forms and it is well known that the partial- and full-circulating-current modes could reduce the harmonics compared to the circulating-current free mode [28]. However, the quantitative comparison of harmonics between the full- and the partial circulating-current mode has been barely performed. Here, a simple comparison between both methods is performed. For this purpose, the same modulation index of 0.38 is used for both cases and the magnitude of the threshold current ((I_T)) for the partial circulating-current mode is half of the operating current at the LFAC-transmission system. Table 6.7 presents the numerical values of the harmonics contents, while Figure 6.31 graphically represents the harmonic spectra for both modes. As shown in Table 6.7 and Figure 6.31, the full circulating-current mode allows better performance in a quantitative analysis of harmonics than that from the partial-circulating current mode.

Table 6.7: Numerical Values of Harmonic Contents of the Phase Voltage at LFAC Side in Both Full- and Fifty Percent-Circulating Current Modes.

Circulating Mode	Harmonic Order										
	3	5	7	9	11	13	15	17	19	21	THDs
Full	17	4.8	3.7	1.4	1.2	0.4	0.04	39	37	2.4	48.87
50%	39	17	12	11	4.1	7.9	28	39	29	19	59.67

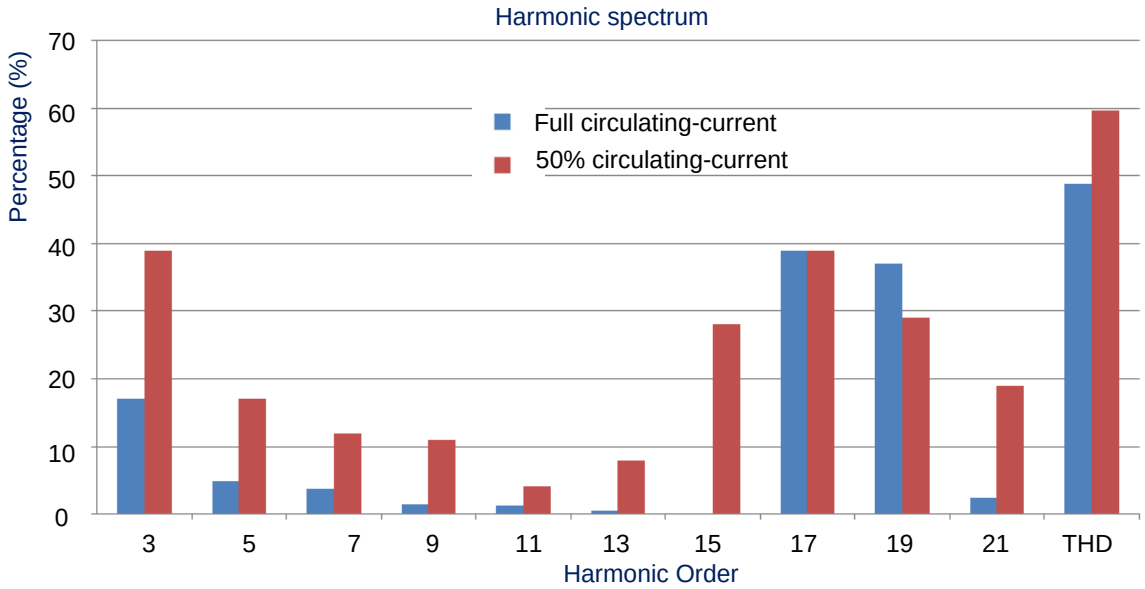

Figure 6.31: Harmonic Spectra of the Phase Voltage at the LFAC Side: (Blue) Full Circulating-Current Mode and (Red) 50% Circulating-Current Mode.

CHAPTER 7

CONCLUSION

7.1 Conclusions

The increased pressure from environmental restrictions and the economical crisis from increased prices of non-renewable natural resources [35] make renewables gradually become economical energy sources. The European Union has forecasted that renewable energies will reach 20 percent of the total energy capacity in 2020. North America has adopted a similar plan for 25 percent of the total energy capacity by 2025[13], [51]. In these cases, renewable energy sources, such as wind, solar, hydro energy, are experiencing dramatic innovations and improvements in terms of both quality and quantity.

Specifically, the rapid increase of wind generation in remote and offshore locations has accelerated the necessity of more reliable and cost-effective applications of alternative transmission systems, such as HVDC transmission and LFAC transmission. In these cases, switching systems are highly involved for the transmission and interconnection of renewable energy, since switching systems can easily permit the excellent controllability of electrical signals: changing voltage and frequency levels, power factor, etc. Converter systems recently seem to be key factors in the integration and the transmission of renewable resources.

With large percent penetration of weak-synchronous renewables and switching systems, traditional power systems might experience a dramatic upheaval on paradigms in which traditional power systems have been designed and operated. For example, traditional control algorithms for either protection devices or converters may not play their role with the traditional paradigms. New paradigms and technologies should be essential for flexible and reliable operation of future power systems, highly involving converters and nonlinearities. In this case, an advanced simulation tool, such as the QMQI method, can be the first step to study and analyze the new paradigms and the optimal design of new technologies.

The work, performed in this research, focused on alternative transmission systems interfacing wind farm systems and synchronous grid systems, as well as reliable and robust models of converters that were used for alterative transmission systems. For this purpose, the QMQI method is introduced for converter models in steady-state, quasi steady-state, and full time-domain. Consequently, these converters are used for the analyses and studies of new-type configurations of LFAC-transmission systems using the converter models.

In Chapter 3, a new modeling methodology was introduced for modeling and analyzing mixed power systems with nonlinearities and switching subsystems. The modeling method is based on the combination of model quadratization (quadratized models) and quadratic integration (QMQI). The quadratic-integration method was compared to trapezoidal integration and cubic integration to prove the superiorities in modeling power systems with nonlinearities and switching systems. In this comparative analysis, the quadratic-integration method was determined to be the best method among

the three collocation methods to model power systems with nonlinearities and switching systems. The quadratic integration method is an absolutely stable, quite accurate method to model them; moreover, the method is totally free of numerical oscillations. Also, the model quadratization can permit nonlinearities to be solved in nonlinear concept without simplification or approximation, leading to realistic models of nonlinearities described by nonlinear equations. Therefore, the QMQI method is suitable for power systems of switching subsystems with highly nonlinear components, such as saturable-core reactors and transformers [36].

In terms of converter models, converters such as a three-phase, six-pulse converter, a three-phase, six-pulse cycloconverter, and a three-phase, PWM converter were modeled in (quasi) steady-state and time-domain. Also, a push-pull resonant converter was modeled to explain how to model converters using the QMQI method. These converter models, derived by the QMQI method, were used for analysis and studies of the alternative transmission systems integrating wind-farm systems.

In Chapter 4, an averaging modeling concept was introduced for quantitative analyses of power systems with converters. The averaging method was based on the equivalent relationship between input and output (a two-port network analysis) in (quasi-) steady-state. In this averaging concept, the voltage and current ripples were averaged and the harmonics at both the AC side and the DC side of the converters were ignored. The dynamic behaviors, such as switching operation and transient phenomena, were not taken into consideration for the averaging converter models. However, this method has distinct advantages for quantitative analysis, such as power transfer capability, total operational losses, and optimal kV-level studies of networks. On the other hand, the averaging

models in a quasi steady-state used for simple dynamic analyses of power systems, since the models were developed with the assumptions: the electrical waves are operating in a sinusoidal, steady-state condition and the dynamics of the mechanical systems are explicitly models.

In chapter 5, full-time domain converters were modeled. For this purpose, physical components in converters were modeled in a realistic manner and merged using Kirchhoff's current law. Also, specific controllers were used for each converter. For the control algorithm, a DSP (digital signal processor) was used for sensing real-time values of currents and voltages from converters and for extracting proper references according to converters' own purposes. Using estimated references from the DSP, the switching sequence was computed and switching pulses were generated for each converter. The three-phase, six-pulse converter used an equidistant control algorithm and the three-phase, six-pulse cycloconverter used a cosine wave-crossing method. Note that the equidistant control and the cosine wave-crossing algorithms have the characteristic to minimize the total harmonic distortion at input and output for phase-controlled converters. For the three-phase PWM converter, DPC-SVM (direct-power control with space vector modulation) was used, since the control algorithm has demonstrated some outstanding characteristics including: a simple algorithm, a superior dynamic response, and steady-state performance [41]. The time-domain models were utilized for a better understanding of the dynamic behavior of power systems, such as the operation of electrical switches, harmonics, and power transients.

The converters, developed in Chapter 4 and 5, were used to analyze and study LFAC-transmission systems integrating wind-farm systems, as shown in Chapter 6. The

averaging converter models in steady-state were used for operational studies of an LFAC-transmission system using a three-phase, six-pulse cycloconverter and a three-phase PWM inverter, while the averaging models in quasi steady-state were used for voltage-stability studies over the example systems of LFAC transmission systems. Also, the time-domain models were used for power transient studies and harmonics studies.

In operational studies, the maximum power transfer capability (MPTC) of LFAC-transmission systems was compared to that of nominal frequency (60-Hz) transmission systems. For this purpose, the ability of electrical power systems to transfer electrical power from one place to another was analyzed within operational constraints of physical and electrical limitations. For the power transfer capability studies of LFAC-transmission systems, several constraints, which are assure the robust and secure operation of the power systems, were considered, such as the operational margins of converters (a cycloconverter and a PWM converter) and voltage-drop margins on AC-transmission lines. The results from these studies indicated that the LFAC transmissions have economic and performance advantages over conventional AC transmission, when the transmission distance is more than 50-miles. Note that the LFAC-transmission system greatly increased the MPTC and decreased the electrical loss, compared to conventional AC transmission. Also, it was detected that the power transfer capability of 20-Hz transmission is approximately two times of 60-Hz transmission.

Also, voltage stability studies were performed over several example configurations of LFAC-transmission systems by using the voltage right-though (VRT) capability requirement described by NERC standards. These voltage stability studies have been recognized to be of paramount importance for secure system operation of

LFAC transmission systems. Slow voltage recovery after a disturbance can cause significant damage: a voltage collapse and blackout can be caused by power system instability in the LFAC transmission systems integrating wind-farm systems [47]. These voltage stability studies increased the knowledge and understanding about the impact of contingencies on LFAC transmission systems; also, the knowledge from these stability studies helped maintain the secure operation of LFAC transmission systems. In these studies, we demonstrated that the LFAC-transmission systems can be continuously sustained after contingencies such as a three-phase fault and the dramatic change of wind farm systems, assuming that the contingencies are cleared within proper time (critical clearing time). However, the critical clearing time and the behavior of the analyzed systems much depend on the system configuration and the location of contingencies.

In time-domain studies, power-transient studies and harmonic studies were performed on LFAC-transmission systems. The LFAC-transmission systems should support the continuing power transmission, while either electrical loads or variable wind-sources vary in real-time. The flexible control of LFAC-transmission systems was required for the reliable and robust operation of power systems. The converters in LFAC-transmission systems supported flexible controllability for continuing operation: The three-phase PWM converters offered controllability of real- and reactive-power and voltage, while the three-phase, six-pulse converter permitted frequency and voltage level control on the low-frequency side. These power transient studies demonstrated that while the control algorithms of converters were properly modeled, the demonstrative examples could support continuing operation during the large or small variation of electrical loads and wind sources. Also, harmonic studies are of important, since harmonic pollution in

power systems can cause several problems: overheating problems in transformers and electrical machines, aging problems of isolation in power-system devices, malfunction of dynamic-control systems, and inductive interference over communication networks [14], [50]. Harmonics should be eliminated from voltages and currents and these wave forms are nearly pure sinusoidal signals with accurate harmonic analyses. In these harmonic studies, LFAC-transmission systems were analyzed over harmonics, according to the modulation indices of the cycloconverter. The modulation index was indicated as an important parameter. While the modulation index was decreased, the THD was substantially increased. These harmonic studies over LFAC-transmission systems gave the reference to optimally design harmonic filters, leading to the high quality operation of the LFAC-transmission systems.

7.2 Future Work

The present research is dedicated to introducing a new modeling methodology for power systems with nonlinearities and switching subsystems, to model converter systems using advanced modeling-methodology, and to analyze new-type alternative configurations of LFAC-transmission systems. These LFAC-transmission systems are designed for the interconnection of remote wind farm systems and main grid systems in terms of economics and technical benefits. Future work may be extended in consideration of the economic and technical integration and transmission using alternative transmission systems.

Alternative transmission systems are of paramount importance to the transmission and integration of renewable resources, since renewable energy is rapidly developing to

substitute for non-renewable energy. However, the economics and technical challenges of alternative transmission systems are challenging: they depend on many factors: distance between energy sources and load centers, topographic characteristics such as offshore and onshore, system configurations to be connected, etc. Thus, the configuration of alternative transmission systems should be carefully selected and intensively analyzed in technical and economic aspects. The converter models developed can be utilized to study other configurations of alternative transmission systems, leading to least cost integration of renewable resources.

Another main concern in the integration and transmission of renewable resources is whether the paradigms used for traditional grid systems can also perform their role in the new topology connecting a large percentage of renewable generating systems. It is worth considering the characteristics of synchronous systems and synchronization procedures and comparing them to weak systems with high penetration of renewable resources. For example, traditional control algorithms, and protection devices must sense and estimate voltages and currents in real-time, and then they should perform their roles in fraction of a second. However, traditional devices may not work well in weak systems, since the operating frequency in these systems may require different data processing algorithms and different protection logic as compared to traditional power-systems. Therefore, new paradigms for weak synchronous power systems are required for reliable and robust operation. Specifically, new protection paradigms and algorithms must be developed for these systems [14]. The modeling and simulation methods developed in this Thesis can be utilized for the investigation of the mentioned challenges.

REFERENCES

[1] A. Meliopoulos, G. Cokkinides, and G. Stefopoulos, "Quadratic integration method," in *Proceedings of the 2005 International Power System Transients Conference*, Citeseer, 2005, pp. 19–23.

[2] M. Roitman and P. Diniz, "Simulation of Nonlinear and Switching Elements for Transient Analysis Based on Wave Digital Filters," *IEEE transactions on Power Delivery*, vol. 11, no. 4 pp. 2042-2048, Oct. 1996.

[3] W. Gao, E. Solodovnik, R. Dougal, G. Cokkinides, and A. Meliopoulos, "Elimination of numerical oscillations in power system dynamic simulation," in *Proceedings Power Electronics Conference and Exposition, 2003 APEC'03. Eighteenth Annual IEEE*, vol. 2, Feb. 2003.

[4] J. Lin, J. R. Marti, "Implementation of the CDA procedure in the EMTP," *IEEE Transactions on Power Systems*, vol. 5, no. 2, pp. 394-402, May 1990.

[5] S. N. Hong, C. R. Liu, Z. Q. Bo, and A Klimek, "Elimination of numerical oscillation of dynamic phasor in HVDC system simulation," in *proceedings of Power and Energy Society General meeting*, Jul. 2009, pp. 19–23.

[6] M. Roitman, and P. S. R. Diniz, "Power systems simulation based on Wave Digital filters," *IEEE Transactions on Power Delivery*, vol. 12, pp. 1098-1104, Apr. 1966.

[7] R. Rudervall, J. P. Charpetier , and R. Sharma, "High voltage direct current (HVDC) transmission systems technology review paper," in *Energy Week*, Washington, D. C, USA, Mar. 2000.

[8] D. Woodford, "HVDC Transmission," Manitoba HVDC Research Centre Inc. Manitoba, Canada, 1998.

[9] M. P. Bahrman, "Overview of HVDC transmission," in *proceedings of Power Systems Conference and Exposition, 2006. PSCE '06. 2006 IEEE PES*, Oct. 2006, pp. 18-23.

[10] J. Setreus, and L. Bertling, "Introduction to HVDC technology for reliable electrical power systems," in *Proceedings of the 10th International Conference on Probabilistic Methods Applied to Power Systems*, May 2008, pp. 1-8.

[11] P. Pourbeik, M. Bahrman, and E. John, W. Wong, "Modern countermeasures to blackouts," *Power and Energy Magazine, IEEE*, vol. 4, no. 5, Sep. 2006.

[12] H M. P. Bahrman, "HVDC transmission overview," in *Proceedings Transmission and Distribution Conference and Exposition, 2008. T&D. IEEE/PES*, Chicago, IL, Apr.21–24, pp. 1–7.

[13] Nan Qin, Shi You, Zhao Xu, and V. Akhmatov, "Offshore wind farm connection with low frequency AC transmission technology" in *proceedings of Power & Energy Society General Meeting, 2009. PES '09. IEEE*, July 2009, pp. 1 – 8.

[14] A. P. Meliopoulos, Dionysios Aliprantis, Yongnam Cho, Dongbo Zhao, Anupama Keeli, and Hao Chen," Low frequency transmission" *Power Systems Engineering Research Center, Tech. Rep. S-42*, Oct. 2012.

[15] P. Bresesti, W.L. Kling, and R. Vailati, "Transmission expansion issues for offshore wind farms integration in Europe," in *proceedings of IEEE PES Transmission and Distribution Conference and Exhibition*, Chicago, Apr. 2008, pp. 1-7.

[16] K.E. Atkinson, *An introduction to numerical analysis*, 1989; John Wiley & Sons.

[17] Yongnam Cho, G.J. Cokkinides, and A.P. Meliopoulos, "Transient simulation technique for HVDC systems," *in proceeding of the International conference on Power Systems Transients*, Delft, the Netherlands, Jun. 2011.

[18] Eugene V. Solodovnik, George J. Cokkinides and A. P. Sakis Meliopoulos, "On stability of implicit numerical methods in nonlinear dynamical systems simulation," in *Proceedings of the Thirtieth Southeastern Symposium on System Theory*, Mar. 1998, pp. 27-31.

[19] Guang-Da Hu, Guang-Di Hu, and S. Meguid, "Stability of Runge–Kutta methods for delay differential systems with multiple delays," *IMA J. Numer. Anal.*, 19 (1999), pp. 349–356

[20] J. R. Marti and J. Lin, "Suppression of numerical oscillations in the EMTP," *IEEE Transactions on Power Systems*, vol. 4, no. 2, pp. 739-747, May 1989.

[21] V. Rraridwajn, "Damping of numerical noise in the EMTP solution," EKrP Newsletter, Vol. 2. No. 3, pp. 10-19, Feb. 1982.

[22] F. 1. Alvarado, H. H. Lasseter, and J. J. Sanchez, "Testing of trapezoidal integration with damping for the solution of power transient problems," *IEEE Transaction on Power Apparatus and Systems*, Vol. PAS--102, No. 12, pp. 3783.3790. Dec. 1983.

[23] E. Hairer and G. Wanner, *Solving ordinary differential equation II: Stiff and differential-algebraic problems*. Springer Series in Computational Mathematics 14. Springer-Verlag, Berlin, Heidelberg, 1991.

[24] Guang-Da Hu, Guang-Di Hu, and S. Meguid, "Stability of Runge–Kutta methods for delay differential systems with multiple delays" *IMA J. Numer. Anal.*, 19 (1999), pp. 349–356

[25] Joseph E. Flaherty. Ordinary differential equations. [On-line]. Available: http://www.cs.rpi.edu//~flaherje/pdf/ode3.pdf [Jan. 24, 2013].

[26] C.-L. Chu and C.-H. Li. "Analysis and design of a current-fed zero-voltage-switching and zero-current-switching CL_resonant push-pull dc-dc converter," Power Electronics, IET, vol. 2, pp. 456-465, Jul. 2009.

[27] A. Meliopoulos, S. Kang, G. Cokkinides, and R. Dougal, "Animation and visualization of spot prices via quadratized power flow analysis", in *Proceedings of the 36th Hawaii International Conference on System Sciences*, Jan. 2003.

[28] R. Pelly, "Cycloconverter circuits," in *Thyristor Phase-Controlled Converters and Cycloconverters*, New York: Wiley, 1971.

[29] G. Stefopoulos, "Quadratic power system modeling and simulation with application to voltage recovery and optimal allocation of var support," Ph.D dissertation, ECE, Georgia Institute of Technology, GA, Aug 2009.

[30] R. Simard and V. Rajagopalan, "Economical equidistant pulse firing scheme for thyristorized DC drives," *IEEE Transactions on Industrial Electronics and Control Instrumentation*, pp. 425–429, no. 3, Aug. 1975.

[31] S. Bhat, "Novel equidistant digital pulse firing schemes for three-phase thyristor converters*," International Journal of Electronics*, vol. 50, no. 3, pp. 175–182, 1981

[32] J. Ainsworth, "The phase-locked oscillator - A New Control System for Controlled Static Convertors," *IEEE Transactions on Power Apparatus and Systems*, vol. PAS-87, no. 3, pp. 859–865, Mar. 1968.

[33] J. Pontt, J. Rodriguez, E.Caceres, E. Illanes, and C. Silva, "Cycloconverter drive system for fault diagnosis study: real time model, simulation and construction," *in Proceedings of Power Electronics Specialists Conference*, 2006. PESC '06. 37th IEEE, Jun. 2006, pp. 1-6.

[34] W. A. Hill, E. Y. Y. Ho, and I. J. Nuezil, "Dynamic behavior of cycloconverter system," *IEEE Transactions on Industry Applications*, vol. 27, no. 4, pp.750-755, Aug. 2002.

[35] Yongnam Cho, G.J. Cokkinides, and A.P. Meliopoulos, "Time domain simulation of a three-phase cycloconverter for LFAC transmission systems," *in proceeding of Transmission and Distribution Conference and Exposition (T&D), 2012 IEEE PES,* West Virginia, Florida, USA, 2012.

[36] Yongnam Cho, G.J. Cokkinides, and A.P. Meliopoulos, "Advanced time domain method for remote wind farms with LFAC transmission systems: Power transfer and harmonics," *in proceeding of North American Power Symposium (NAPS), Illinois, 2012*.

[37] Yongnam Cho, G.J. Cokkinides, and A.P. Meliopoulos, " LFAC-transmission systems for remote wind farms using a three-phase, six-pulse cycloconverter ," *in proceeding of Power Electronics and Machines in Wind Applications (PEMWA)*, CO, July 2012

[38] M. Malinowski and M. P. Kazmierkowski, "Direct power control of three-phase PWM rectifier using space vector modulation—Simulation study," in *Proceedings of the 2002 IEEE International Symposium on industrial Electronics*, vol. 4, 2002, pp. 1114–1118.

[39] Y. Tang and L. Xu, "A flexible active and reactive power control strategy for a variable speed constant frequency generating system," in *proceedings of Power Electronics Specialists Conference, 1993. PESC '93 Record., 24th Annual IEEE*, Jun. 1993, pp. 568–573.

[40] L. Xiao, S. Huang, T. Liu, Q. Xu, and K. Huang, "A novel SVM-DPC control method for gird connected AC-DC converters under asymmetrical fault," in *proceedings of 2011 International Conference on Power Engineering, Energy and Electrical Drives (POWERENG)*, May 2011, pp.1 – 6.

[41] L. Xu and P. Cartwright, "Direct active and reactive power control of DFIG for wind energy generation," *IEEE Transactions on Energy Conversion.*, vol. 21, no. 3, pp. 750–758, Sep. 2006.

[42] S. Bozhko, R. V. Blasco-Gimenez, R. Li, J. Clare, and G. Asher, "Control of offshore DFIG-based wind farm grid with line-commutated HVDC connection," *IEEE Transactions on Energy Conversion*, vol. 22, no. 1, pp. 71–78, Mar. 2007.

[43] D. Xiang, L. Ran, J. R. Bumby, P. J. Tavner, and S. Yang, "Coordinated control of an HVDC link and doubly fed induction generators in a large offshore wind farm," *IEEE Transactions on Power Delivery*, vol. 21, no. 1, pp. 463–471, Jan. 2006.

[44] Wu, Bin, *High-Power converters and AC drives*, IEEE Press, USA, 2006

[45] __"Available transfer capability definitions and determination," North Amer. Elect. Rel. Council, Princeton, NJ, June 1996

[46] P. Kundur, J. Paserba, V. Ajjarapu, G. Andersson, etc., "Definition and classification of power system stability" *IEEE Transactions on Power Systems*, Vol. 19, no. 2, pp 1387 – 1401, May, 2004.

[47] A. P. Meliopoulos, G. J. Cokkinides, and G. K. Stefopoulos, "Voltage stability and voltage recovery: Effects of electric load dynamics," in *proceedings of IEEE International Symposium on Circuits and Systems*, May. 2006, pp. 5-734.

[48] P. Kundur, J. Paserba, V. Ajjarap, *et al.*, "Definition and classification of power system stability," *IEEE Transactions on Power Systems*, vol. 19, no.3, pp. 1387-1401, Aug. 2004.

[49] S. M. Muyeen, R. Takahashi, T. Murata, *et al.*, "Low voltage ride-through capability enhancement of wind turbine generator system during network disturbance," *IET transaction on Renewable Power Generation*, Vol. 3, No. 1, pp. 65-74, Mar. 2009.

[50] Asaad A. Elmoudi, "Evaluation of power system harmonic effects on transformers," Ph.D dissertation, ECE, Helsinki University of Technology, FINLAND, 2006.

[51] Teodorescu, Remus, Marco Liserre, and Pedro Rodriguez, Introduction in *grid converters for photovoltaic and wind power systems*, Chichester, West Sussex: Wiley, 2011.

VITA

YONGNAM CHO

YONGNAM CHO was born in Janghang, Korea in 1978. He attended public schools in Kunsan, Korea and received his high school diploma in February 1997. After graduation, he joined the school of Electrical Engineering at Myongji University in Korea. In the middle of his university period, he performed military duties for two years, from 1999 to 2001. Eventually, he finished his Bachelor's degree in 2005. In August 2006, he joined the school of Electrical and Computer Engineering at Georgia Institute of Technology, in Atlanta, Georgia, where obtained Master's degree in 2010.

Since the beginning of his studies at Georgia Tech, Mr. Yongnam Cho has been a graduate research assistant under the supervision of Professor A. P. Sakis Meliopoulos who has made significant contributions to power system grounding, harmonics, and the reliability assessment of power systems. Mr. Yongnam Cho has been working on topics in computer modeling and analysis of power systems. In particular, his specialization is in converter systems that are used for the integration and transmission of renewable resources.